GNSS-Based Relative Navigation for LEO Nanosatellite Laser Communications

by

Peter W. Grenfell

B.S., University of California Berkeley (2017)

Submitted to the Department of Aeronautics and Astronautics
in partial fulfillment of the requirements for the degree of

Master of Science in Aeronautics and Astronautics

at the

MASSACHUSETTS INSTITUTE OF TECHNOLOGY

February 2020

Signature redacted

Author .....
Department of Aeronautics and Astronautics
January 30, 2020

Signature redacted

Certified by .....
Kerri Cahoy
Associate Professor of Aeronautics and Astronautics
Thesis Supervisor

Signature redacted

Accepted by .....
Sertac Karaman
Associate Professor, Aeronautics and Astronautics
Chair, Graduate Program Committee

GNSS-Based Relative Navigation for LEO Nanosatellite Laser Communications

by

Peter W. Grenfell

Submitted to the Department of Aeronautics and Astronautics
on January 30, 2020, in partial fulfillment of the
requirements for the degree of
Master of Science in Aeronautics and Astronautics

Abstract

The Size, Weight, and Power (SWaP) efficiency of laser communications make it a good fit for development in concert with rising interest in small satellite mission concepts. The CubeSat Laser Infrared CrossinK (CLICK) mission has the objective of demonstrating the first Low-Earth orbit (LEO) nanosatellite crosslink. The need for precise and accurate pointing with laser instruments motivates a formalized, systematic approach to fulfilling this need called Pointing, Acquisition, and Tracking (PAT). The focus of this work is the initial Global Navigation Satellite System (GNSS) based relative navigation pointing process for LEO crosslinks and downlinks.

In Chapter 2, the baseline CLICK pointing budgets are given for crosslink and downlink relative navigation based body pointing. For crosslink, the 99^{th} percentile angular relative navigation errors are 1367 μrad & 76.58 μrad for the minimum 25 km range and maximum 580 km range cases, respectively. The corresponding 99.7% pointing losses are -0.278 dB & -0.182 dB, with margins of 1.222 dB & 1.318 dB relative to the -1.5 dB requirement. For downlink, the 99^{th} percentile angular relative navigation error is 17.29 μrad, with a corresponding 99.7% pointing loss of -0.189 dB and margin of 1.311 dB. The crosslink and downlink access durations are also determined by simulation.

In Chapter 3, using Cowell's method with only an appropriate central body gravity model, model-induced propagation error is maintained to less than 50 m for intervals up to 90 minutes and less than 25 m for intervals up to 30 minutes. This corresponds to crosslink 99^{th} percentile angular errors of less than 600 μrad at 25 km and less then 40 μrad at 580 km. Earth-Centered-Inertial (ECI) to Earth-Centered-Earth-Fixed (ECEF) transformations are discussed for ground station position prediction, and even with the simplest transformation formulation, position error remained less than 16 m. Model-induced error for all downlink cases had a 99^{th} percentile error of less than 32 μrad. The relative navigation error for crosslinks is analyzed for the baseline CLICK configuration of directly propagating GPS fixes. For crosslinks across all configurations, the 99^{th} percentile angular errors are less than $\sim$2000 μrad at 25 km and less then $\sim$200 μrad at 580 km, corresponding to 99.7% pointing losses less than

-1.235 dB at 25 km and -0.427 dB at 580 km and corresponding margins greater than 0.265 dB and 1.073 dB, respectively. For downlinks, the 99^{th} percentile error across all cases is less than $\sim$45 μrad, which corresponds to 99.7% pointing losses of less than -0.434 dB with margins greater than 1.066 dB across all cases, including simplified Earth rotation models.

In Chapter 4, Kalman filtering algorithms are explored to improve GNSS-based orbit determination for relative navigation in LEO. Three different formulations of the Extended Kalman Filter (EKF) correction and prediction subroutines are explored in depth: 1) the Conventional EKF (CEKF); 2) the Joseph Sequential EKF (JSEKF); 3) the UD Sequential EKF (UDSEKF). Implementation and time complexity differences are discussed for Runge-Kutta methods used to solve state prediction problem and for matrix exponential methods used to approximate continuous-time covariance prediction. The EKF for orbit determination using GNSS measurements is formulated using the ECI position and velocity, a central body gravity model, and nondimensionalization. The CEKF, JSEKF, and UDSEKF filter formulations are evaluated on three metrics: efficiency as per analytical time complexity results, consistency, and orbit determination accuracy. The overall ranking is 1) UDSEKF, 2) CEKF, 3) JSEKF. With the addition of Kalman filtering, across all crosslink configurations, the 99^{th} percentile angular errors are less than $\sim$1000 μrad at 25 km and less then $\sim$100 μrad at 580 km, and the 99.7% pointing losses are less than -0.623 dB at 25 km and -0.421 dB at 580 km with corresponding margins greater than 0.877 dB and 1.079 dB, respectively. This corresponds to improvements of at least 50% for the angular error across all cases. For the CLICK hardware configuration, filtering has a significantly greater effect on pointing loss at shorter ranges. Applying filtering for downlinks yields an improvement in the overall 99^{th} percentile error across all cases by at least 22.2% to less than $\sim$35 μrad. As anticipated from previous analysis, filtering has a negligible impact on pointing loss for downlink due to the dominance of mechanical and spacecraft errors in the CLICK downlink pointing budget. Filtering had the greatest impact for short range crosslinks. Nevertheless, for future missions with more stringent requirements, narrower beams, improved mechanical errors, and/or significantly worse GPS measurement errors, filtering may also have significant benefit for long range crosslinks and for downlinks.

Thesis Supervisor: Kerri Cahoy
Title: Associate Professor of Aeronautics and Astronautics

Acknowledgments

This work was partially funded by the CLICK (CubeSat Laser Infrared CrosslinK) Technology Demonstration Mission, Grant Number 80NSSC18K1579. The views, opinions, and/or findings contained in this work are those of the author and should not be interpreted as representing the official views or policies, either expressed or implied, of the National Aeronautics and Space Administration.

I would like to thank my advisor Kerri Cahoy for her continuous support of my research and work with her group in the Space, Telecommunications, Astronomy, and Radiation (STAR) Laboratory. I would like to thank all of my colleagues on the CLICK mission including my teammates at MIT, the University of Florida's PSSL, and NASA Ames Research Center. I would also like to thank my peers in MIT AeroAstro who I've worked with in numerous courses and have had the good fortune to call friends. Finally, I would like to thank my family and friends without whom I wouldn't be where I am today.

Contents

List of Figures

List of Tables

Chapter 1

Introduction

A laser communications system operating in the visible or infrared spectrum (~533 nm, 780-980 nm, 1064 nm, 1550 nm) has several advantages that distinguishes it from conventional radio frequency communications, which operate in the spectrum between the Ultra-High Frequency (UHF) band (300 - 1000 MHz [1]) up to the W Band (75 - 100 GHz [1]). These features include: 1) increased Size, Weight, and Power (SWaP) efficiency; 2) improved data rate scalability due to a combination of SWaP efficiency, increased bandwidth, and high carrier frequency; 3) less crowded frequency bands with reduced regulatory burden from licensing; 4) improved link security; 5) reduced risk of mutual interference (self-jamming) and jamming more generally; and 6) hybrid instrument capabilities combining communications with capabilities such as ranging, spectrometry, and laser remote sensing [2, 3, 4]. Laser communications is currently being pursued across the aerospace community for telecommunications and earth observing satellites, both for commercial and defense applications as well as for next generation data relays in space science and exploration applications.

This work focuses on laser communications (lasercom) for nanosatellites (~ 10 kg). The nanosatellite class includes a popular modular design framework developed by California Polytechnic Institute known as CubeSats [5]. These are characterized as being made up of volume units (Us), where 1U is 10 cm x 10 cm x 10 cm. Common nanosatellite form factors include 1U, 3U, and 6U.

1.1 Review of Satellite Laser Communications Missions

A collection of specific uses of laser communications in satellite missions is given in Table 1.1. Beginning in the 1980s with the Semiconductor laser Intersatellite Link Experiment (SILEX) mission, there has been significant progress in recent decades in developing laser communications for large satellites ($\sim$ 1000 kg class), with a series of successful technology demonstrations in the 2010s by the European Space Agency (ESA), National Aeronautics and Space Administration (NASA), and Japanese Aerospace Exploration Agency (JAXA) as well as technology commercialization. The SILEX, Optical Inter-orbit Communications Engineering Test Satellite (OICETS), European Data Relay System (EDRS), and Laser Communications Relay Demonstration (LCRD) missions have been focused on lasercom relays to Geostationary Earth Orbit (GEO), wherein a LEO satellite such as the International Space Station (ISS) or an earth-observing satellite is able to uplink to a GEO satellite, which then rapidly downlinks to the ground. Additional technology demonstrations with large spacecraft have included a LEO-LEO intersatellite link (ISL) demonstrated by the German Aerospace Center (DLR) Laser Communication Terminal (LCT) and a downlink from NASA's Lunar Atmosphere Environment Explorer (LADEE) lunar orbiting spacecraft to the ground. With the maturation of laser communications for large satellites has come the subsequent development of the technology for microsatellites ($\sim$ 100 kg class) like 2014's Bispectral Infrared Optical System (BiROS) and Space Optical Communications Research Advanced Technology Satellite (SOCRATES). Both of these missions demonstrated direct downlinks from LEO satellites to the ground. The SWaP efficiency and hybrid instrument capabilities of lasercom terminals have motivated the extension of this technology to the nanosatellites ($\sim$ 10 kg class), which feature reduced costs compared to larger satellites [5].

Reduced costs make nanosatellites and microsatellites ideally suited for advanced mission designs requiring a multitude of satellites, including large constellations covering the Earth, as well as clusters or swarms of satellites flying in formation to achieve

an objective that would not be possible with a single large satellite, such as distributed aperture sensing or increased resilience via spacecraft fractionation. Therefore, there is significant motivation to improve the capabilities of small satellites, and the key features of laser communications make it an ideal technology to significantly improve the capabilities of this class of satellites, benefiting many applications both in the democratization of space as well as advanced mission concepts. The first nanosatellite lasercom technology demonstration was NASA's Optical Communications and Sensor Demonstration (OCSD), which completed downlinks from LEO to the ground. To date, no nanosatellite lasercom ISLs have been demonstrated. However, one development in ISLs for nanosatellites came when one of the OCSD satellites signalled to a camera aboard another satellite using its wide angle laser [6]. The CubeSat Laser Infrared CrosslinK (CLICK) nanosatellite mission will demonstrate a full-duplex intersatellite crosslink in LEO in addition to downlinks [7].

In summary, the SWaP efficiency of laser communications make it a good fit for development in concert with rising interest in small satellite mission concepts. Nanosatellite LEO to ground downlinks have been demonstrated and improved performance is expected with future downlink demonstrations. The CLICK B/C mission has the objective of demonstrating the first nanosatellite crosslink. This mission was the catalyst for this thesis research and will be referenced throughout as a motivating example and case study in nanosatellite laser communications. The next section will give an overview of the CLICK B/C mission.

Table 1.1: Selection of Satellite Laser Communications Missions

Year	Mission: Satellite(s)	Host-Partner Orbits	P_{Tx} (mW)	Data Rate (Mbps)	θ_{FWHM} (μrad)	Ref.
1985-2001	SILEX: SPOT-4	LEO-GEO	70	50	4	[8]
1985-2001	SILEX: ARTEMIS	GEO-LEO	35	2	7	[9, 10]
1993-2005	OICETS: OICETS	LEO-GEO	100	50	7	[9, 10]
2002-2007	DLR-LCT: TerraSAR-X, NFIRE	LEO-LEO	1000	5625	9	[10, 11]
2012	EDRS: Sentinel 1A, Alphasat	LEO-GEO	5000	2800	8	[10]
2013	LLCD: LADEE	Lunar-Ground	500	622	15	[12]
2014	SOTA: SOCRATES	LEO-Ground	22	10	223	[13]
2014	OSIRIS: BiROS	LEO-Ground	1000	1000	200	[8]
2015	OCSD: Aerocube A,B,C	LEO-Ground	6000, 2000, 2000	5, 200, 200	6109, 2618, 873	[6]
2019	VSOTA: RISESAT	LEO-Ground	80	0.1	1300	[14]
2019	LCRD: STPSat-6	GEO-LEO	N/A	311-1244	15	[15, 16]
2023	LCRD ILLUMA-T: ISS	LEO-GEO	3000	1200	16	[17]
2020s	TBIRD	LEO-Ground	1000	200000	130	[18, 19]
2020s	CLICK: A	LEO-Ground	200	10	1300	[7, 20]
2020s	CLICK: B/C	LEO-LEO	200	20	70	[7, 20]

1.2 CLICK B/C Mission Overview

The motivation for this thesis research comes from the CubeSat Laser Infrared CrossLinK (CLICK) nanosatellite laser communications demonstration mission. This mission is composed of two phases. In the first phase, the CLICK A spacecraft will demonstrate a low-Earth orbit (LEO) space to ground downlink with a compact, mobile optical ground station called the Portable Telescope for Laser Communications (PorTeL). The CLICK A terminal is described in detail in Payne et al. [21]. The PorTeL terminal is described in detail in [22, 23]. In the second phase of the mission, the CLICK B

& C spacecraft will demonstrate the first LEO communications crosslink between two nanosatellites as well as downlinks to PorTeL [7]. The baseline crosslink ranges are 25 - 580 km, and the two spacecraft will be deployed in a co-orbital, string-of-pearls configuration. This constitutes a crosslink type that may be required by formation flying spacecraft and the planar building blocks of satellite constellations. Here we will present a brief overview of the terminal architecture and concept of operations.

The CLICK B/C terminal optical hardware is shown in Figure 1-1. Background

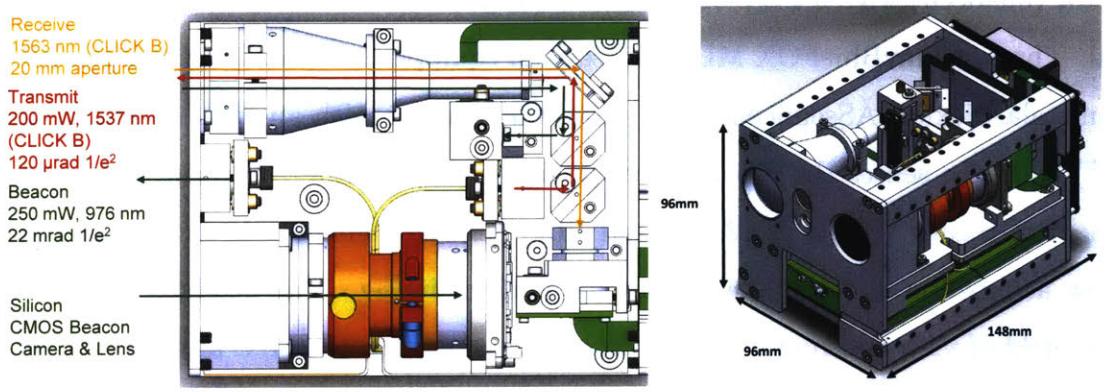

Figure 1-1: CLICK B/C Lasercomm Terminal

information on the hardware used in lasercom terminals can be found in Appendix A.1. The communications design enables a full-duplex laser communications crosslink and a simplex laser communications downlink. The communications laser is 200 mW and near the 1550 nm wavelength, with one terminal transmitting at 1537 nm and the other terminal transmitting at 1563 nm to enable spectral isolation of the transmit (Tx) and receive (Rx) paths in both terminals to avoid self-jamming. The isolation is accomplished via dichroic filter mounted at a 45 degree angle that acts as a fold mirror for the transmit path while passing the receive signal.

The Tx & Rx paths share the same telescope aperture, with a micro-electro-mechanical system (MEMS) fast steering mirror (FSM) placed at the output of the telescope to enable steering of the transmit (Tx) beam via optical feedback. The telescope itself is in a Keplerian beam expander configuration with a clear aperture of 20 mm and a lateral magnification factor of 10.53×. The Tx collimator output has a full-width half-maximum (FWHM) beam divergence of 750 μrad and uses a

single mode 1550 nm fiber. The telescope reduces this further to the final Tx FWHM beam divergence of 71.2 μrad (14.7 arcsec). There is a second optical source mounted next to the telescope aperture. This is a 976 nm beacon laser operating at 250 mW average power with a collimator output FWHM divergence of 13 mrad (0.75°). There are three sensors. One, an InGaAs avalanche photodiode detector (APD) communications detector with an field of view (FOV) of 2.84 mrad (585 arcsec) that detects the 1537 or 1563 nm signal. Two, a silicon quadrant p-intrinsic (PIN) photodiode detector (quadcell) with a FOV of 6.28 mrad (0.36°) that detects the 976 nm beacon signal. Three, an mvBlueFOX MLC-205 camera equipped with a silicon complementary metalâĂŞoxideâĂŞsemiconductor (CMOS) detector with an FOV of 182 mrad (10.4°) that also senses the 976 nm beacon signal. With the FSM throw, the quadcell field of regard (FOR) is 12.92 mrad (0.74°). The camera acts as a wide field of view acquisition and tracking sensor for body pointing. The quadcell acts as a narrow field of view tracking sensor for fine beam steering. The B/C mission concept

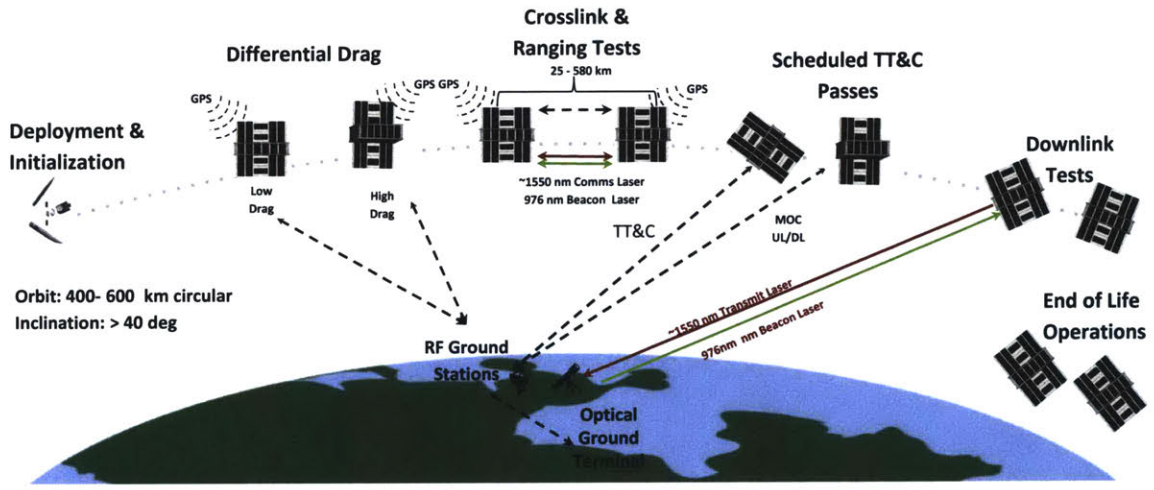

Figure 1-2: Concept of operation for the CLICK-B/C mission.

of operations sketched in Figure 1-2 begins with launch and deployment of the two spacecraft into a LEO orbit with an altitude between 400-600 km and inclination greater than 40 degrees. After commissioning, the establishment of the relative range for crosslink experiments begins. As the CLICK spacecraft are not equipped with

propulsion systems, they utilize differential drag to begin drifting apart, with the 25 km range established after approximately 1 week and the 580 km range established after an additional 2-3 weeks. The drag management is then used to reverse the drift repeatedly and traverse this operations range for mission operations lasting from 6 - 12 months. Optical downlinks will also be conducted using a PorTeL optical ground station located in the Boston, MA area. The two spacecraft are equipped with radios that can uplink/downlink telemetry as well as provide crosslink access to ephemeris data gathered by each spacecraft's Global Navigation Satellite System (GNSS) receiver, which use the U.S. Global Positioning Service (GPS). Both spacecraft body point the payload apertures and fixed beacon laser.

The need for precise and accurate pointing with laser instruments motivates a formalized, systematic approach to fulfilling this need called a Pointing, Acquisition, and Tracking (PAT). For crosslink, relative navigation information derived from the GPS measurements aboard both satellites provides the initial pointing information for beacon acquisition on the beacon camera. The beacon camera data is used for feedback to refine the body pointing. Upon secondary acquisition of the beacon on the quadcell, the closed-loop fine tracking process begins, followed by the communications process. The baseline communications link duration is 10 minutes, with an anticipated minimum data rate of 20 Mbps. Throughout communications, the coarse spacecraft tracking and fine steering mirror tracking processes continue to maintain the link.

The downlink process is somewhat different. The first stage involving navigation is similar, except instead of the target position being estimated via orbit propagation, it is estimated using an earth rotation model and ground station coordinates stored from periodic TT&C uplinks. Furthermore, the spacecraft body pointing does not employ feedback from the camera during downlink. Rather, the navigation solution is used throughout, and the ground station's beacon is used only for fine pointing feedback. While body pointing, the quadcell acquires the ground station's beacon signal, enabling fine pointing & communications.

The focus of this thesis is the initial pointing process for these LEO crosslinks and

downlinks using GPS-based relative navigation. Additional discussion of the CLICK B/C PAT sequence can be found in Appendix A.5, and additional details on the CLICK B/C terminal design and development can be found in [7, 24, 20].

1.3 Thesis Overview

Chapter 1 summarized the history of satellite laser communications missions and introduced the CLICK B/C nanosatellite lasercom mission, with a synopsis of its PAT processes for establishing crosslinks and downlinks. The focus of this thesis is the initial pointing process for these LEO crosslinks and downlinks using GPS-based relative navigation.

Chapter 2 will first give background on the concepts of laser beam geometry and the laser link range equation. Then derivations will be given for the Rice/Rician model of the total pointing error and the non-central chi-squared model of the pointing loss. These pointing models are then used in pointing budgets for the initial relative navigation stages of the CLICK PAT processes for crosslinks and downlinks to show that the pointing loss requirement of -1.5 dB or less is met. The crosslink access will be evaluated using sun keep out for the beacon camera, and downlink access will be evaluated using overpass durations and ranges.

Chapter 3 will discuss onboard GNSS-based relative navigation for establishing LEO crosslinks and downlinks. Both the Cowell method for spacecraft state propagation and the ECI-ECEF transformations used for ground station position prediction will be analyzed and simulated for errors incurred from incurred from simplifications. This will be followed by a derivation of how GPS position & velocity fixes are generated and their noise properties. Noise analysis and simulations will be conducted for GPS receivers in LEO and in the Continental U.S. (CONUS). Finally, the relative navigation error for crosslinks and downlinks will be simulated by combining orbit propagation with raw GPS fixes, which is the baseline configuration for CLICK. This baseline configuration will be confirmed to meet CLICK's pointing requirements.

In Chapter 4, the Extended Kalman Filter (EKF) will be presented to improve

GNSS-based orbit determination. Three different formulations of the correction and prediction subroutines will be explored in depth: 1) the Conventional EKF (CEKF); 2) the Joseph Sequential EKF (JSEKF); 3) the UD Sequential EKF (UDSEKF). Numerical integration methods for state prediction using fixed & variable step methods and for covariance prediction using the matrix exponential will be presented and compared. The three formulations will be compared on the basis of their overall time complexities, consistency, and orbit determination accuracy. Finally, results for improved relative navigation via propagation with Kalman filtered GNSS measurements for crosslinks and downlinks will be presented and discussed in the context of CLICK and potential future missions.

Chapter 2

Pointing Error Analysis

The starting point for any laser communications system are the link parameters, which are captured in a systems engineering tool called the link budget. For each laser link, including beacon links, a link budget is maintained for systems engineering purposes to predict the performance to be verified and validated by the overall communications system. A key element of this link analysis is the received power analysis, which contains statistical models of random elements: these generally include power loss at the receiver due to transmitter pointing error and, for uplinks & downlinks, losses due to atmospheric effects. In this chapter, we review the standard statistical model for pointing error and the associated systems engineering tool called the pointing budget, which is used to predict the total pointing loss.

2.1 The Gaussian Beam

In this section, the aspects of the theory of wave optics relevant to link analysis are reviewed. For in-depth background on scalar wave theory, reference Saleh & Teich [25]. For our present analysis, we are interested in the intensity, I, pattern of a laser beam. We assume that the transmitted beam is not truncated, nor is it obscured in any way by obstacles in the path of propagation. For a treatment of truncated, centrally obscured beam propagation, as would occur in a Schmidt-Cassegrain telescope transmitter configuration, refer to Degnan & Klein [26]. An

ideal laser beam is modeled as a Gaussian beam, which is in-between a plane wave which is infinite in extent and has no spread and a spherical wave which spreads over all of space. The $1/e^2$ beam width is defined by the bounding surface representing the

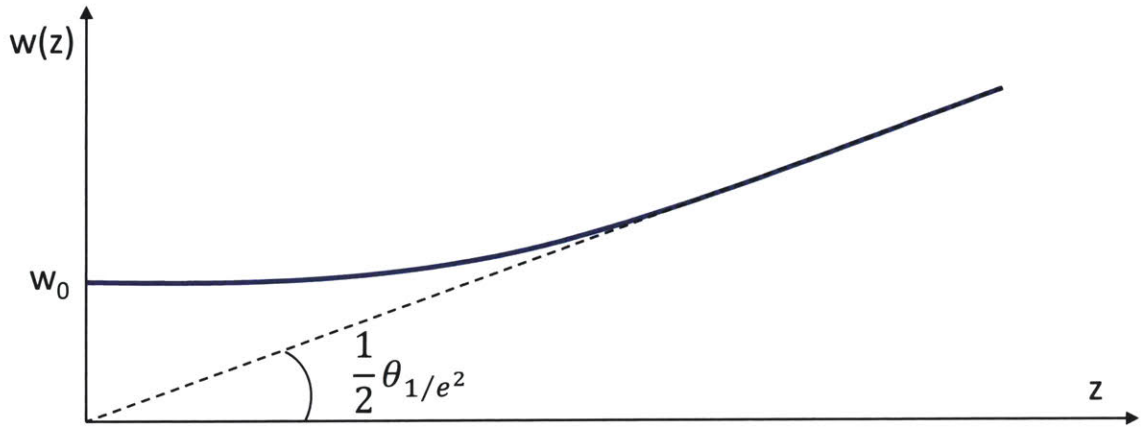

Figure 2-1: Gaussian Beam $1/e^2$ beam width and divergence angle geometry.

boundary at which the wavefront intensity drops to $1/e^2 \approx 13.5\%$ of its peak value on the optical axis. The minimum $1/e^2$ beamwidth is called the beam waist, with a radius denoted w_0. The $1/e^2$ full-width beam divergence angle, θ_{1/e^2} is defined with reference to the linear asymptotes of the beam width. The Gaussian beam intensity is parameterized in cylindrical-polar coordinates with respect to the optical axis as follows [25].

$$I(r,z) = I_0 \left(\frac{w_0}{w(z)}\right)^2 \exp\left(-\frac{2r^2}{w^2(z)}\right) \tag{2.1a}$$

$$w(z) = w_0\sqrt{1+(z/z_0)^2} \tag{2.1b}$$

$$z_0 = \frac{\pi w_0^2}{\lambda} = \frac{4\lambda}{\pi\theta_{1/e^2}^2} \tag{2.1c}$$

$$\theta_{1/e^2} = \frac{2\lambda}{\pi w_0} = \sqrt{\frac{2}{\ln(2)}}\theta_{\text{FWHM}} \tag{2.1d}$$

where $I_0 = 2P_0/(\pi w_0^2)$ is the reference intensity at the origin, P_0 is the reference power, $w(z)$ is the $1/e^2$ beam radius, z_0 is called the Rayleigh range, and θ_{FWHM} is FWHM beam divergence, which corresponds to an intensity of 50% of the on-axis value. These

relations are used to generate the transmit gain and pointing loss equations in the next section. See appendix A.2 for a derivation that relates the intensity equation to the transmit gain and pointing loss. In this section, the Gaussian beam intensity function was given with the definition of $1/e^2$ & FWHM beam divergences. The next section will describe the laser range equation, which is used to compute received power during a link.

2.2 The Laser Range Equation

The laser range equation is the equivalent of the radio range equation for optical transmitters and receivers and takes the same mathematical form with different details for the individual terms.

$$P_{\text{rx}} = P_{\text{tx}} G_{\text{tx}} G_{\text{rx}} L_{\text{path}} L_{\text{ptg}} L_{\text{opt,tx}} L_{\text{opt,rx}} L_{\text{atm}} \tag{2.2}$$

where P_{rx} is the power to the receiver sensor in Watts, P_{tx} is the power from the laser source in Watts, G_{tx} is the transmitter gain, G_{rx} is the receiver gain, L_{path} is the path loss, L_{ptg} is the pointing loss, $L_{\text{opt,tx}}$ and $L_{\text{opt,rx}}$ are the transmitter and receiver optical implementation losses, and L_{atm} is the atmospheric loss for uplinks and downlinks. The gain and loss terms are all dimensionless. The loss terms are all in the interval $(0, 1]$, which in decibels ($X_{dB} = 10\text{Log}_{10}(X)$) is $(-\infty, 0]$ dB. Simple equations can be given for some of the above terms as follows [3, 2]:

$$G_{\text{tx}} = \frac{32}{\theta_{1/e^2}^2} \tag{2.3a}$$

$$G_{\text{rx}} = \left(\frac{\pi D_{\text{rx}}}{\lambda}\right)^2 \tag{2.3b}$$

$$L_{\text{path}} = \left(\frac{\lambda}{4\pi z}\right)^2 \tag{2.3c}$$

$$L_{\text{ptg}} = \exp\left(-8\left(\frac{\theta}{\theta_{1/e^2}}\right)^2\right) \tag{2.3d}$$

where D_{rx} is the diameter of the receiver aperture and θ is the spherical-polar pointing angle relative to the optical axis. Equations 2.3a & 2.3d are derived in Appendix A.2. P_{tx}, $L_{\text{opt,tx}}$, & $L_{\text{opt,rx}}$ are parameters of the transmitting and receiving terminal hardware. L_{atm} is based on atmospheric modeling of absorption and scattering of the laser wavelength and is a function of distance that the beam travels within the atmosphere. A detailed discussion of atmospheric losses can be found in Hemmati et al. [2], and a discussion of uplink atmospheric losses can be found in in Nguyen [27]. For statistical modeling purposes, the terms in the range equation are random variables. General statistical link modeling for communications performance analysis is beyond the scope of this thesis. Methods for general statistical link modeling can be found in Clements [28].

This section briefly presented the laser communications range equation and its terms. Although a detailed link analysis is beyond the scope of this work, previous CLICK mission analysis indicates that a reasonable pointing loss upper bound requirement is -1.5 dB. This will be used as a point of comparison later on. In the following section, statistical models of pointing error and loss will be discussed.

2.3 Statistical Modeling of the Pointing Error & Loss

A pointing direction can be mathematically specified by a unit vector ($\mathbf{p}$), which has two degrees of freedom. These degrees of freedom can be parameterized by two angular coordinates (θ_x, θ_y), which are typically azimuth and elevation respectively, with $\theta_x \in (-\pi, \pi]$ and $\theta_y \in [-\pi/2, \pi/2]$, although the coordinates chosen can vary. This is illustrated in Figure 2-2, where the z-axis is the optical reference axis. We model Θ_x and Θ_y as Gaussian distributed random variables: $\Theta_x \sim N(\mu_x, \sigma_x)$ & $\Theta_y \sim N(\mu_y, \sigma_y)$, where μ_x & μ_y represent the sum of bias error contributions and σ_x & σ_y represent the RMS of the standard deviations of the error contributions. As the variables are bounded, the true distributions are also bounded; however, they are well approximated by unbounded Gaussian distributions for small angles (see Appendix A.3). The total angle (Θ) between the random pointing vector ($\mathbf{p}(\Theta_x, \Theta_y)$) and the

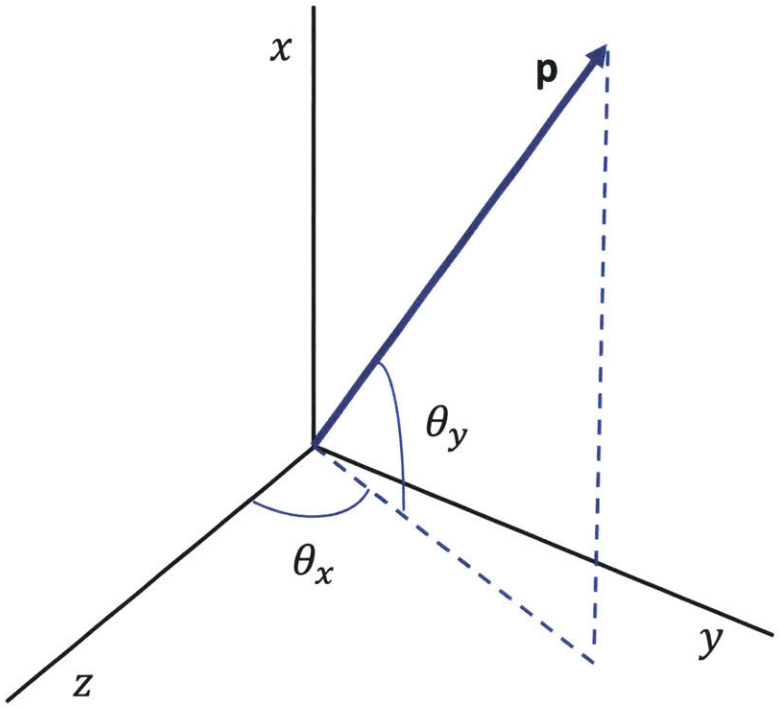

Figure 2-2: Spherical geometry of $\mathbf{p}$, θ_x, and θ_y. The reference optical axis is the z-axis.

optical axis (z) is determined by the spherical law of cosines:

$$\cos(\Theta) = \cos(\Theta_x)\cos(\Theta_y) + \sin(\Theta_x)\sin(\Theta_y)\cos(\pi/2) \tag{2.4a}$$

$$= \cos(\Theta_x)\cos(\Theta_y) \tag{2.4b}$$

And applying the small angle approximation for $\cos(x) = 1 - x^2/2 + O(x^4)$, $\Theta \approx \sqrt{\Theta_x^2 + \Theta_y^2}$. Next, assuming rotational symmetry about the optical axis and taking $\sigma = \sigma_x = \sigma_y$, it can be shown that $\Theta \sim \text{Rice}(\nu, \sigma)$, where $\nu = \sqrt{\mu_x^2 + \mu_y^2}$ and the Rice/Rician cumulative distribution function (CDF) is [29]:

$$\mathrm{P}[\Theta \leq \theta] = F_\Theta(\theta) = 1 - \mathrm{Q}_1\left(\frac{\nu}{\sigma}, \frac{\theta}{\sigma}\right) \tag{2.5}$$

where Q_1 is a Marcum Q-Function [29]:

$$Q_1(a,b) = \int_b^\infty x \exp\left(-\frac{x^2+a^2}{2}\right) I_0(ax)\,dx \tag{2.6}$$

where I_0 is the zeroth order modified Bessel function of the first kind [29]. Therefore, the expression for pointing error given a reliability expressed as a probability p_θ is

$$\theta = F_\Theta^{-1}(p_\theta) \tag{2.7}$$

where the inverse CDF of the Rice distribution is computed numerically. This equation can be used when evaluating a pointing budget for successful sensor acquisition, where the requirement is defined by the FOV or the FOR: $\theta < \theta_{\text{FOV/FOR}}/2 = \theta_{\text{HFOV/HFOR}}$.

Next, the equation for pointing loss is derived. From Equation 2.3d, the pointing loss in decibels is

$$L_{\text{ptg,dB}} = -80\text{Log}_{10}(e)\left(\frac{\Theta}{\theta_{1/e^2}}\right)^2 \tag{2.8}$$

Re-arranging this expression gives

$$-\frac{L_{\text{ptg,dB}}\theta_{1/e^2}^2}{80\text{Log}_{10}(e)} = \Theta^2 = \Theta_x^2 + \Theta_y^2 \tag{2.9}$$

Again, we assume rotational symmetry with regard to the axes with $\sigma = \sigma_x = \sigma_y$, $\mu = \mu_x = \mu_y$, & $\nu = \sqrt{2}\mu$. Then dividing both sides of Equation 2.9 by σ^2, we define the random variable A

$$A = -\frac{L_{\text{ptg,dB}}\theta_{1/e^2}^2}{80\text{Log}_{10}(e)\sigma^2} = \left(\frac{\Theta_x}{\sigma}\right)^2 + \left(\frac{\Theta_y}{\sigma}\right)^2 \tag{2.10}$$

Now, $(\Theta_x/\sigma) \sim N(\mu/\sigma, 1)$ and $(\Theta_y/\sigma) \sim N(\mu/\sigma, 1)$, which means A is distributed as a non-central chi-squared distribution with 2 degrees of freedom: $A \sim \chi_2^2(\nu^2/\sigma^2)$, with CDF [29]:

$$\text{P}[A \leq a] = F_A(a) = 1 - Q_1\left(\frac{\nu}{\sigma}, \sqrt{a}\right) \tag{2.11}$$

Now define $\tilde{L}_{\text{ptg,dB}} \equiv -L_{\text{ptg,dB}}$. $\tilde{L}_{\text{ptg,dB}}$ is a positive scaling of A, which means its CDF is

$$\mathrm{P}[\tilde{L}_{\text{ptg,dB}} \leq \tilde{l}] = F_{\tilde{L}}(\tilde{l}) = \mathrm{P}[c_A A \leq \tilde{l}] = \mathrm{P}[A \leq \tilde{l}/c_A] \tag{2.12a}$$

$$= 1 - Q_1\left(\frac{\nu}{\sigma}, \sqrt{\frac{\tilde{l}}{c_A}}\right) \tag{2.12b}$$

where (2.12c)

$$c_A = 80\mathrm{Log}_{10}(e)\left(\frac{\sigma}{\Theta_{1/e^2}}\right)^2 \tag{2.12d}$$

Hence, the the pointing loss in dB for a given reliability expressed as a probability p_l is

$$l_{\text{ptg,dB}} = -\tilde{l} = -F_{\tilde{L}}^{-1}(p_l) = -c_A F_A^{-1}(p_l) \tag{2.13}$$

which can be computed using numerical methods for the inverse CDF of the non-central chi-squared distribution. An alternative model of the pointing error arises when the mean error μ is negligible, which yields the Rayleigh distribution: Rayleigh(σ) = Rice(0,σ). See Appendix A.4 for details on this model and the corresponding pointing loss function.

In this section, the Rice/Rician model of the total pointing error and the non-central chi-squared model of the pointing loss were derived based on Gaussian models of the single-axis pointing errors. In the next section, these models will be applied to the system's analysis tool called a pointing budget in the context of the CLICK B/C mission.

2.4 Pointing Budgets

As part of systems analysis, pointing error statistics are estimated by considering the end-to-end systems performance and how each subsystem adds error to the pointing process. In preliminary design, these statistics can be estimated a priori using simplified models or past experience. In later project stages, the errors can be statistically analyzed in detail using simulations and experimental test results. The pointing error model is used to evaluate PAT performance with respect to two metrics: one, sensor acquisition as per the FOV or FOR; and two, link loss for use in link budgets. Each pointing budget element represents a single-axis Gaussian error component, with the total single axis error being the sum of these Gaussian random variables:

$$\Theta_{\text{x (or y)}} = \sum_{i=1}^{N} \Theta_i \tag{2.14a}$$

$$\Theta_i \sim N(\mu_i, \sigma_i),\ \Theta_{\text{x (or y)}} \sim N(\mu, \sigma) \tag{2.14b}$$

$$\mu = \sum_{i=1}^{N} \mu_i,\ \sigma = \sqrt{\sum_{i=1}^{N} \sigma_i^2} \tag{2.14c}$$

In this section, the pointing budgets for CLICK B/C body pointing using GPS-based relative navigation for LEO crosslink and downlink are given in Tables A.1 & 2.3, respectively. Additional CLICK B/C pointing budgets can be found in Appendix A.6.

2.4.1 Relative Navigation Error

For use in the pointing budgets, we use the relative navigation error data from Chapter 3, with the crosslink corresponding to the second row of Tables 3.11 & 3.12 and the downlink corresponding to row 4 of Table 3.13. The crosslink data corresponds to on-board propagation of unfiltered GPS position and velocity fixes with a Host propagation interval of 1 minute and a Target propagation interval of 10 minutes. The downlink data corresponds to the same Host configuration with the Target being generated via application of an Earth rotation model to the stored

geodetic coordinates of the optical ground station. Chapter 3 will have a detailed discussion of the relative navigation analysis for these results and the results for other relative navigation configurations. The relative navigation two axis angle error (Θ) distribution for crosslink is shown in Figure 2-3. The Rice distribution fit parameters for 25 km range are $\nu = 19.512$ μrad ($\mu = \nu/\sqrt{2} = 13.797$ μrad) and $\sigma = 343.127$ μrad. The Rice distribution fit parameters for 580 km range are $\nu = 0.00157$ μrad ($\mu = \nu/\sqrt{2} = 0.00112$ μrad) and $\sigma = 20.435$ μrad. The

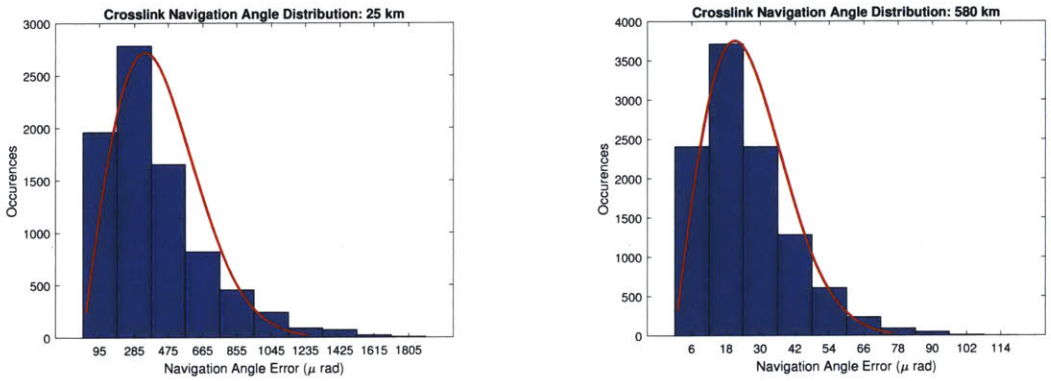

Figure 2-3: Navigation error distributions for minimum and maximum CLICK crosslink ranges using unfiltered GPS measurements corresponding to the second row of Tables 3.11 & 3.12

relative navigation two axis angle error (Θ) distribution for downlink is shown in Figure 2-4, and the Rice distribution fit parameters are $\nu = 4.369 \times 10^{-5}$ μrad ($\mu = \nu/\sqrt{2} = 3.089 \times 10^{-5}$ μrad) and $\sigma = 2.674$ μrad. In this section, the Rice distribution parameters were given for a particular configuration for crosslink & downlink relative navigation. For crosslinks, GPS fixes were directly propagated with a Host propagation interval of 1 minute and a target propagation interval of 10 minutes. For downlink, the Host propagation interval was also 1 minute, with the target position being measured using GPS and propagated with an IAU-00/06 B earth rotation model. This is representative of conservative CLICK B/C operations. Kalman filtering will not be applied in the CLICK mission for on-board relative navigation. Specific details of these results and results for other relative navigation configurations will be discussed in Chapter 3. Kalman filtering and its effects will be the subject of Chapter 4.

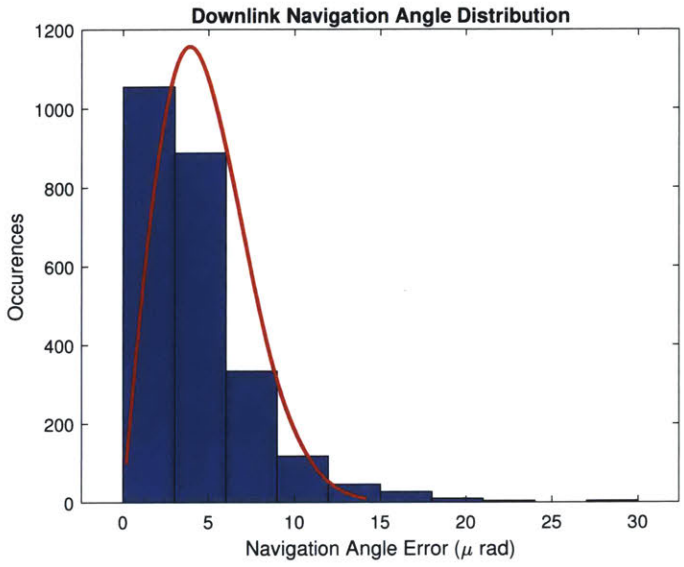

Figure 2-4: Navigation error distribution CLICK downlink using unfiltered GPS measurements corresponding to the fourth row of Table 3.13

2.4.2 Point Ahead Error

The relative velocity of the spacecraft orthogonal to the direction of the beam axis causes a pointing error due to the finite speed of light. This is called the point-ahead error, and the formula is given below [3]:

$$\theta_{\mathrm{PA}} = \frac{2v_{\mathrm{rel,orth}}}{c} \tag{2.15a}$$

$$v_{\mathrm{rel,orth}} = ||\mathbf{v}_{\mathrm{rel}} - (\mathbf{v}_{\mathrm{rel}}, \mathbf{p})\mathbf{p}|| = ||\omega_{\mathrm{rel}} \times \mathbf{p}|| \tag{2.15b}$$

$$\mathbf{v}_{\mathrm{rel}} = \mathbf{v}_{\mathrm{T}} - \mathbf{v}_{\mathrm{H}} \tag{2.15c}$$

$$\mathbf{p} = \mathbf{r}_{\mathrm{rel}}/||\mathbf{r}_{\mathrm{rel}}|| \tag{2.15d}$$

$$\mathbf{r}_{\mathrm{rel}} = \mathbf{r}_{\mathrm{T}} - \mathbf{r}_{\mathrm{H}} \tag{2.15e}$$

where θ_{PA} is the point ahead angle $(\mathbf{r}_{\mathrm{T}}, \mathbf{v}_{\mathrm{T}})$ are the position and velocity of the target, $(\mathbf{r}_{\mathrm{H}}, \mathbf{v}_{\mathrm{H}})$ are the position and velocity of the host, $\mathbf{p}$ is pointing line of sight direction vector, and c is the speed of light in vacuum. Some terminal designs implement an independent FSM called a point-ahead mirror (PAM) to correct for this error based on relative navigation data. Due to SWaP restrictions, the CLICK B/C terminals

do not implement a PAM and will simply accept this error. The following sections present simulation results for point-ahead error for CLICK crosslinks and downlinks.

LEO Intra-Orbit Point Ahead Error

Figure 2-5 summarizes the statistical results for 99$^{\text{th}}$ percentile point-ahead angles for intra-orbit crosslinks in LEO. The leader and follower satellites share the same orbital elements except that they are separated by some inter-satellite range. The point-ahead angle is well described by a power-law function of the range (d), which is fit using least squares: $\theta_{PA,99\%}(\mu\text{rad}) = (7.249 \times 10^{-3})(d(\text{km}))^{0.997}$. The point ahead increases with increasing range, and the 99$^{\text{th}}$ percentile point-ahead angle for the minimum CLICK range of 25 km is 0.180 μrad and for the maximum CLICK range of 580 km is 4.175 μrad. The distributions for 25 km and 580 km ranges

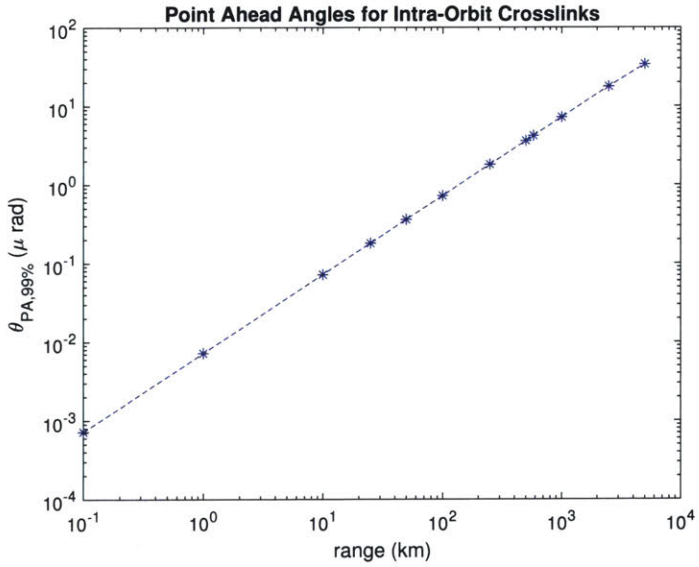

Figure 2-5: Logarithmic plot of 99$^{\text{th}}$ percentile point-ahead angles over various intra-orbit ranges (e.g., string of pearls configuration) for near circular ($e = 0.005$) LEO orbits.

are shown below. The Rice distribution fit parameters for 25 km are $\nu = 0.178$ μrad ($\mu = \nu/\sqrt{2} = 0.126$ μrad) and $\sigma = 0.00132$ μrad. The Rice distribution fit parameters for 580 km are $\nu = 4.117$ μrad ($\mu = \nu/\sqrt{2} = 2.911$ μrad) and $\sigma = 0.0313$ μrad. In this section, the point ahead errors for LEO intra-orbit crosslink ranges between 0.1 &

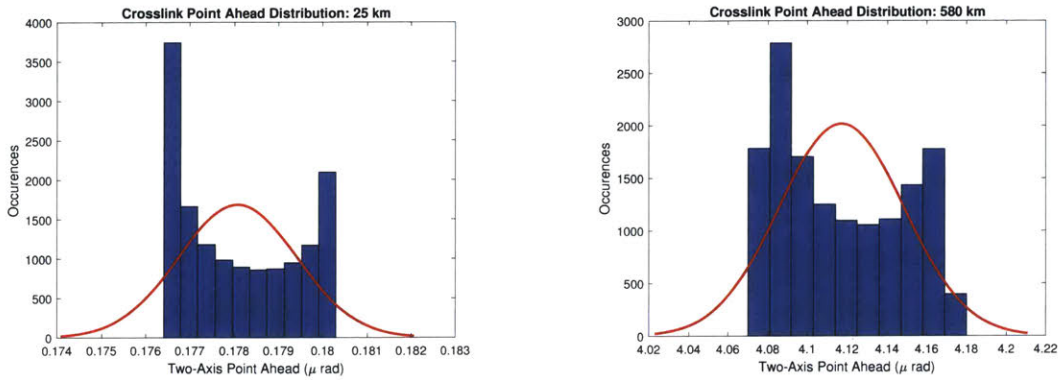

Figure 2-6: Point-ahead error distributions for minimum and maximum CLICK crosslink ranges.

5000 km were given along with a power-law to describe how point ahead error grows with increasing range. Additionally, the Rice distribution parameters for the CLICK minimum and maximum ranges of 25 & 580 km. These distribution parameters will be used in the pointing budget analysis later on.

LEO Downlink Point Ahead Error

Table 2.1 summarizes the point-ahead angle statistics for LEO downlinks for 9 different orbits that span the LEO orbits of interest: 400 km, 500 km, & 600 km altitudes; 35°, 51.6°, & 82-83° inclination (sun-synchronous inclination is a function of the altitude). The orbits are propagated over 180 days using a J_2 propagator to cover all possible RAAN values and hence all possible downlink geometries for each of the 9 orbits. What is apparent is that there is not a significant statistical difference between the 99^{th} percentile point ahead angles for the different ground stations across the Continental U.S. (CONUS) and for the different orbits. The 99^{th} percentile point ahead angle across all orbits and all ground station locations is 50.36 μrad. The distribution is shown in Figure 2-7, which is used to compute the result for the downlink pointing budget (Table 2.3), and the Rice distribution fit parameters are $\nu = 34.624$ μrad ($\mu = \nu/\sqrt{2} = 24.483$ μrad) and $\sigma = 9.859$ μrad. In this section, the point ahead errors for downlinks from 9 different LEO orbits to 3 different ground locations across CONUS were given. Notably, the point-ahead errors were similar across these cases,

Table 2.1: 99^{th} percentile point ahead angles for CLICK-type LEO downlinks. Simulation over 180 days using J_2 model (for orbital precession) from epoch Jan 01 2019 00:00:00.000 UTC. Reference geodetic coordinates (Latitude, Longitude): Boston (42.360636°, −71.093418°), Boulder (40.006891°, −105.264983°), Los Angeles (34.068851°, −118.444692°).

Altitude (km)	Inclination (°)	θ_{PA} (μrad) Boston	θ_{PA} (μrad) Boulder	θ_{PA} (μrad) Los Angeles
400	35	49.10	49.05	48.92
400	51.6	49.59	49.55	49.47
400	82.84	51.24	51.25	51.12
500	35	48.76	48.72	48.58
500	51.6	49.29	49.24	49.15
500	82.47	50.98	50.72	50.82
600	35	48.44	48.38	48.26
600	51.6	49.00	48.96	48.86
600	82.07	50.58	50.57	50.48

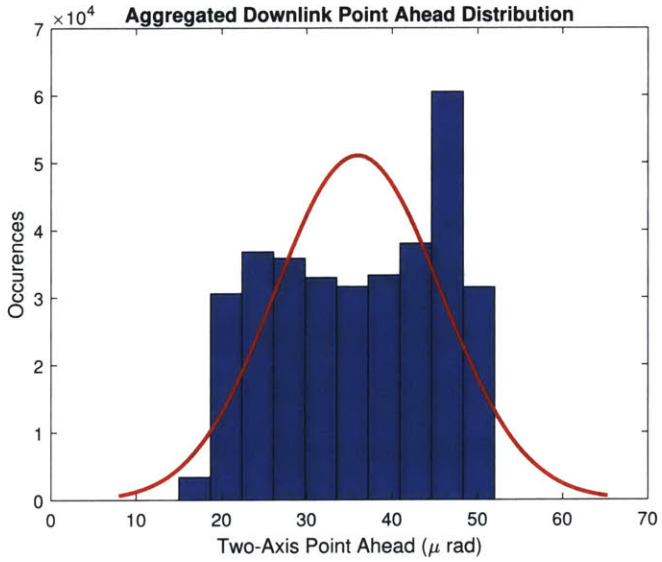

Figure 2-7: Distribution of point ahead angles for all 9 LEO orbits and all 3 ground stations used in Table 2.1.

and the Rice distribution fit parameters for the point ahead errors aggregated across all cases were given. These will be used in the sequel for pointing budget analysis.

2.4.3 Crosslink Relative Navigation Body Pointing Budget

Table 2.2 gives the pointing loss budget for GNSS-based body pointing for crosslinks. The pointing error budget terms include relative navigation error & point ahead error discussed in the previous two sections. Additional error terms include assembly & calibration, which is based on the residual knowledge error of the beacon laser axis direction in the spacecraft body frame following assembly & calibration on the ground. Additional details on this type of error can be found in [24]. The launch shift is due to vibration of the payload during launch, which has the potential to shift the mounted components within any assembly. Additional details on this type of error can be found in [24, 30]. The thermoelastic deformation primarily comes from thermal gradients and temperature fluctuations from solar heating and cooling cycles that naturally occur on each orbit. This causes the structure to deform, and the major structure of relevance here is the spacecraft structure defining the relative geometry between the payload apertures and the spacecraft star tracker, which defines the spacecraft's body frame. The magnitude of this effect for the CLICK B/C beacon was analyzed in detail in Yenchesky et al. using finite element analysis [24]. Spacecraft body pointing error is caused by residual attitude control error and mechanical vibrations in the spacecraft structure induced by the attitude control actuator (a reaction wheel system). The value used here comes from the system requirement levied on the CLICK B/C spacecraft bus, which is provided by Blue Canyon Technologies. The previous on-orbit performance of this spacecraft bus is described by Mason et al. for the Min-XSS mission [31]. In this section, the pointing budget for crosslink relative navigation based body pointing was given for the CLICK minimum & maximum ranges of 25 & 580 km. The 99.7% total pointing errors were 1988.9 μrad & 1609 μrad, respectively. And the corresponding 99.7% pointing losses were -0.278 dB & -0.182 dB, with corresponding margins of 1.222 dB & 1.318 dB compared to the -1.5 dB required worst case pointing loss bound. Chapters 3 & 4 will focus on the relative navigation error component of this budget and the corresponding downlink budget in the next section. For the purposes of comparison, the results used for this

Table 2.2: Pointing error budget for body pointing of crosslink beacon laser prior to optical feedback using direct propagation of GPS measurements. See Section 2.4.1 for relative navigation. See Section 2.4.2 for point-ahead.

Budget Element	25 km range		580 km range	
	μ (μrad)	σ (μrad)	μ (μrad)	σ (μrad)
Relative Navigation	13.80	343.1	0.001	20.44
Point Ahead	0.126	0.001	2.911	0.031
Assembly & Calibration	0.000	434.5	0.000	434.5
Launch Induced Shift	0.000	161.6	0.000	161.6
Thermal Deformation	0.000	16.16	0.000	16.16
Spacecraft Body Pointing	0.000	87.42	0.000	87.42
Total	13.92	583.3	2.912	472.2
θ_{1/e^2} (μrad)	22235			
θ_{ptg} (μrad, $p_\theta = 0.997$)	1988.9		1609.5	
$L_{\text{ptg,dB}}$ (dB, $p_l = 0.997$)	-0.278		-0.182	

case are regarded as the baseline with which other relative navigation configurations will be compared. The main comparison metric will be the 99^{th} percentile angular relative navigation error, which are 1367 μrad & 76.58 μrad for the 25 km and 580 km cases, respectively.

Furthermore, in order to be able to directly relate angular error percentiles that will be generated in later sections for different relative navigation configurations to pointing loss percentiles without needing bias error, the Rayleigh approximation is useful (see Appendix A.4). For the crosslink relative navigation pointing budget, this approximation of the pointing error and loss is accurate as $\nu/\sigma < 0.03$ in both cases. Using only the total σ value in both cases (583.3 μrad and 472.2 μrad) as the Rayleigh parameter in Equation A.12 yields the same (within roundoff) 99.7% pointing losses of -0.278 dB and -0.182 dB for 25 km and 580 km, respectively. This method will be used in later sections to compare the pointing losses incurred by different relative navigation errors (the Rayleigh parameter is computed from percentile data using Equation A.8a).

2.4.4 Downlink Relative Navigation Body Pointing Budget

The next pointing budget shown in Table 2.3 is for the downlink, with new parameters for relative navigation and point ahead from the results given in previously. Also note the change to the quadcell as the stage 2 sensor as explained previously, which also changes the assembly & calibration error value. The other budget elements are the same as in the crosslink case. In this section, the pointing budget for relative

Table 2.3: Pointing error budget for body pointing of downlink beacon laser using direct propagation of GPS measurements. See Table 3.13 for relative navigation. See Section 2.4.2 for point-ahead.

Budget Element	μ (μrad)	σ (μrad)
Relative Navigation	3×10^{-5}	2.674
Point Ahead	24.483	9.859
Assembly & Calibration	0	443.5
Launch Induced Shift	0	161.6
Thermal Deformation	0	16.16
Spacecraft Body Pointing	0	87.42
Total	24.48	480.4
θ_{1/e^2} (μrad)	22253	
θ_{ptg} (μrad, $p_\theta = 0.997$)	1639.7	
$L_{\text{ptg,dB}}$ (dB, $p_l = 0.997$)	-0.189	

navigation based body pointing for the CLICK B/C downlink was given. The 99.7% total pointing error was 1639.7 μrad. And the corresponding 99.7% pointing loss was $-0.189dB$ with a corresponding margin of 1.311 dB compared to the -1.5 dB required worst case pointing loss bound. Again, for later comparison with other relative navigation configurations, the 99^{th} percentile angular relative navigation error for this configuration is 17.29 μrad. The next section will discuss the operational availability of crosslinks and downlinks.

Again, the Rayleigh pointing model will be used in later sections to approximate the Rice model to compare pointing losses for different relative navigation configurations. For the downlink budget here, this approximation of the pointing error and loss is still accurate despite the increased bias due to point ahead error: $\nu/\sigma = 0.07$. Using $\sigma = 480.4$ μrad in Equation A.12 again yields the same (within roundoff) 99.7% pointing losses of -0.189 dB.

2.5 Link Access Analysis

2.5.1 Crosslink Access Analysis

The CLICK crosslink is conducted between satellites sharing the same orbit but separated by ranges between 25 km and 580 km. Therefore, unlike downlinks, this type of crosslink is geometrically possible at any time. However, as discussed previously, the CLICK terminal utilizes a monocular camera as part of its PAT system, which cannot operate when the Sun is within its keep-out zone. The CLICK camera is equipped with a baffle that is design for 45° to 50° solar keep-out, half-angle. Therefore, the crosslink access duration is computed with STK using the solar keep-out as the determining factor. Additional keep-out angles are also analyzed for alternative terminal designs. Note that a smaller keep out angle requires a longer baffle, which means the minimum keep-out angle is limited by the volume requirement of the terminal. The CLICK volume prevents a baffle with a keep out angle smaller than 45°. Figure 2-8 shows the lower bound crosslink access durations for 99% of links (e.g. the 1^{st} percentile). The CLICK baffle geometry access durations are at least 21 minutes (99%), which meets the mission need of up to 15 minutes. Although the 3U spacecraft volume precludes smaller keep-out angles, larger nanosatellites like 6U cubesats could potentially have smaller keep out angles. Moreover, there is alternative approach to mitigating stray light from the Sun and other environmental sources: modulate the laser source and electronically bandpass filter the received signal. This is done on CLICK for the fine pointing system with the quadcell via its FPGA interface. It is possible to do this using a camera sensor; however, a custom FPGA implementation must be implemented, which is not practical with the COTS CLICK camera. However, this may be useful in future terminal designs.

In this section, the crosslink access duration was analyzed based on solar keep out constraints between 20° & 75° for three different orbital inclinations of near-circular LEO orbits. The CLICK keep out constraint of 45° to 50° corresponded to an access duration of at least 21 minutes for 99% of cases, which meets the mission requirement of 15 minutes.

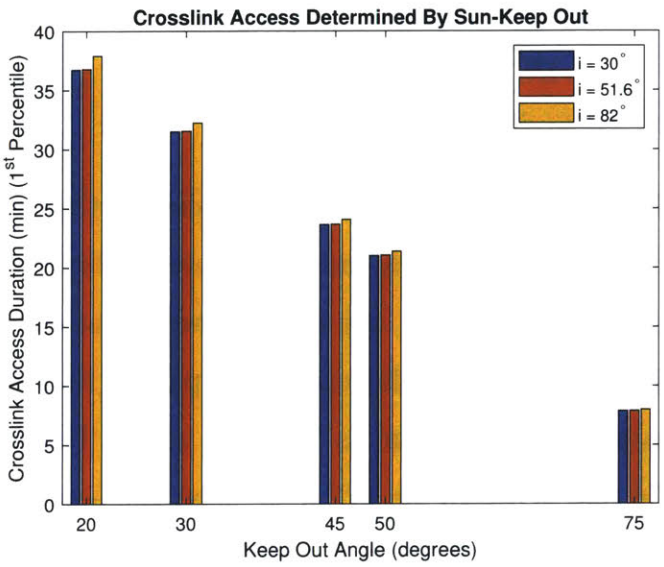

Figure 2-8: Crosslink access durations as determined by various Sun keep-out angles. The statistic plotted is the 1st percentile of the data aggregated, which means that 99% of the access intervals are greater than this value. The orbits computed are near-circular (e = 0.005) at 500 km altitude over three different inclinations (the results for 400 km and 600 km are not significantly different).

2.5.2 Downlink Access Analysis

Figure 2-9 is a comprehensive statistical analysis of downlink ranges from 9 different LEO orbits aggregated over 3 different ground station locations across the continental U.S. (CONUS). Each figure shows the percentile contours for all overpass data for each orbit. The simulation is over a period of 180 days with a J_2 propagator for orbital precession to run the RAAN through 360° to capture all downlink geometries for each orbit. The access interval limits are defined via geometric access in STK with a zero minimum elevation angle for the ground station. Table 2.4 summarizes the median overpass durations for each orbit. In practice, the OGS minimum elevation angle will be vary depending on the obstacles in the surrounding area (e.g. mountains, buildings, etc.), which means that the link durations will be further limited. For example, a similar analysis using a minimum elevation angle of 15° yields a median overpass duration for CONUS ground stations of 5.2 minutes. Figure 2-9 can be used to look up the minimum and maximum range for arbitrary link durations. For

CLICK, a downlink duration up to 1 minute will conservatively meet the science data needs to validate the data rate objective of at least 10 Mbps. Table 2.5 summarizes

Table 2.4: Median (50^{th} percentile) downlink durations (min) corresponding to Figure 2-9.

Orbit	Duration (min) Boston	Duration (min) Denver	Duration (min) LA
h_p = 400 km, i = 35 °	9.57	10.05	10.80
h_p = 400 km, i = 51.6 °	10.53	10.19	9.29
h_p = 400 km, i = 82.8 °	9.45	9.38	9.41
h_p = 500 km, i = 35 °	11.01	11.41	12.20
h_p = 500 km, i = 51.6 °	11.94	11.64	10.79
h_p = 500 km, i = 82.5 °	10.18	11.17	10.37
h_p = 600 km, i = 35 °	12.29	12.74	13.55
h_p = 600 km, i = 51.6 °	13.27	13.00	12.15
h_p = 600 km, i = 82.0 °	11.74	11.74	11.74

the median minimum ranges for each orbit (e.g. the minima of the 50% curves in Figure 2-9). In this section, LEO downlink access analysis results were summarized for 9 different orbits and 3 different ground stations across CONUS. The median downlink durations for zero minimum ground station elevation angle were between 9.38 & 13.55 minutes for perigee altitudes between 400 & 600 km. A similar analysis with a 15° minimu, ground station elevation angle yields a median downlink duration of 5.2 minutes for a perigee altitude of 500 km. The median minimum downlink ranges were between 995.9 km and 1630 km with the mid-range ISS inclination of 51.6° having the minimum ranges to CONUS. The Sun-Synchronous orbit inclinations of 82-83° had the maximium ranges to CONUS.

Table 2.5: Median (50^{th} percentile) minimum downlink ranges (km) corresponding to Figure 2-9

Inclination (°)	Min. Range (km, 50%), h_p = 400 km	Min. Range (km, 50%), h_p = 500 km	Min. Range (km, 50%), h_p = 600 km
35	1307.3	1426.1	1532.7
51.6	995.9	1066.7	1146.7
82-83	1310.6	1547.8	1630.0

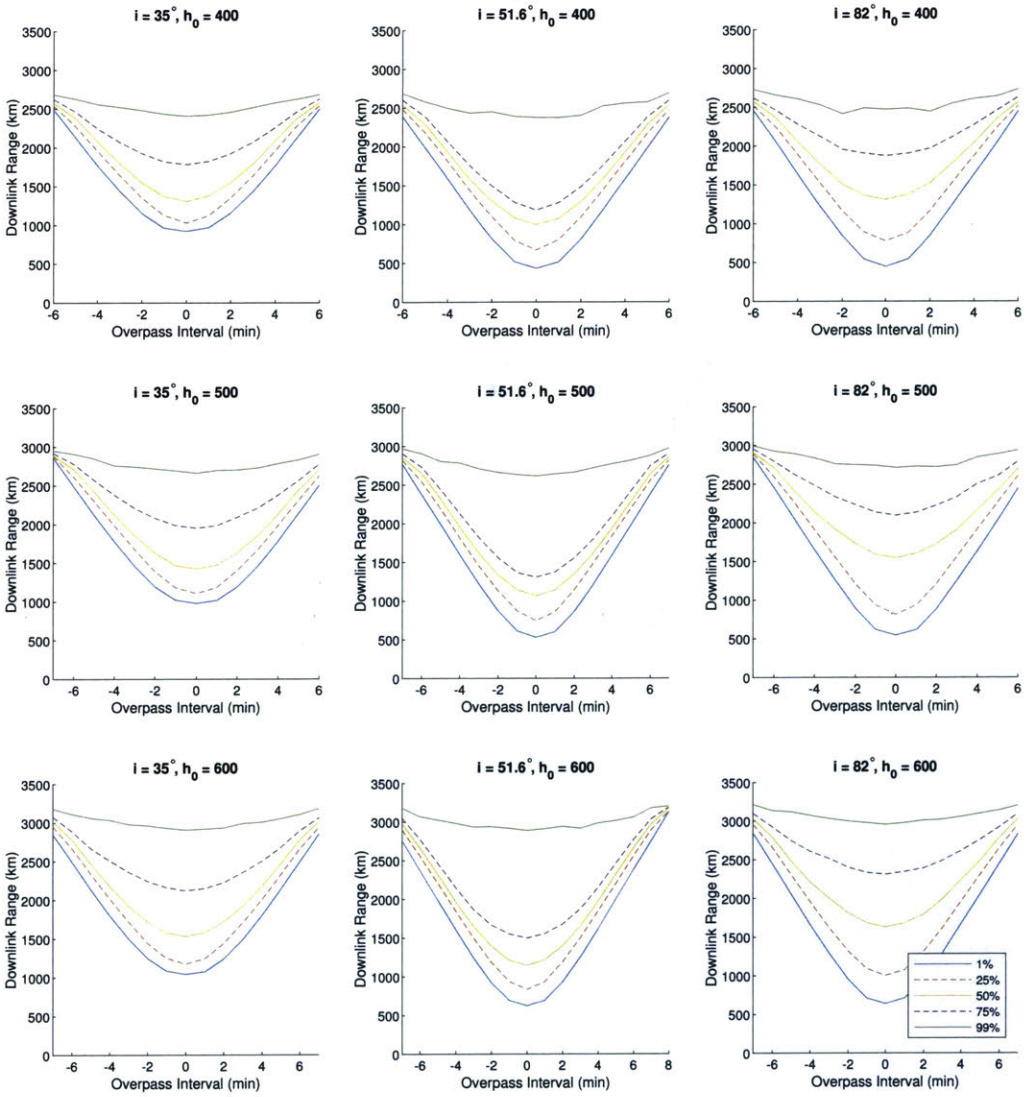

Figure 2-9: Percentiles of downlink overpass ranges for 9 different near circular (e = 0.005) LEO orbits with given inclinations and initial altitudes. Reference geodetic coordinates (Latitude, Longitude): Boston (42.360636°, − 71.093418°), Boulder (40.006891°, − 105.264983°), Los Angeles (34.068851°, − 118.444692°).

2.6 Chapter 2 Summary

In Section 2.1, the Gaussian beam intensity function was given with the definition of $1/e^2$ & FWHM beam divergences. Next in Section 2.2, the laser communications range equation and its terms were briefly presented, leading into Section 2.3's derivations for the Rice/Rician model of the total pointing error and the non-central chi-squared model of the pointing loss based on Gaussian models of the single-axis pointing errors. Following this, in Section 2.4.1, the pointing error model was applied to find distribution parameters for relative navigation for a particular configuration for crosslink & downlink relative navigation corresponding to CLICK B/C operations. Next, in Section 2.4.2, the pointing error model was also applied to find distribution parameters for point ahead error crosslinks and downlinks, which is the error due to the finite speed of light and the relative motion of the two terminals. Notably, the crosslink point ahead errors increased as a power law of the range, and the downlink point-ahead errors were similar across altitudes of 400-600 km, inclinations of 35° to 83°, and three different CONUS ground stations from Southern California to Massachusetts.

Following this, in Section 2.4.3, these distribution parameters as well as parameters for other error terms were used in pointing budgets for CLICK B/C body pointing using GPS-based relative navigation for LEO crosslink and downlink. The pointing budget for crosslink relative navigation based body pointing was given in in Table A.1 for the CLICK minimum & maximum ranges of 25 & 580 km. The 99.7% total pointing errors were 1988.9 μrad & 1609 μrad, respectively. And the corresponding 99.7% pointing losses were -0.278 dB & -0.182 dB, with corresponding margins of 1.222 dB & 1.318 dB compared to the -1.5 dB required worst case pointing loss bound. Chapters 3 & 4 will focus on the relative navigation error component of this budget and the corresponding downlink budget in the next section. For the purposes of comparison, the results used for this case are regarded as the baseline with which other relative navigation configurations will be compared. The main comparison metric will be the 99^{th} percentile angular relative navigation error, which are 1367 μrad

& 76.58 μrad for the 25 km and 580 km cases, respectively.

Next, in Section 2.4.4, the pointing budget for relative navigation based body pointing for the CLICK B/C downlink was given in Table 2.3. The 99.7% total pointing error was 1639.7 μrad. And the corresponding 99.7% pointing loss was -0.189 dB with a corresponding margin of 1.311 dB compared to the -1.5 dB required worst case pointing loss bound. Again, for later comparison with other relative navigation configurations, the 99^{th} percentile angular relative navigation error for this configuration is 17.29 μrad.

Finally, link access analyses for crosslink and downlink were given in Sections 2.5.1 & 2.5.2, respectively. The crosslink access duration was analyzed based on solar keep out constraints between 20° & 75° for three different orbital inclinations of near-circular LEO orbits. The CLICK keep out constraint of 45° to 50° corresponded to an access duration of at least 21 minutes for 99% of cases, which meets the mission requirement of 15 minutes. The LEO downlink access analysis results were summarized for 9 different orbits and 3 different ground stations across CONUS. The median downlink durations for zero minimum ground station elevation angle were between 9.38 & 13.55 minutes for perigee altitudes between 400 & 600 km. A similar analysis with a 15° minimu, ground station elevation angle yields a median downlink duration of 5.2 minutes for a perigee altitude of 500 km. The median minimum downlink ranges were between 995.9 km and 1630 km with the mid-range ISS inclination of 51.6° having the minimum ranges to CONUS. The Sun-Synchronous orbit inclinations of 82-83° had the maximium ranges to CONUS.

The next chapter will proceed with a detailed discussion and analysis of orbit propagation and GPS-based orbit determination for relative navigation. This will include the CLICK B/C configuration used here as well as other possible configurations for comparison and reference during future mission development.

Chapter 3

GNSS-Based Relative Navigation in LEO

Relative navigation is accomplished via kinematic knowledge of the terminal's host satellite as well as the target terminal, be it another satellite or a ground station. Satellite navigation requires orbit determination and propagation, which has a long history in spacecraft engineering. Onboard satellite orbit determination in LEO commonly utilizes a global navigation satellite system (GNSS) receiver, which enables orbit determination without additional sensors. The US Global Positioning System (GPS) is one of the GNSS constellations in place and the one being utilized in this work. GPS measurements are used to generate an orbit state and epoch that is then propagated forward in time using a propagation algorithm. A block diagram that describes the relative navigation configuration for this chapter and chapter 4 is shown in Figure 3-1.

The analysis considered here derives from the baseline mission operation for the CLICK satellites, which is a cross link between two satellites which are roughly in the same LEO near-circular orbit at altitudes from 400-600 km separated by ranges from 25 km to 580 km. The orbit determination measurements are taken from onboard GPS receivers. The epoch and state is communicated between the satellites and some interval of time passes before they are used. The receiving terminal propagates the orbit forward prior to using the orbit state data for an acquisition attitude manuever.

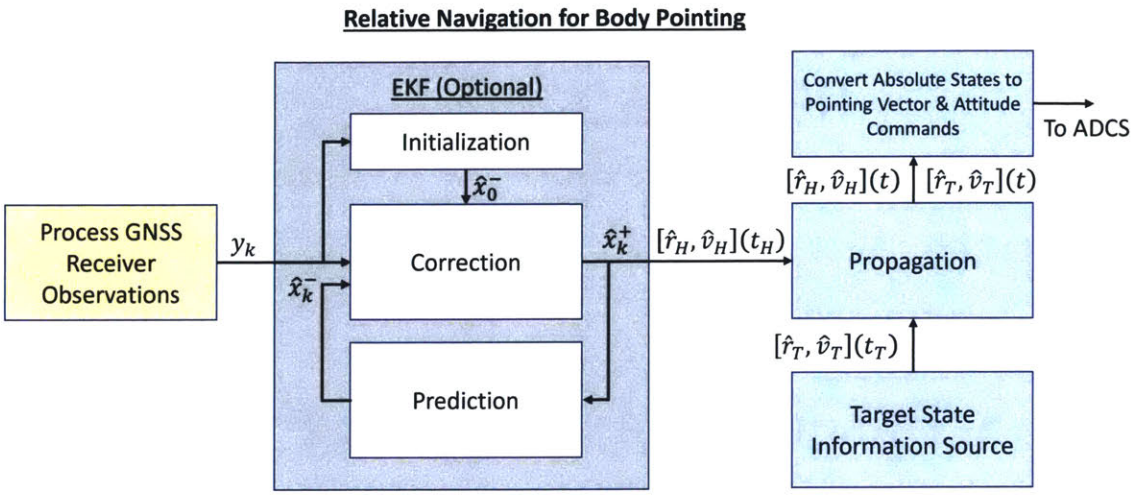

Figure 3-1: Block Diagram of Relative Navigation for Body Pointing Configuration

The smallest time interval that can be expected involves the direct RF transfer of the epoch and state information between the satellites. The time interval before use in this case can be on the order of seconds; however, operations are simplified and power usage is reduced if the acceptable delay can be increased to minutes or more. Other methods of orbit data communications include indirect methods such as over satellite communications networks like Globalstar with delays of seconds to a few minutes [32] and over ground networks with delays of tens of minutes or more. Hence, the potential propagation interval range considered here is over a range of 3 orders of magnitude from $10^0 - 10^3$ seconds.

If an Extended Kalman Filter (EKF) is used, it runs aboard each spacecraft and processes only the spacecraft's own GPS measurements (the Host measurements) to generate state estimates. These estimates are then transferred from the Host to the Target spacecraft, and the Target spacecraft simply propagates them forward. Therefore, each spacecraft is only running one EKF algorithm with a state dimension of 6 with a maximum sampling interval corresponding to the maximum Host propagation interval. The implementation of an EKF for onboard orbit determination will be the subject of Chapter 4.

The motivating example is navigation for nanosatellites in LEO using on-board

GPS measurement data for the purposes of line of sight determination for crosslinks and downlinks. The line of sight is specified by the unit direction vector from the host to the target, which we will refer to as the pointing vector:

$$\mathbf{p} = \frac{\mathbf{r}_T - \mathbf{r}_H}{\|\mathbf{r}_T - \mathbf{r}_H\|} \tag{3.1}$$

where $\mathbf{r}_T$ is the target position vector and $\mathbf{r}_H$ is the host satellite's position vector. The initial acquisition objective is to point the boresight of the laser terminal along the pointing vector for a specified period of time. Computing these pointing vectors is done by estimating the host and target positions over this interval, which is done as follows. The first step is to process the GPS measurement data into an estimate of the host and target states: $\hat{\mathbf{x}}_H(t_H)$ and $\hat{\mathbf{x}}_T(t_T)$. The next step is to propagate the host and target states from the estimate times t_H & t_T through the Host and Target measurement intervals Δt_H & Δt_T to the next anticipated measurement times. The predicted positions at intermediate times (t) are used to determine the relative navigation attitude commands for body pointing.

This process can be completed using two algorithms: 1) the measurement data processing algorithm & 2) the propagation algorithm. This chapter will first analyze the state propagation algorithm in depth. The later sections will discuss how GPS position & velocity fixes are generated and their noise properties. Finally, these algorithms will be combined to estimate the relative navigation error by directly propagating GPS fixes. In Chapter 4, extended Kalman filtering algorithms will be explored to reduce the state estimation error contributed by GPS measurement noise. It should be noted that state propagation is an essential subroutine for Kalman filtering, so this chapter sets the groundwork for Chapter 4's discussion of Kalman filtering algorithms.

3.1 State Propagation Background

For CLICK, both satellites are in similar low-Earth orbits, so the same orbit propagation algorithm is used for each of them. In the case of a laser downlink only, the host is a satellite and, in this application, the target is a ground station that is fixed with respect to the Earth's surface for the duration of the link. The ground target state propagation problem is thus equivalent to an Earth rotation model. The background and approaches for orbit propagation and Earth rotation modeling will be discussed in detail in the following two sections.

3.1.1 Orbit Propagation Background

Orbit propagation is an initial value problem (IVP): it is the problem of determining the state of a satellite at some future time, $\mathbf{x}(t_0 + \Delta t)$, given the state of the satellite at some initial time, $\mathbf{x}(t_0)$, by integrating the equations of state. The equations of state are defined as follows:

$$\dot{\mathbf{x}} = \begin{bmatrix} \dot{\mathbf{r}} \\ \dot{\mathbf{v}} \end{bmatrix} = \begin{bmatrix} \mathbf{v} \\ -\frac{\mu}{\|\mathbf{r}\|^3}\mathbf{r} + \mathbf{a}_p \end{bmatrix} \tag{3.2}$$

where $\mathbf{a_p}$ is the total perturbation acceleration, which is added to the Kepler two body gravitational term. The units used are km, km/s, and km/s^2 unless otherwise specified. Cowell's method for orbit propagation is direct numerical integration of eq. (3.2) given an initial state [33]. There are also other methods. For example, Encke's method integrates the deviations from a reference analytically determined orbit. Analytical methods can also be used alone. The simplest analytical propagator is the Kepler propagator, which solves the reduced two-body problem [33]. More complex analytical methods include the commonly used Simplified General Perturbations 4 (SGP4) propagator, which relies on state and model parameter estimates generated by JSpOC, called Two-Line Elements (TLEs) [33]. Although SGP4 is a fairly high accuracy analytic method, the position uncertainty of TLEs for nanosatellites can be on the order of 1-10 km or more, even with batch least squares differential

correction processing [34]. This would yield relative navigation angular errors for crosslinks of tens of degrees for the CLICK minimum range of 25 km, which would lead to unacceptable beacon pointing losses and sensor field of view coverage even ignoring the additional error incurred by propagation over the time delay of waiting for TLE data to be uplinked from the ground to the spacecraft. Furthermore, the reliance on uplinked TLEs from the ground for space terminals is undesirable for the development of this technology into the future, where increased levels of autonomy are essential for the practical operation of satellite swarms and constellations. Due to these issues and the availability of GNSS receivers for use in nanosatellites, the use of TLEs for onboard navigation was discarded during CLICK mission design, and it is not considered further in this work. However, this level of positioning error can potentially be acceptable for significantly longer range crosslinks of thousands of km or for uplinks & downlinks. It should also be noted that the PorTeL optical ground station uses an extended Kalman filter to correct TLEs for use with orbit prediction for uplinks [22].

In practice, reference "truth" orbits are generated via numerical methods using complex force models. Therefore, this work considers analytical propation algorithms more generally to be in the purview of propagator algorithm optimization. Analytical methods may be used to reduce computational costs at the potential cost of accuracy if propagation algorithm performance optimization is deemed necessary given the available processor hardware resources. For reference, in the discussion of different Kalman filter implementations, the computational costs of some standard numerical integration algorithms will be discussed in Chapter 4. However, a more general discussion of algorithmic optimization approaches for particular hardware implementations, including the application of analytical methods, is beyond the scope of this work, and interested readers are referred to the literature, such as Vallado [33].

Perturbation Accelerations

The Cowell method uses two-body gravitational acceleration plus a perturbation acceleration. The perturbation acceleration is computed via the sum of additional forces

being considered beyond Keplerian two-body gravity. In Earth orbit, these generally can include aspherical Earth gravity terms, atmospheric drag, solar radiation pressure, third body perturbations, tides, earth radiation pressure, relativistic effects, and thrusting maneuvers. The general perturbing acceleration is:

$$\mathbf{a}_p = \mathbf{a}_{\text{aspherical}} + \mathbf{a}_{\text{drag}} + \sum_{i=1}^{N} \mathbf{a}_{3,i} + \mathbf{a}_{\text{SRP}} + \mathbf{a}_{\text{other}} \tag{3.3}$$

where $\mathbf{a}_{\text{aspherical}}$ is the acceleration due to central body effects beyond two-body gravity, $\mathbf{a}_{\text{drag}}$ is the acceleration due to atmospheric drag, $\mathbf{a}_{3,i}$ are the accelerations due to third body gravity, $\mathbf{a}_{\text{SRP}}$ is the acceleration due to solar radiation pressure, and $\mathbf{a}_{\text{other}}$ are any additional accelerations such as Earth radiation pressure. Each of these perturbing accelerations are discussed in the following sections.

Central Body Gravity Perturbations

The Kepler two-body acceleration simplifies the gravitational field by assuming the central body, which is the Earth in LEO, is a perfect sphere, which makes the central body gravitational potential (U) equivalent to that generated by a point of the same mass as the Earth. There are thus perturbing accelerations to this approximate form due to Earth's asphericity. The central body acceleration is given as the position gradient of the central body gravitational potential:

$$\mathbf{a}_{\text{central body}} = \mathbf{a}_{\text{two-body}} + \mathbf{a}_{\text{aspherical}} = -\frac{\partial U}{\partial \mathbf{r}} \tag{3.4}$$

The general gravitational potential is given as an infinite spherical harmonic series, where the coefficients are determined by the exact mass distribution of the central

body. The general central body potential used is [33]:

$$U = U_0 + U_1 + U_2 \tag{3.5a}$$

$$U_0 = -\frac{\mu}{r} \tag{3.5b}$$

$$U_1 = \frac{\mu}{r}\sum_{i=2}^{\infty} J_i \left(\frac{R_\oplus}{r}\right)^i P_{i,0}[\sin(\phi)] \tag{3.5c}$$

$$U_2 = -\frac{\mu}{r}\sum_{i=2}^{\infty}\sum_{j=1}^{i} \left(\frac{R_\oplus}{r}\right)^i P_{i,j}[\sin(\phi)]\left(C_{i,j}\cos(j\lambda) + S_{i,j}\sin(j\lambda)\right) \tag{3.5d}$$

where U_0 is the two-body spherical potential, U_1 is the perturbing potential due to zonal harmonics characterized by the coefficients J_i, U_2 is the perturbing potential due to sectoral and tesseral harmonics characterized by the coefficients $C_{i,j}$ & $S_{i,j}$, ϕ and λ are the satellite latitude & longitude, with $r = \|\mathbf{r}\|$, and $P_{i,j}[x]$ are the associated Legendre polynomials defined in general by the following expression [33]:

$$P_{i,j}[x] = \frac{(1-x^2)^{j/2}}{2^i i!}\frac{d^{i+j}}{dx^{i+j}}(x^2-1)^i \tag{3.6}$$

An order m by degree n ($m \times n$) gravity field model truncates the sum for U_1 and the primary sum for U_2 to the first m terms and the secondary sum for U_2 to the first $n \leq m$ terms. The simplest aspherical gravity model is the 2×0 model also referred to simply as J_2. This accounts for the primary oblateness of the Earth, which is by far the dominant effect, with J_2 being about 2 to 3 orders of magnitude larger than the next harmonics (see table 3.1). The corresponding perturbing acceleration given in the Earth-Centered-Earth-Fixed (ECEF) frame is [33]:

$$\mathbf{a}_{J2}^{ECEF} = -\frac{3}{2}\frac{\mu}{r^3}J_2\left(\frac{R_\oplus}{r}\right)^2 \begin{bmatrix} \left(1-5\left(\frac{z}{r}\right)^2\right)x \\ \left(1-5\left(\frac{z}{r}\right)^2\right)y \\ \left(3-5\left(\frac{z}{r}\right)^2\right)z \end{bmatrix} \tag{3.7}$$

where $\mathbf{r}^{ECEF} = [x, y, z]^T$ is the satellite position in the ECEF frame. Expressions for higher order gravity model acceleration components are documented in the literature

(see Vallado [33]).

Atmospheric Drag

Atmospheric drag is a perturbing force that is especially prominent in LEO. The satellite can be simply modeled via a flat plate approximation given by the following expression in the Earth-Centered-Inertial (ECI) frame [33]:

$$\mathbf{a}_{\text{drag}}^{\text{ECI}} = -\frac{1}{2}\left(\frac{C_D A_c}{m}\right)\rho \left\|\mathbf{v}_{\text{rel}}^{\text{ECI}}\right\| \mathbf{v}_{\text{rel}}^{\text{ECI}} \tag{3.8a}$$

$$\mathbf{v}_{\text{rel}}^{\text{ECI}} \approx \mathbf{v}^{\text{ECI}} - \omega_{\oplus}^{\text{ECI}} \times \mathbf{r}^{\text{ECI}} \tag{3.8b}$$

where C_D is the coefficient of drag (~ 2.2 [33]), A_c is the effective cross-sectional ram area, m is the satellite mass, ρ is the atmospheric density, $\mathbf{v}_{\text{rel}}$ is the velocity of the fluid relative to the effective flat plate cross-sectional area. The given approximation for the relative fluid velocity models atmosphere as simply co-rotating with the Earth, ignoring local effects like winds. Accurately determining the drag acceleration parameters is generally very challenging. The cross-sectional area requires knowledge of the satellite attitude. The coefficient of drag is a function of the satellite geometry and the atmospheric composition. The atmospheric density at high altitudes is a function of solar flux and geomagnetic activity, both of which are very difficult to predict. The solar flux activity at a wavelength of 10.7 cm, $F_{10.7}$, is monitored by the National Oceanic & Atmospheric Administration (NOAA), and 27-day forecasts are reported daily. The geomagnetic planetary index, K_p, and the corresponding daily planetary amplitude, A_p, are also reported in the daily 27-day forecast by NOAA. This data is used in time-varying atmospheric models like Jacchia-Roberts and NRLMSISE-2000, which are more accurate than table lookup models like the U.S. Standard Atmosphere 1976, although they run slower [33]. The COSPAR International Reference Atmosphere (CIRA) 1972 has moderate accuracy and efficiency, mixing table lookup with some free variables [33].

Third Body Perturbations

The gravity from other solar system bodies can also be taken into account. The dominant third body gravitational fields in Earth orbit are due to the Sun and the Moon. Let μ_3 be the gravitational parameter of the third body, and let $\mathbf{r}_3$ be the position of the third body relative to the Earth. Then each third body acceleration has the following form [33]:

$$\mathbf{a}_3 = \mu_3 \left(\frac{\mathbf{r}_3 - \mathbf{r}}{\|\mathbf{r}_3 - \mathbf{r}\|^3} - \frac{\mathbf{r}_3}{\|\mathbf{r}_3\|^3} \right) \tag{3.9}$$

Solar Radiation Pressure

The photons that make up solar irradiance carry momentum that can be transferred to objects they interact with. This effect is called solar radiation pressure and is modeled via a flat plate approximation as follows [33]:

$$\mathbf{a}_{\text{SRP}} = -\frac{pA_{\text{SRP}}}{m}(\hat{\mathbf{s}} \cdot \hat{\mathbf{n}}) \left[\left(\frac{2}{3} C_{R,d} + 2C_{R,s}(\hat{\mathbf{s}} \cdot \hat{\mathbf{n}}) \right) \hat{\mathbf{n}} + (1 - C_{R,s})\hat{\mathbf{s}} \right] \tag{3.10a}$$

$$\hat{\mathbf{s}} = \frac{\mathbf{r}_\odot - \mathbf{r}}{\|\mathbf{r}_\odot - \mathbf{r}\|} \tag{3.10b}$$

where $C_{R,d}$ is the coefficient of reflectivity for diffuse reflection, $C_{R,s}$ is the coefficient of reflectivity for specular reflection, $C_{R,a}$ is the coefficient of reflectivity for absorption, A_{SRP} is the effective sunlit surface area (m^2), p is the solar radiation pressure (Pa), $\mathbf{r}_\odot$ is the position of the sun relative to the Earth (km), and $\hat{\mathbf{n}}$ is the unit normal vector to the illuminated surface. The sunlit surface area requires knowledge of the satellite attitude. And the solar radiation pressure is generally time varying, with a nontrivial dependency on the Earth's shadow.

Other Perturbing Accelerations

Additional perturbation forces include Earth solid & ocean tides, radiation pressure from Earth's albedo and infrared emissions, relativistic effects, and manuevering thrust. Earth solid tides are deformations of the Earth's shape primarily due to the

gravitational attraction of the moon. Both Earth solid and ocean tides are accounted for via corrections to the aspheric gravitational potential coefficients. Earth radiation pressure is defined similarly to solar radiation pressure. Earth radiation pressure is of similar magnitude to ocean tides at LEO altitudes near 500 km [33]. Relativistic effects are corrections to Newtonian gravity using Einstein's theory of General Relativity. Relativistic effects are on the order of centimeters per orbit for a typical Earth satellite in a near-circular orbit [35]. As will be seen in Section 3.2, this should also be treated like tides and therefore only included in high accuracy "truth" models. As the CLICK spacecraft are not equipped with propulsion, the effects of maneuvering thrust are not considered further.

Numerical Comparison of Perturbing Accelerations in LEO

The purpose of this propagator study is for on-board operational use with nanosatellites in LEO, which necessitates a minimal force model for practical implementation. Hence, this section details a numerical comparison of perturbing accelerations in LEO to identify which perturbation sources should be included for further study and which can be safely ignored. The perturbing accelerations are computed using AGI's Systems Tool Kit (STK) via the High Precision Orbit Propagator (HPOP), which supports a wide variety of force models for comparison. The integrator used is a Runge-Kutta-Fehlberg 7(8) variable step method with a step size between 10^{-3} and 1 second, an error tolerance of 10^{-13}, and 7^{th} order Lagrange interpolation. The simulations were run for 2 hours from epoch, and the average magnitudes of the perturbing accelerations for initial altitudes between 400 and 600 km are shown in table 3.1. In all cases, the dominant perturbation is the Earth's J_2 acceleration by two orders of magnitude. Following this, the aspheric gravity terms up to degree 21 dominate other acceleration sources. It should be noted that the effects from non-conservative forces, drag and SRP, can have a significant effect distinct from the effects of the conservative forces over sufficient time intervals. Eventually, drag causes LEO satellites to lose sufficient energy to de-orbit. Furthermore, drag is actually taken advantage of by the CLICK mission for ranging using differential drag. At 500 km, solar radiation pressure

and drag are similar in average magnitude, with SRP acceleration being greater than drag acceleration at higher altitudes and smaller at lower altitudes. Third body perturbations are of similar magnitude to solar radiation pressure, with the Moon having about 3 times the effect of the Sun. Solid tides have a slightly greater effect than Lunar third body effects. Finally, ocean tides are the minimal acceleration at 400 and 500 km. Drag is the minimal acceleration at 600 km, although it should be noted that due to orbital decay, the effect due to drag compounds over time. Taking these results as guidance, the force model simplifications will be 1) eliminate tides, 2) eliminate third body perturbations, 3) eliminate SRP, 4 & 5) substitute simplified atmospheric models for NRLMSISE00, 6) eliminate drag, 7-9) truncate central body gravity to lower order square models, 10) use a J_2 model, and 11) use a two-body model. The next section will assess the position error incurred by these simplifications for various propagation intervals of interest for nanosatellite laser communications missions.

Table 3.1: Average magnitude (km/s^2) over 2 hours of various perturbing accelerations from epoch Jan 01 2019 00:00:00.000 UTC and initial states $(a, e, i, \Omega, \omega_p, M) = (6812.2-7013.2\text{km}, 0.005, 51.6^o, 220^o, 0^o, 0^o)$. h_p is the initial altitude at perigee. Drag and SRP area are both 0.1624 m^2, which is an upper estimate for a 3U nanosatellite with double deployed solar panels mounted on opposite corners of the central structure. $C_D = 2.2$ [33], $C_R = 2.0$ [33], Daily $F_{10.7cm} = 69$ [36], 81 Day Avg. $F_{10.7cm} = 69.47$ [36], Daily $K_p = 2$ [36].

Perturbation	$h_p = 400$ km	$h_p = 500$ km	$h_p = 600$ km
Two Body	8.60×10^{-3}	8.40×10^{-3}	8.10×10^{-3}
Central Body: J_2 (2×0)	1.29×10^{-5}	1.21×10^{-5}	1.13×10^{-5}
Central Body: 2×1 & 2×2	1.65×10^{-7}	1.54×10^{-7}	1.45×10^{-7}
Central Body: 3×0 to 3×3	2.61×10^{-7}	2.34×10^{-7}	2.10×10^{-7}
Central Body: 4×0 to 4×4	4.00×10^{-7}	3.62×10^{-7}	3.29×10^{-7}
Central Body: 5×0 to 5×5	2.09×10^{-7}	1.88×10^{-7}	1.70×10^{-7}
Central Body: 6×0 to 10×10	4.81×10^{-7}	4.22×10^{-7}	3.71×10^{-7}
Central Body: 11×0 to 21×21	7.16×10^{-8}	5.74×10^{-8}	4.61×10^{-8}
Central Body: 22×0 to 70×70	1.21×10^{-8}	7.75×10^{-9}	5.34×10^{-9}
Drag: CIRA 1972	9.52×10^{-10}	1.34×10^{-10}	6.11×10^{-11}
Drag: Jacchia-Roberts	9.66×10^{-10}	1.36×10^{-10}	6.13×10^{-11}
Drag: NRLMSISE-2000	8.06×10^{-10}	1.19×10^{-10}	6.03×10^{-11}
Drag: Std. Atm. 1976	4.16×10^{-9}	7.72×10^{-10}	1.84×10^{-10}
TBP: Moon	8.74×10^{-10}	8.92×10^{-10}	9.13×10^{-10}
TBP: Sun	3.03×10^{-10}	3.10×10^{-10}	3.16×10^{-10}
SRP	3.17×10^{-10}	3.25×10^{-10}	3.35×10^{-10}
Solid Tides	1.54×10^{-9}	1.44×10^{-9}	1.34×10^{-9}
Ocean Tides	1.26×10^{-10}	1.17×10^{-10}	1.09×10^{-10}

3.2 Comparison of Force Models

Although in principle all known perturbations could be included in the force model for propagation, in practice the computational overhead for force model evaluation dominates run times. This makes selection of a simplified force model with sufficient accuracy for the application at hand an essential part of designing any orbit propagation algorithm. Therefore, we will here examine the errors introduced by various simplifications of the force model for various propagation intervals in the time regime relevant for this study.

The reference "truth" orbit will be generated via STK's High Precision Orbit Propagator (HPOP) with a force model including 1) EGM-08 100×100 Earth gravity model with secular variations, permanent solid tides, and ocean tides; 2) Drag using

the NRLMSISE00 atmospheric density model; 3) solar radiation pressure; 4) luni-solar and planetary (Mercury, Venus, Mars, Jupiter, Saturn, Uranus, Neptune) third body perturbations. The numerical integration method is Runge-Kutta-Fehlberg 7(8) with a maximum step size of 10 seconds for intervals less then 24 hours and 60 seconds for the 24 hour interval, an error tolerance of 10^{-13}, and 7^{th}-order Lagrange interpolation. The epoch is January 1, 2019 00:00:00.000, and all intervals are propagated sequentially 30 times using the truth orbit to find the initial state for each interval.

The first simplification is to remove central body gravity tides and secular variations. Next, third body perturbations are removed, followed by solar radiation pressure. The simpler time-varying Harris-Priester and static 1976 Standard Atmosphere density models are tested before eliminating drag entirely. Finally, the central body gravity field is progressively truncated towards the two-body model by order of magnitude of the gravity field coefficients. The truncation roughly follows order of magnitude trends in the unnormalized EGM-08 zonal coefficients.

The comparison metric is the 99^{th} percentile of the L_2-norm of the position error over all 30 intervals propagated over 9 different low-Earth, near-circular orbits comprised of the combinations of the following initial state parameters: 400 km, 500 km, or 600 km altitudes at perigee; 0.005 eccentricity; 35°, 51.6° ISS, or sun-synchronous inclination (82° – 83° depending on the altitude); −120° RAAN, 0° argument of perigee, and 0° mean anomaly. Figure 3-2 shows the results for this comparison. The relevant propagation intervals selected cover the likely regimes for application to satellite lasercom links. For downlinks and crosslinks, if the GPS information is recorded and processed in real time, a one minute interval is a conservative upper bound for propagation of the host orbit. For crosslinks with a direct RF exchange of GPS information, the messaging delay would be included in the 1 minute interval: a 700 bit message containing an epoch and initial state in double-precision floating point along with any necessary headers has a transfer time less than 1 second given a data rate on the order of 1 kbps. Similarly, if a crosslink utilized a satellite communications network like Globalstar, the messaging delay could be also included in the 1 minute interval: for the same message with a 72 bps worst-case data rate; the

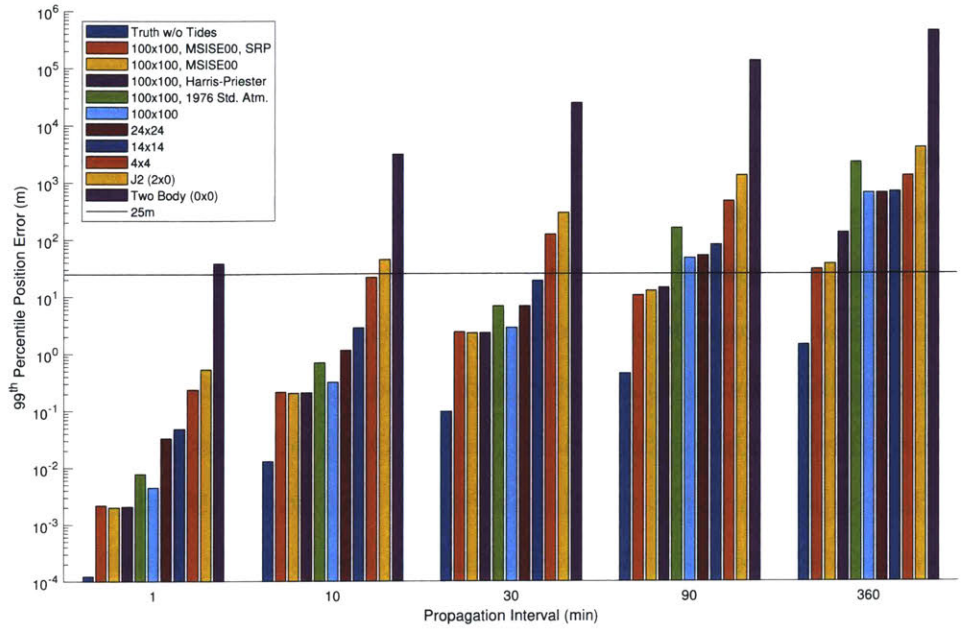

Figure 3-2: Propagation Error Statistics for Force Model Simplifications

system would have a transfer time less than ten seconds [32]. If the GPS measurement process is duty cycled to save power or if the desired receiver performance is intermittent (e.g. CanX-2 [37] & Aalto-1 [38]), the necessary propagation interval for both the crosslink and downlink cases could extend to the order of 10 minutes if we still assume satellite-to-satellite communications in the crosslink case. The propagation interval could be further increased for crosslinks if no satellite-to-satellite communications capability is implemented and the system relies on ground stations. For a network of ground stations with global coverage (e.g. KSAT [39]), one to a handful of relays could be consistently achieved per orbit [39], which is represented in this analysis by propagation times of 30 & 90 minutes. Finally, for a single ground station in the Continental United States, STK access geometry analysis yields an overpass waiting time of approximately 360 minutes averaged over the 9 orbits and over the 3 ground stations in Table 3.4 (for a simulation period of 180 days using a J_2 force model). This time is used as the estimate for the co-planar crosslink relay using a single ground station.

These estimates are here used simply to downselect to a few force models for further, more detailed analysis that can directly simulate initial acquisition angular error from navigation. For this purpose, a simple order of magnitude position error requirement is sufficient. With regard to the beacon $1/e^2$ divergence angle of about 22.1 mrad, this is taken to be 1 mrad ($\sim$ 5% of θ_{1/e^2}) to have sufficient margin remaining for measurement error. This angle roughly corresponds to 25 m for the 25 km range crosslink, which is used because it is the worst case geometry and therefore guarantees that the selected force models will also be sufficient for longer range crosslinks and downlinks. The solid black line illustrates the 25 m position error in Figure 3-2.

For downlink and crosslink host orbit propagation, we are interested in the 1 and 10 min intervals, and J_2 is judged as sufficient. For crosslink target orbit propagation in the 1 and 10 min interval range, 4×4 central body gravity is sufficient. For the crosslink target orbit propagation in the 30 min range, more terms in the central body field are needed, such as a 14×14 model. Once at least one full orbit ($\sim$ 90 min) is propagated, a high-fidelity central body model is necessary, and drag effects become noticeable. It should be noted that using the 1976 Standard Atmosphere static density model is worse than simply ignoring drag entirely in all cases. Using a simplified time-varying density model like Harris-Priester is feasible for the 90 min interval. However, it is undesirable to incur the additional operational complexity of needing space weather data on-board as well as estimates of the Target spacecraft's attitude for computing its ram area. For simplicity therefore, the $\sim$ 50 m position error for the 100×100 central body gravity model without drag is judged as sufficient for the 90 minute target interval case. For multi-orbit intervals, high-fidelity modeling of the atmospheric density is necessary, and additional contributions from solar radiation pressure and third-body effects should be taken into account. A force model of this level of fidelity would be difficult to implement for on-board software in practice due to its high computational cost and the need for accurate space weather and target attitude data. Therefore, propagation over an interval of one or more orbits during a ground relay would be done on the ground while waiting to upload to the

spacecraft. However, this work is mainly interested in relative navigation algorithms for use onboard the spacecraft that enable greater levels of autonomy; therefore, the 360 minute target interval case will not be considered further.

In summary, to achieve a position propagation accuracy of $\sim$ 25 m for crosslinks, the models chosen for further analysis are J_2 for Δt = 1 minute, 4 $\times$ 4 for Δt = 10 minutes, 14 $\times$ 14 for Δt = 30 minutes, and 100 $\times$ 100 for Δt = 90 minutes. For downlink, the 1 & 10 minute interval cases using the same respective models will be analyzed.

3.3 Propagation Error for Crosslinks

Tables 3.2 and 3.3 summarize the simulation results of model-induced errors for crosslinks at the CLICK boundary ranges of 25 km and 580 km, respectively. The absolute position errors for the Host and Target satellites are given, along with the relative range and angle errors. The angle errors are the key results for pointing analysis. The truth model is as described in Section 3.2, and the Host & Target models under evaluation along with the propagation intervals (Δt_H & Δt_H) are listed. The initial altitude of the Target spacecraft is set to 1 km below that of the Host to include an offset due to differential drag ranging. The simulation duration is set to include 30 Target propagation intervals, with the number of Host propagation intervals being enough to fill the simulation period. This means, for example, that for the 10 minute target interval simulations, the simulation duration is 300 minutes, so there are 300 host intervals for the 1 minute host interval case and only 30 host intervals for the 10 minute host interval case. This is why the host position error statistic changes between cases even if the host interval is the same.

As noted in Section 3.2, the allocation for navigation error (99^{th} percentile) is on the order of 1 mrad angle error (approx. 25 m position error). The results agree with the predicted performance: all cases have a 99^{th} percentile model-induced error of less than 0.6 mrad. The case that is representative of CLICK B/C operations is the 1 minute host and 10 minute target interval case (row 2 in both tables). With

respect to the reference total error case discussed in Chapter 2 that also includes GPS measurement error, the model error therefore accounts for 588/1367 = 43% of the total error in the 25 km case and 36.3/76.58 = 47.4% of the total error in the 580 km case. Moreover, all configurations other than the reference configuration have reduced angle error, which indicates that these configurations may also be feasible alternatives. This will be discussed further when GPS measurement error is added in Section 3.8. In summary, the results show that using only an appropriate central

Table 3.2: Error magnitudes (99^{th} percentile) for model-induced propagation error for CLICK short range (25 km) LEO crosslink for various propagation configurations.

Δt_H (min)	Δt_T (min)	Host Model	Target Model	Host Pos. Err. (m)	Target Pos. Err. (m)	Range Err. (m)	Angle Err. (μrad)
1	1	J_2	J_2	0.580	0.578	0.252	22.32
1	**10**	**J_2**	**4×4**	**0.642**	**22.08**	**9.142**	**588.0**
10	10	4×4	4×4	23.24	23.32	7.828	529.6
10	30	4×4	14×14	20.74	19.09	13.31	479.3
10	90	4×4	100×100	19.86	47.40	13.22	324.9

Table 3.3: Error magnitudes (99^{th} percentile) for model-induced propagation error for CLICK long range (580 km) LEO crosslink for various propagation configurations.

Δt_H (min)	Δt_T (min)	Host Model	Target Model	Host Pos. Err. (m)	Target Pos. Err. (m)	Range Err. (m)	Angle Err. (μrad)
1	1	J_2	J_2	0.567	0.520	0.253	0.847
1	**10**	**J_2**	**4×4**	**0.605**	**21.76**	**8.353**	**36.34**
10	10	4×4	4×4	23.24	23.05	8.026	32.94
10	30	4×4	14×14	20.74	19.97	13.40	37.02
10	90	4×4	100×100	19.86	47.37	13.27	31.20

body gravity model, model-induced propagation error can be maintained less than 50 m for intervals up to 90 minutes and less than 25 m for intervals up to 30 minutes. This corresponds to 99^{th} percentile angular errors of less than 600 μrad at 25 km and less then 40 μrad at 580 km. For the baseline case, the model error accounts for 43% of the total error at 25 km case and 47.4% of the total error at 580 km. Moreover, all configurations other than the reference configuration have reduced angle error, which

means that they are all potentially feasible options for crosslinks similar to CLICK. The next section will explore the Earth rotation model used for Target position prediction in downlinks as background for the analysis of the model-induced error for downlinks.

3.4 Earth Rotation Models

An Earth Centered Inertial (ECI) frame is a psuedoinertial frame with respect to the stars (taken to be fixed). An Earth Centered Earth Fixed (ECEF) frame is a non-inertial frame that rotates with the Earth. The International Astronomical Union (IAU) defines commonly used versions of these frames and how to transform between them. In the IAU nomenclature, the ECI frame is the Geocentric Celestial Reference Frame (GCRF), and the ECEF frame is the International Terrestrial Reference Frame (ITRF). The current definition follows the IAU-2000/2006 resolutions, which re-defined the transformation in terms of the Celestial Intermediate Origin (CIO), with three new parameters (X, Y, s) defining precession and nutation. The previous definition was IAU-1976/FK5 (J2000.0), which uses the IAU 1976 precession theory and the IAU 1980 nutation theory [33]. It should be noted for reference that the U.S. WGS-84 ECEF frame used by GPS agrees with the ITRF to the cm level, which means that they are considered to be interchangeable in this work [33]. In general, the transformation of a position, velocity, or acceleration vector are defined as follows [33]:

$$\mathbf{r}^{\text{GCRF}} = P(t)N(t)R(t)\mathbf{r}^{\text{TIRS}} \tag{3.11a}$$

$$\mathbf{v}^{\text{GCRF}} = P(t)N(t)R(t)(\mathbf{v}^{\text{TIRS}} + \omega_{\oplus} \times \mathbf{r}^{\text{TIRS}}) \tag{3.11b}$$

$$\mathbf{a}^{\text{GCRF}} = P(t)N(t)R(t)(\mathbf{a}^{\text{TIRS}} + 2\omega_{\oplus} \times \mathbf{v}^{\text{TIRS}} + \omega_{\oplus} \times (\omega_{\oplus} \times \mathbf{r}^{\text{TIRS}})) \tag{3.11c}$$

$$\mathbf{r}^{\text{TIRS}} = W(t)\mathbf{r}^{\text{ITRF}},\ \mathbf{v}^{\text{TIRS}} = W(t)\mathbf{v}^{\text{ITRF}},\ \mathbf{a}^{\text{TIRS}} = W(t)\mathbf{a}^{\text{ITRF}} \tag{3.11d}$$

$$\omega_{\oplus} = [0,\ 0,\ 7.292115146706979 \times 10^{-5}(\text{rad/s})(1 - \text{LOD}/86400)]^T \tag{3.11e}$$

where P accounts for precession, N accounts for nutation, R accounts for sidereal rotation, and W accounts for polar-motion, which relates the ITRF to the Terrestrial Intermediate Reference System (TIRS). Length of Day (LOD) is the difference between the observed mean solar day and 86,400 SI seconds. Additional information on time systems can be found in Appendix A.7.

The sidereal rotation about the Earth's axis R is defined using the Earth rotation angle θ_{ERA} as [33]:

$$R = \begin{bmatrix} \cos(\theta_{\text{ERA}}) & -\sin(\theta_{\text{ERA}}) & 0 \\ \sin(\theta_{\text{ERA}}) & \cos(\theta_{\text{ERA}}) & 0 \\ 0 & 0 & 1 \end{bmatrix} \tag{3.12}$$

The precession and nutation of the Earth's axis PN is defined as [33]:

$$PN = \begin{bmatrix} 1 - a\bar{X}^2 & -a\bar{X}\bar{Y} & \bar{X}\bar{Y} \\ -a\bar{X}\bar{Y} & 1 - a\bar{Y}^2 & \bar{Y} \\ -\bar{X} & -\bar{Y} & 1 - a(\bar{X}^2 + \bar{Y}^2) \end{bmatrix} \begin{bmatrix} \cos(s) & \sin(s) & 0 \\ -\sin(s) & \cos(s) & 0 \\ 0 & 0 & 1 \end{bmatrix} \tag{3.13}$$

Lastly, the ITRF to TIRS transformation W is defined as [33]:

$$W = \begin{bmatrix} \cos(s') & -\sin(s') & 0 \\ \sin(s') & \cos(s') & 0 \\ 0 & 0 & 1 \end{bmatrix} \begin{bmatrix} \cos(x_p) & 0 & -\sin(x_p) \\ 0 & 1 & 0 \\ \sin(x_p) & 0 & \cos(x_p) \end{bmatrix} \begin{bmatrix} 1 & 0 & 0 \\ 0 & \cos(y_p) & \sin(y_p) \\ 0 & -\sin(y_p) & \cos(y_p) \end{bmatrix} \tag{3.14}$$

where (x_p, y_p) are polar motion displacements along the 0^o & 90^oW longitude meridians, respectively. These are published daily by the International Earth Rotation Service (IERS) as part of the Earth Orientation Parameter (EOP) sets, which also include CIO offsets (dX, dY) and LOD [33, 40]. The daily published data can also be found aggregated with timing offsets ΔAT & ΔUT1 at [41].

The $\bar{X}$ series is defined as [33]:

$$X = \sum_{j=0}^{4} \left(C_{X,j} + \sum_{i=1}^{N_{X,j}} A_{X,j}\sin(\alpha_{X,i}) + B_{X,j}\cos(\alpha_{X,i}) \right) \mathrm{T}_{\mathrm{TT}}^{j} \tag{3.15a}$$

$$\text{with } N_{X,j} \in \{1306, 253, 36, 4, 1\} \tag{3.15b}$$

$$\bar{X} = X + dX \tag{3.15c}$$

The $\bar{Y}$ series is defined as [33]:

$$Y = \sum_{j=0}^{4} \left(C_{Y,j} + \sum_{i=1}^{N_{Y,j}} A_{Y,j}\sin(\alpha_{Y,i}) + B_{Y,j}\cos(\alpha_{Y,i}) \right) \mathrm{T}_{\mathrm{TT}}^{j} \tag{3.16a}$$

$$\text{with } N_{Y,j} \in \{962, 277, 30, 5, 1\} \tag{3.16b}$$

$$\bar{Y} = Y + dY \tag{3.16c}$$

$$\tag{3.16d}$$

And the remaining parameters, θ_{ERA} and s' are defined as [33]:

$$s = -\frac{XY}{2} + \sum_{j=0}^{4} \left(C_{s,j} + \sum_{i=1}^{N_{s,j}} A_{s,j}\sin(\alpha_{s,i}) + B_{s,j}\cos(\alpha_{s,i}) \right) \mathrm{T}_{\mathrm{TT}}^{j} \tag{3.17a}$$

$$\text{with } N_{s,j} \in \{33, 3, 25, 4, 1\} \tag{3.17b}$$

$$a \cong \frac{1}{2} + \frac{1}{8}(\bar{X}^2 + \bar{Y}^2) \tag{3.17c}$$

$$\theta_{\mathrm{ERA}} = 2\pi(0.779057273264 + 1.00273781191135448(\mathrm{JD}_{\mathrm{UT1}} - 2451545.0)) \tag{3.17d}$$

$$s' = -0.000047\text{"}\mathrm{T}_{\mathrm{TT}} \tag{3.17e}$$

where $\alpha_{X,i}$, $\alpha_{Y,i}$, and $\alpha_{s,i}$ are unique linear combinations of the Delaunay arguments, each of which is expressed as a fourth order polynomial in T_{TT} (see [33] for exact expressions). The coefficients for the ($\alpha_{X,i}$, $\alpha_{Y,i}$, $\alpha_{s,i}$) linear combinations and for the (X, Y, s) series are tabulated and can be found online at [42]. θ_{ERA} is the Earth Rotation Angle and s' is the Terrestrial Intermediate Origin (TIO) locator, which accounts for polar wobble.

Numerical Comparison of ECEF-ECI Transformations

The IAU-2000/2006 transformation has three versions (A, B, and C) and from highest to lowest computational cost, they are C, A, B [33]. The baseline for comparison is the C version. The IAU-00/06 A and B versions in addition to the IAU-76/FK5 method are included in the comparison. The IAU-2000/2006 transformation algorithm can also be simplified by eliminating Earth Orientation Parameters (EOPs) & the s parameter and truncating to only a few terms in the X & Y series. Reducing the number of EOP also reduces the amount of uplink telemetry data required to run the algorithm on-board. The simplified methods chosen for analysis here are based on a study done by Bradley and are [40]:

- Set $s, dX, dY, x_p, y_p, \Delta\text{UT1}$ to zero, truncate X, Y series to 4 terms.
- Set s, dX, dY, x_p, y_p to zero, include ΔUT1, truncate X, Y series to 4 terms.
- Set s, dX, dY to zero, include $x_p, y_p, \Delta\text{UT1}$, truncate X, Y series to 15 terms.

The X, Y series are ordered from the largest term to the smallest term, so a 4-term truncation means setting $N_0 = 4$ & $N_1 = N_2 = N_3 = N_4 = 0$. Note that the series should be added in reverse order starting with the smallest terms to mitigate numerical rounding errors. The comparison was performed using STK for GCRF ground position reference data. This was converted to ITRF data using the IAU-2000/2006 C method for a common reference before being converted back into GCRF data to compare the various reduced cost methods relative to IAU-00/06 C. The software was implemented in MATLAB via an adaptation of open-source software published by Vallado [43]. The results are summarized in Table 3.4. The simplified models are listed in order of increasing accuracy. For the most part, this corresponds to increasing computational cost; however, the IAU-76/FK5 model actually outperformed the IAU-00/06 A model, though the difference is on the order of millimeters, which is not significant for our purposes. More significant performance degradation came when truncating the X & Y series to only a few terms and eliminating the s parameter & EOP parameters. However, even with the simplest 4-term, no EOP model, position

Table 3.4: 99^{th} percentile position error magnitude (m) for ECEF to ECI transformation implementations relative to full-accuracy IAU-2000/2006 method. Simulation over 7 days with 10 min sampling time from epoch Jan 01 2019 00:00:00.000 UTC. Reference geodetic coordinates (Latitude, Longitude): Boston (42.360636°, − 71.093418°), Boulder (40.006891°, − 105.264983°), Los Angeles (34.068851°, − 118.444692°).

ITRF to GCRF Method	3D RMS Position Error (m), Boston	3D RMS Position Error (m), Boulder	3D RMS Position Error (m), Los Angeles
4-term X,Y Only	14.110	14.561	15.632
4-term X,Y & ΔUT1	9.800	9.053	8.105
15-term X,Y & x_p, y_p, ΔUT1	1.184	1.179	1.175
IAU-00/06 B & All EOP	0.0227	0.0226	0.0223
IAU-00/06 A & All EOP	0.0181	0.0181	0.0180
IAU-76/FK5 & All EOP	0.0039	0.0038	0.0038

error remained less than 16 m, which corresponds to about 9-16 μrad of angular error for the median downlink ranges of about 1000-1700 km from the analysis in Table 2.5. The baseline model will be IAU-00/06 B with all EOPs. For further reference, a detailed study of ECEF-ECI transformation simplification approaches can be found in Bradley [40].

ECI-ECEF Acceleration Transforms for Orbit Propagation

Aspherical central body gravity accelerations are typically computed in the ECEF frame and converted to ECI for propagation. In this work, the high-accuracy Earth rotation model in STK's HPOP is used; however, in practice it is possible to optimize performance by using a simplified Earth rotation model. Bradley gives an analysis of the effects of truncating Earth rotation models for orbit propagation. For a 400 km LEO orbit, the simplest truncated model, the 4-term X,Y series with no EOPs has 0.2 mm position error for $\Delta t = 1$ minute, 4.6 cm error for $\Delta t = 15$ minutes, and 2.9 m for $\Delta t = 6$ hours [40]. Comparing against the results in Section 3.3, this effect is not significant ($\sim 0.03\%$) relative to force model errors for 1 minute propagation intervals, so truncation may be effectively used in these cases to reduce computational costs. Taking the 15 minute error as relevant to the 10 & 30 minute propagation, the effect

is also insignificant ($\sim 0.2\%$) relative to force model errors. Taking the 6 hour error as relevant for 90 minute propagation, the effect will be $\sim 6\%$ of the force model position errors, with additional angular error of $\sim 30\%$ over 25 km. In summary, for intervals on the order of 15 minutes or less, a truncated ECI-ECEF model is not considered to impact satellite orbit prediction significantly for relative navigation purposes and is a feasible option for reducing computational costs. It should also be noted that an alternative approach to performance optimization is to avoid transformation of the central body acceleration by propagating the orbit state in the ECEF frame. Bradley gives an analysis of the errors for this configuration [40].

3.5 Propagation Error for Downlinks

Table 3.5 summarizes the simulation results of model-induced errors for downlinks to ground station locations located on the east coast, midwest, and west coast of the Continental U.S. (CONUS) at higher, mid, and lower latitudes. The access data is aggregated over all three locations for statistical analysis. The STK simulation has the same 9 orbit types, epoch, and truth model as the previous crosslink (Sec. 3.3) and force model analysis simulations (Sec. 3.2). The propagation intervals are limited to 1 and 10 minutes (see Sec. Sec. 3.2), as there is no ephemeris transfer necessary during the link: the ground station is assumed fixed with its ECEF coordinates stored on-board the spacecraft. Updates to the stored coordinates are possible during periodic TT&C contacts with the mission operations center. The minimum elevation angle for access is set to 0°. The three truncated ECI-ECEF transforms (see Sec. 3.4) are included, in addition to IAU-00/06B (all the IAU models have near-zero error contribution, so it is redundant to include all of them), and lastly a case without any ECI-ECEF transform error as a control comparison.

What is immediately clear in Table 3.5 is that the IAU-00/06 B transform with all EOP has essentially negligible error contribution. Moreover, for short ($\approx$ 1 min) intervals, even a simple J_2 model has near-negligible (sub-arcsec) angular error contribution for terminals similar to CLICK. For longer intervals, the propagation error

becomes more noticeable but is still in the range tens of microradians. Lastly, the 15-term X,Y & x_p, y_p, ΔUT1 ECI-ECEF transformation error is on the order of short interval J_2 model error. Hence, it could potentially be used as a sufficiently accurate, lower computational cost alternative to the IAU-00/06 B transform (15 terms as opposed to 77). The baseline case with a 1 minute host interval and IAU-00/06 B (row 4) has an error of 0.338 μrad. With respect to the reference total error in the baseline case, the model error accounts for 0.338/17.29 = 2.0% of the total error (see Table 3.13). As would be expected, as the Earth rotation model is simplified, the model error fraction of the total error increases. For example, for the 1 minute host interval and 4-term series without EOPs, the model error accounts for 28.77/33.90 = 85% of the total error. All cases have a 99$^{\text{th}}$ percentile model-induced error of less than 32 μrad, which is on the order of the point-ahead error (50.36 μrad). This indicates the feasibility of using configurations other than the baseline, which will be discussed further when GPS measurement error is added in Section 3.8. The following sections will discuss the GPS measurement process and the associated errors.

Table 3.5: Error magnitudes (99$^{\text{th}}$ percentile) for model-induced error for LEO downlink to CONUS for various propagation & ECI-ECEF transform configurations. Reference geodetic coordinates (Latitude, Longitude): Boston (42.360636°, −71.093418°), Boulder (40.006891°, − 105.264983°), Los Angeles (34.068851°, − 118.444692°).

Δt_H (min)	Host Model	ECI-ECEF Transform	Host Pos. Err. (m)	Target Pos. Err. (m)	Range Err. (m)	Angle Err. (μrad)
1	J_2	4-term X,Y Only	0.478	18.04	17.80	28.77
1	J_2	4-term X,Y & ΔUT1	0.478	7.963	7.812	12.39
1	J_2	15-term X,Y & x_p, y_p, ΔUT1	0.478	0.866	0.789	1.198
1	**J_2**	**IAU-00/06 B & All EOP**	**0.478**	**0.015**	**0.015**	**0.338**
1	J_2	None	0.478	0.000	0.010	0.334
10	4×4	4-term X,Y Only	24.56	18.14	18.02	31.11
10	4×4	4-term X,Y & ΔUT1	24.56	7.959	7.871	19.97
10	4×4	15-term X,Y & x_p, y_p, ΔUT1	24.56	0.935	7.991	15.55
10	4×4	IAU-00/06 B & All EOP	24.56	0.015	7.565	15.78
10	4×4	None	24.56	0.000	7.576	15.78

3.6 GPS Measurements

The Global Positioning System (GPS) was developed under the NAVSTAR satellite program and is operated by the U.S. Department of Defense (DoD) [44]. As of January 2020, the GPS constellation consists of 31 operational GPS satellites [45] located in near-circular Medium Earth Orbits (MEOs) with radii of 26,560 km and orbital periods of approximately 12 hours [44]. Each GPS satellite continuously broadcasts the GPS message, including data needed to compute user position, velocity, and clock errors. The transmission frequencies are designated as L1 (1575.42 MHz) and L2 (1227.6 MHz) [44]. Additional technical implementation details are published by the DoD [46]. This section will describe a typical approach used to compute the user position and velocity from the GPS measurement observables. The corresponding position and velocity uncertainty will also be derived as a function of the so-called dilution of precision (DOP) and the noise associated with the observables.

3.6.1 User Position

The position measurement observables are the psuedoranges (ρ_α) to each GPS satellite in view [47]:

$$\rho_\alpha = d_\alpha + c\delta t_u + w_\rho \tag{3.18a}$$

$$d_\alpha = c\Delta t = \|\mathbf{r}_\alpha - \mathbf{r}_u\| = \sqrt{(x_\alpha - x_u)^2 + (y_\alpha - y_u)^2 + (z_\alpha - z_u)^2} \tag{3.18b}$$

$$\alpha \in \{1, ..., N_{\text{GPS}}\} \tag{3.18c}$$

where ρ_α is the measured psuedorange from the user to GPS satellite α, d_α is the corresponding true range, $\mathbf{r}_\alpha$ are the GPS satellite positions, $\mathbf{r}_u$ is the user position, $\Delta t = t_u - t_s$ is the difference in the true receive time and transmission time, δt_u is the user clock error, and w_ρ is the measurement error, which has variance σ^2_{URE} (URE: User Range Error). The transmission time and the GPS satellite position data are contained in the GPS message. Note that the GPS satellite position data is given in the WGS84 ECEF reference frame, so the position estimate will also be with respect

to this frame unless a conversion is also computed. As noted in Section 3.4, the ITRF corresponds to the WGS84 frame to cm-level accuracy; so for the purposes of this work, these two frames are considered to be interchangeable.

The simplest position estimation method directly solves for the the unknown variables $\mathbf{x}^T = [x_u, y_u, z_u, c\delta t_u]$ at a particular time using a set of measurements from at least 4 GPS satellites in view ($N_{GPS} \geq 4$). This is a set of nonlinear equations that can be linearized and solved via Gauss-Newton least squares iteration. It should be noted that although more complex position estimation algorithms using filtering can be used, the same linearization of the measurement equation (H The iteration step is defined as [48]:

$$\mathbf{x}_{k+1} = \mathbf{x}_k - (H_k^T H_k)^{-1} H_k^T \Delta\mathbf{y}_k, \;\; k = 0, 1, 2, ..., n \tag{3.19}$$

where n is the final iteration count dictated by a stopping tolerance criterion $\|\Delta\mathbf{x}_k\| = \|\mathbf{x}_{k+1} - \mathbf{x}_k\| < \epsilon$ and/or iteration count limit. The measurement residual $\Delta\mathbf{y}_k$ and the measurement Jacobian H_k are [48]:

$$\Delta\mathbf{y}_k = [\hat{\rho}_1(\mathbf{x}_k) - \rho_1, ..., \hat{\rho}_\alpha(\mathbf{x}_k) - \rho_\alpha, ..., \hat{\rho}_{N_{GPS}}(\mathbf{x}_k) - \rho_{N_{GPS}}]^T \tag{3.20a}$$

$$H_k = [\mathbf{h}_1(\mathbf{x}_k), ..., \mathbf{h}_\alpha(\mathbf{x}_k), ..., \mathbf{h}_{N_{GPS}}(\mathbf{x}_k)]^T \tag{3.20b}$$

$$\mathbf{h}_\alpha^T(\mathbf{x}_k) = \frac{\partial\hat{\rho}_\alpha}{\partial\mathbf{x}}(\mathbf{x}_k) = [-\hat{\mathbf{p}}_\alpha^T(\mathbf{x}_k), 1] \tag{3.20c}$$

$$\hat{\mathbf{p}}_\alpha(\mathbf{x}_k) = (\mathbf{r}_\alpha - \hat{\mathbf{r}}_u(\mathbf{x}_k))/\hat{d}_\alpha(\mathbf{x}_k) \tag{3.20d}$$

$$= [x_\alpha - x_{u,k}, y_\alpha - y_{u,k}, z_\alpha - z_{u,k}]^T/\hat{d}_\alpha(\mathbf{x}_k) \tag{3.20e}$$

$$\hat{\rho}_\alpha = \hat{d}_\alpha(\mathbf{x}_k) + c\delta t_{u,k} \tag{3.20f}$$

$$\hat{d}_\alpha(\mathbf{x}_k) = \sqrt{(x_\alpha - x_{u,k})^2 + (y_\alpha - y_{u,k})^2 + (z_\alpha - z_{u,k})^2} \tag{3.20g}$$

where $\hat{\mathbf{p}}_\alpha$ are the estimated direction vectors to the GPS satellites in view. We can solve for the error covariance of the position estimate $\mathrm{E}[\Delta\mathbf{x}\Delta\mathbf{x}^T]$ as follows [44]:

$$\mathrm{E}[\Delta\mathbf{x}\Delta\mathbf{x}^T] = \mathrm{E}[(H^TH)^{-1}H^T\Delta\mathbf{y}\Delta\mathbf{y}^TH(H^TH)^{-1}] \tag{3.21a}$$

$$= (H^TH)^{-1}H^T\mathrm{E}[\Delta\mathbf{y}\Delta\mathbf{y}^T]H(H^TH)^{-1} \tag{3.21b}$$

The pseudorange measurement residual covariance $\mathrm{E}[\Delta\mathbf{y}\Delta\mathbf{y}^T]$ is assumed uncorrelated (e.g. diagonal) [44], and the algorithm error is assumed negligible relative to the measurement error w_ρ:

$$\mathrm{E}[\Delta\mathbf{y}\Delta\mathbf{y}^T] = \mathrm{E}[w_\rho w_\rho]I_{N_{GPS}\times N_{GPS}} = \sigma^2_{URE}I_{N_{GPS}\times N_{GPS}} \tag{3.22}$$

Substituting Equation 3.22 into Equation 3.21b yields:

$$\mathrm{E}[\Delta\mathbf{x}\Delta\mathbf{x}^T] = \sigma^2_{URE}G \tag{3.23a}$$

$$G \equiv (H^TH)^{-1} \tag{3.23b}$$

where G is the dilution of precision (DOP) matrix, which yields the various dimensionless DOP scalars [44]:

$$\text{Geometric DOP: GDOP} = \sqrt{\mathrm{tr}(G)} = \sqrt{G_{11}+G_{22}+G_{33}+G_{44}} \tag{3.24a}$$

$$\text{Position DOP: PDOP} = \sqrt{G_{11}+G_{22}+G_{33}} \tag{3.24b}$$

$$\text{Horizontal DOP: HDOP} = \sqrt{G_{11}+G_{22}} \tag{3.24c}$$

$$\text{Vertical DOP: VDOP} = \sqrt{G_{33}} \tag{3.24d}$$

$$\text{Time DOP: TDOP} = \sqrt{G_{44}} \tag{3.24e}$$

Therefore, given the URE variance and the dilution of precision scalars, the user position error standard deviations can be easily estimated using the following formulae:

$$\sigma_{x_u} = \sqrt{G_{11}}\ \sigma_{\text{URE}} \tag{3.25a}$$

$$\sigma_{y_u} = \sqrt{G_{22}}\ \sigma_{\text{URE}} \tag{3.25b}$$

$$\sigma_{z_u} = \sqrt{G_{33}}\ \sigma_{\text{URE}} \tag{3.25c}$$

$$\sigma_{r_u} = \sqrt{\sigma_{x_u}^2 + \sigma_{y_u}^2 + \sigma_{z_u}^2} = \text{PDOP}\ \sigma_{\text{URE}} \tag{3.25d}$$

It should be noted that the values in G and the corresponding position component standard deviations are dependent on the reference frame used. The RMS position standard deviation (σ_{r_u}) is invariant. A standard co-moving reference frame for terrestrial receivers is North-East-Down (NED), hence the reason why the first two components of the main diagonal of G are termed horizontal, with the third being termed vertical. A corresponding co-moving reference frame for space-based receivers is Vehicle Vertical Local Horizontal (VVLH), which is defined by the orbit's in-track, cross-track, and nadir directions.

3.6.2 User Velocity

User velocity can be measured in two ways: one, the user position data can be numerically differentiated; or two, the Doppler-shifts (Δf_α) induced by the relative motion between the receiver and the GPS satellites in view can be measured. The modern receivers that will be referenced in later sections can actually be set to use either method depending on the latency properties desired: the Doppler derived velocity has lower latency than the position data derived velocity in these receivers [49]. Regardless of the method used, the same method for estimating velocity uncertainty using DOP and URRE can be applied for analysis, with the URRE potentially being different depending on the method selected for computation. First, the relationship between Doppler-shift and pseudorange rate will be given. In practice, the psuedorange rates could either be found via via Doppler measurements or numerical differentiation.

Then the uncertainty analysis will utilize psuedorange rate as the observable to show how the velocity uncertainty is related to the URRE via the same DOP values used for position error analysis.

The Doppler-shift is defined as follows [50]:

$$\Delta f_\alpha = f_{R,\alpha} - f_{T,\alpha} = -\frac{f_{T,\alpha}}{c}\dot{d}_\alpha \tag{3.26a}$$

$$f_{R,\alpha} = f_\alpha(1 + \delta\dot{t}_u) \tag{3.26b}$$

$$f_{T,\alpha} = f_0 + \delta f_{T,\alpha} \tag{3.26c}$$

$$\dot{d}_\alpha = (\mathbf{v}_\alpha - \mathbf{v}_u) \cdot \mathbf{p}_\alpha \tag{3.26d}$$

where $\dot{d}_\alpha$ are the true range rates, $\mathbf{v}_\alpha$ are the velocities of the GPS satellites, $\mathbf{v}_u$ is the user velocity, $f_{R,\alpha}$ is the true received frequency, f_α is the measured received frequency, $f_{T,\alpha}$ is the corrected transmit frequency, f_0 is the nominal transmit frequency (e.g. L1).

The psuedorange rate is defined by differentiation of Equation 3.18a:

$$\dot{\rho}_\alpha = \dot{d}_\alpha + c\delta\dot{t}_u + w_{\dot{\rho}} \tag{3.27}$$

where $\delta\dot{t}_u$ is the user clock drift rate, and $w_{\dot{\rho}}$ is the measurement error with variance σ^2_{URRE} (URRE: User Range Rate Error). To relate pseudorange rate to Doppler-shift, Equations 3.26a-3.26b can be combined as follows:

$$f_\alpha(1 + \delta\dot{t}_u) - f_{T,\alpha} = -\frac{f_{T,\alpha}}{c}\dot{d}_\alpha \tag{3.28a}$$

$$\frac{-c(f_\alpha - f_{T,\alpha})}{f_{T,\alpha}} = \dot{d}_\alpha + \frac{f_\alpha}{f_{T,\alpha}}c\delta\dot{t}_u \tag{3.28b}$$

The right-hand-side can be simplified since, numerically, $f_\alpha/f_{T,\alpha} \approx 1$ [50]. This leads to the following relation between the Doppler-shift measurement variables and the psuedorange rate variables:

$$\dot{d}_\alpha + c\delta\dot{t}_u = \frac{-c(f_\alpha - f_{T,\alpha})}{f_{T,\alpha}} \tag{3.29}$$

Therefore, the psuedorange rate obtained via differentiation of the position variables is mathematically equivalent to that obtained via Doppler measurements, although as previously noted they may have latency and URRE differences depending on the receiver.

For velocity estimation, the vector of unknowns is $\mathbf{x}^T = [\dot{x}_u, \dot{y}_u, \dot{z}_u, c\delta\dot{t}_u]$. The algorithm is still Gauss-Newton least squares iteration using Equation 3.19 with new variables defined as follows:

$$\Delta\mathbf{y}_k = [\hat{\dot{\rho}}_1(\mathbf{x}_k) - \dot{\rho}_1, ..., \hat{\dot{\rho}}_\alpha(\mathbf{x}_k) - \dot{\rho}_\alpha, ..., \hat{\dot{\rho}}_{N_{GPS}}(\mathbf{x}_k) - \dot{\rho}_{N_{GPS}}]^T \tag{3.30a}$$

$$H_k = [\mathbf{h}_1(\mathbf{x}_k), ..., \mathbf{h}_\alpha(\mathbf{x}_k), ..., \mathbf{h}_{N_{GPS}}(\mathbf{x}_k)]^T \tag{3.30b}$$

$$\mathbf{h}_\alpha^T(\mathbf{x}_k) = \frac{\partial\hat{\dot{\rho}}_\alpha}{\partial\mathbf{x}}(\mathbf{x}_k) = [-\hat{\mathbf{p}}_\alpha^T(\mathbf{x}_k), 1] \tag{3.30c}$$

It is important to note the use of the same H matrix as for position estimation. The velocity error covariance is derived similarly to the position error covariance, treating the pseudorange rate errors between GPS satellites as uncorrelated:

$$\mathrm{E}[\Delta\mathbf{x}\Delta\mathbf{x}^T] = \sigma_{URRE}^2 G \tag{3.31}$$

And since H is the same as before, G is also the same matrix as before, which means that the same DOPs can be used to estimate the velocity standard deviations given the URRE variance using the following formulae:

$$\sigma_{\dot{x}_u} = \sqrt{G_{11}}\ \sigma_{URRE} \tag{3.32a}$$

$$\sigma_{\dot{y}_u} = \sqrt{G_{22}}\ \sigma_{URRE} \tag{3.32b}$$

$$\sigma_{\dot{z}_u} = \sqrt{G_{33}}\ \sigma_{URRE} \tag{3.32c}$$

$$\sigma_v = \sqrt{\sigma_{\dot{x}_u}^2 + \sigma_{\dot{y}_u}^2 + \sigma_{\dot{z}_u}^2} = \mathrm{PDOP}\ \sigma_{URRE} \tag{3.32d}$$

3.7 GPS Measurement Error Estimates

This section will derive expressions for the position and velocity uncertainties associated with GPS measurements and then use simulation to estimate these uncertainties for LEO satellites and CONUS ground stations for later use in relative navigation analysis.

Parkinson et al. give six classes of GPS measurement errors: GPS ephemeris data, GPS satellite clock, ionosphere, troposphere, multipath, and receiver [51]. GPS ephemeris data error is due to error growth in the on-board ephemeris between updates from the ground [51]. GPS satellite clock error is due to drift in the on-board atomic clocks between ground contacts [51]. Note that prior to being discontinued in May 1, 2000, an artificial error called Selective Availability (SA) was intentionally added to the transmitted satellite clock data [51, 44]. The GPS signals do not travel at the vacuum speed of light when passing through the atmosphere, which leads to the ionospheric and tropospheric errors. Note that LEO satellites with an altitude of less than 1000 km are still within the ionosphere; however, they are above the troposphere. Furthermore, GPS receivers correct for atmospheric effects, so it is important for the correction software to be modified for use in LEO to avoid introducing error by correcting for nonexistent tropospheric error [37]. Multipath errors are causes by spurious GPS signals that are reflected from nearby surfaces onto the receiver, a phenomenon which is dependent on GPS antenna placement and the environment [51]. Finally, receiver errors include code tracking loop errors, interchannel bias, and microprocessor precision [51].

One approach to estimating URE and URRE is to make an error budget with estimates for each of the above sources of error [51]. Clearly, the error estimates are dependent on the receiver design details, and a detailed analysis of GPS receiver hardware implementation is beyond the scope of this work. For the interested reader, the Aalto-1 CubeSat GPS receiver design and testing is discussed in depth in Leppinen [38]. For additional reference, the U.S. DoD provides accuracy standards. For example, the Standard Positioning Service (SPS) Signal In Space (SIS) single-frequency

C/A-code accuracy standard is URE $\leq$ 12.8 m & URRE $\leq$ 0.006 m/s 95% global average during normal operations at any Age of Data (AOD), and the 98% global availability standard is PDOP $\leq$ 6 [46].

For another point of reference, the CanX-2 CubeSat was launched in 2008 into a 635 km altitude Sun-synchronous orbit, and it delivered flight results for the NovAtel OEM4-G2 receiver that are summarized by Kahr et al. [37]. One caveat to these results is that this is an older receiver variant with a quoted L1 horizontal RMS position accuracy of 2.16 m (1-σ) and a L1 RMS velocity accuracy of 0.03 m/s (1-σ) [52]. Moreover, the CanX-2 mission experienced operational and hardware difficulties that led to worse receiver performance than anticipated from ground testing, with large error variation between tests. With all channels released, the CanX-2 CubeSat receiver had 3D RMS position errors of 10.8 m to 30.2 m and 3D RMS velocity errors of 0.11 m/s to 0.34 m/s [37]. Systematic biases were noted in these results including unnecessary tropospheric error correction, leading to about -17 m radial position bias error, and timing bias in Doppler measurements, leading to about -0.05 m/s radial velocity bias error [37].

For this work, specifications provided by NovAtel, a popular COTS GPS receiver manufacturer, are used as the starting point. A series of recent receivers as of this writing are the OEM615, OEM719, OEM729, and OEM7600 all of which have a quoted L1 horizontal RMS position accuracy of 1.5 m (1-σ) and a L1 RMS velocity accuracy of 0.03 m/s (1-σ) [53, 54, 55, 56]. NovAtel does not provide URE or URRE data; however, the specifications are said to be based on ground tests conducted on the roof of one of the NovAtel buildings for a period of 24 hours [57]. To estimate the dilution of precision metrics expected in this type of test, an STK simulation was run at epoch 01/01/2019 00:00:00.000 for a period of 30 days with a maximum step size of 1 min, and the direction vectors were computed to visible GPS satellites from the estimated NovAtel ground test coordinates (51.150295°, -114.030733°). The estimated HDOP is 1.273 (95^{th} percentile), and the estimated PDOP is 3.499 (95^{th} percentile). Therefore, $\sigma_{URE} = (1.5 \text{ m})/(\sqrt{2}\text{HDOP}) \approx 0.83$ m, and $\sigma_{URRE} = (0.03 \text{ m/s})/(\sqrt{3}\text{PDOP}) \approx 0.005$ m/s. As expected, this performance is

consistent with DoD accuracy standards. These values are used in the following and in Sections 4.7 and 4.8 for psuedorange and psuedorange rate errors.

To estimate the corresponding position and velocity errors, another dilution of precision simulation was carried out in STK for receivers in LEO orbits. These values are used in Sections 3.8 & 3.9. The simulation parameters were as follows: J2 propagation from the epoch 01/01/2019 00:00:00.000 for a period of 30 days with a maximum step size of 1 minute from 9 different LEO initial conditions of 400, 500, or 600 km altitude, 0.005 eccentricity, 35°, 51.6°, or sun-synchronous inclination (82° – 83° depending on the altitude), −120° RAAN, and 0° argument of perigee. Three different antenna pointing orientations were considered: orbit normal or anti-normal, radial, or canted 45° in-between the normal and radial directions. The VVLH DOP data distributions are shown in Figure 3-3. The statistics are summarized in Table 3.6.

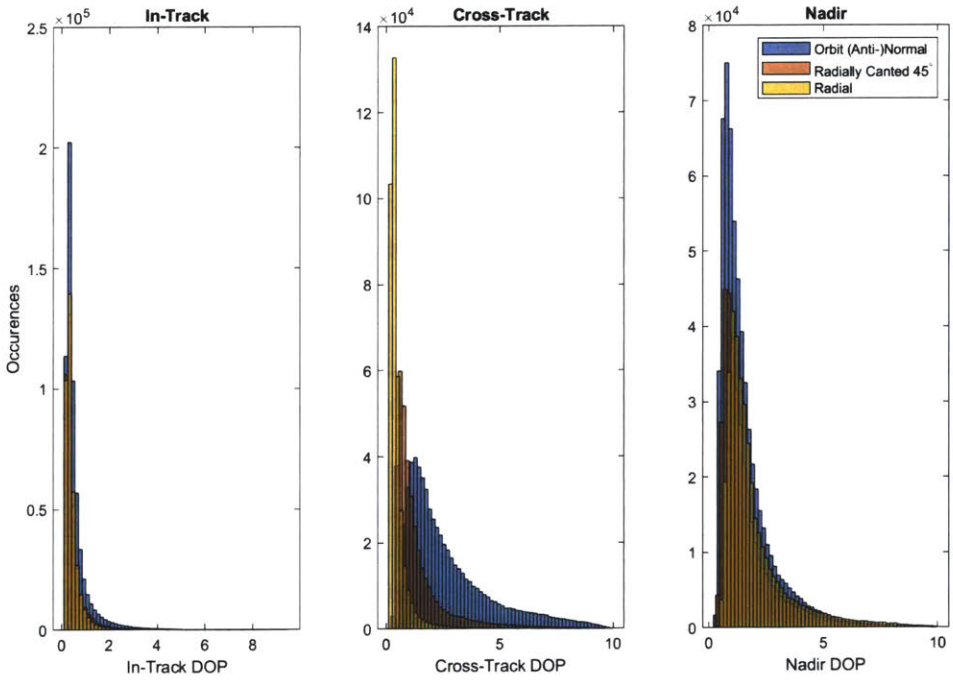

Figure 3-3: VVLH DOP distributions for 400-600 km near-circular LEO satellite receivers.

An important take-away is that the orientation of the receiver has a noticeable effect on the cross-track DOP. The worst orientation is orbit normal pointing with an ap-

proximately 5.4× higher DOP than for radial pointing. The corresponding increase in PDOP is approximately 1.4×. Using Equations 3.25a-3.25d and 3.32a-3.32d, the

Table 3.6: DOP 95th percentile statistics for 400-600 km near-circular LEO satellite receivers using J2 propagation from the epoch 01/01/2019 00:00:00.000 for a period of 30 days.

Orientation	In-Track DOP	Cross-Track DOP	Nadir DOP	PDOP
(Anti-)Normal	1.78	6.92	4.09	8.11
Radially Canted 45°	1.30	4.17	4.41	6.36
Radial	1.11	1.27	5.31	5.71

results in Table 3.6 are translated into position error estimates (Table 3.7) and velocity error estimates (Table 3.8). The same orientation effects are again present, as this a simple scaling of the DOP results. Lastly, similar statistics must be computed

Table 3.7: Estimated (1-σ) position errors for 400-600 km near-circular LEO satellite receivers from the epoch 01/01/2019 00:00:00.000 for a period of 30 days.

Orientation	In-Track (m)	Cross-Track (m)	Nadir (m)	3D-RMS (m)
(Anti-)Normal	1.48	5.77	3.41	6.75
Radially Canted 45°	1.08	3.47	3.67	5.29
Radial	0.92	1.06	4.42	4.75

Table 3.8: Estimated (1-σ) velocity errors for 400-600 km near-circular LEO satellite receivers from the epoch 01/01/2019 00:00:00.000 for a period of 30 days.

Orientation	In-Track (m/s)	Cross-Track (m/s)	Nadir (m/s)	3D-RMS (m/s)
(Anti-)Normal	0.008	0.034	0.020	0.040
Radially Canted 45°	0.006	0.020	0.021	0.031
Radial	0.005	0.006	0.026	0.028

for the optical ground station: the ground station is assumed to be equipped with a GPS receiver, and the raw measurements of the ground station position coordinates from this receiver are stored and optionally processed by the satellite operator and periodically uploaded to the spacecraft. For simulation, the specifications for a low-cost COTS GPS receiver similar to that used by the CLICK-PorTeL optical ground

station [22] are used: 2.5 m horizontal RMS position error [58], with an estimated HDOP of 2.067 (95^{th} percentile) and $\sigma_{URE} = (2.5 \text{ m})/(\sqrt{2}\text{HDOP}) \approx 1.21$ m. The receiver antenna is fixed and zenith pointing. The dilution of precision terms are computed for the aggregate data of the three CONUS ground stations used previously (Secs. 3.4 & 3.5), with the distribution shown in Figure 3-4 and summarized in Tables 3.9 & 3.10. In summary, the URE & URRE error variances that are

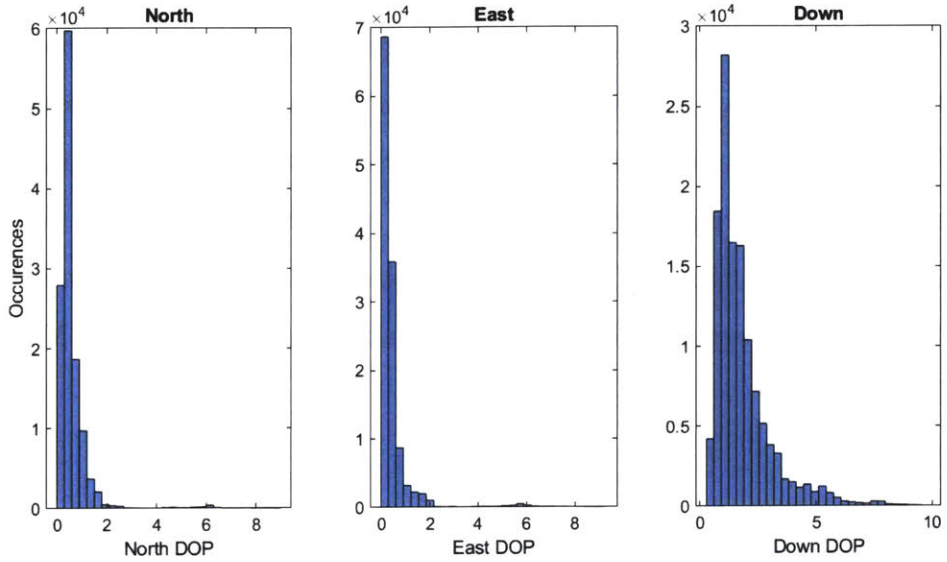

Figure 3-4: North-East-Down (NED) DOP distributions for ground stations in CONUS.

Table 3.9: DOP 95^{th} percentile statistics for ground stations in CONUS from the epoch 01/01/2019 00:00:00.000 for a period of 30 days.

Orientation	North DOP	East DOP	Down DOP	PDOP
Zenith	1.37	1.54	4.58	5.36

Table 3.10: Estimated (1-σ) position errors for ground stations in CONUS from the epoch 01/01/2019 00:00:00.000 for a period of 30 days.

Orientation	North (m)	East (m)	Down (m)	3D RMS (m)
Zenith	1.66	1.86	5.54	6.48

used to model the spacecraft GPS receiver are $\sigma_{\text{URE}} = 0.83$ m and $\sigma_{\text{URRE}} = 0.005$

m/s. Using DOP error analysis for a LEO satellite, the position and velocity errors were estimated for antennas oriented in the (anti-)normal direction, radial direction, or canted at 45° between the normal and radial directions. It was found that the cross-track DOP increased as the antenna is oriented away from the radial direction, with a 1.4× increase in PDOP for (anti-)normal pointing relative to radial pointing. For the purposes of further analysis, the worst case (anti-)normal pointing is assumed, with a PDOP of 8.11 and corresponding 3D RMS position error of 6.75 m and 3D RMS velocity error of 0.040 m/s. In the following simulations, the VVLH error components for this antenna configuration as listed in Tables 3.7 & 3.8 are added to the true VVLH position components. The optical ground station is also equipped with GPS receiver with different specifications: $\sigma_{\text{URE}} = 1.21$ m. The DOP values were computed for the same three CONUS ground station locations as previous analyses (Section 3.5), with the aggregated PDOP = 5.36 and corresponding 3D RMS position error of 6.48 m.

3.8 Propagation of GPS Measurements for Crosslinks

Tables 3.11 and 3.12 summarize the simulation results of direct propagation of GPS fixes for crosslinks at the CLICK boundary ranges of 25 & 580 km, respectively. The simulation implementation is similar to that of Section 3.3, with the difference being the introduction of random noise to the initial condition as per the estimated GPS measurement errors in Tables 3.7 & 3.8. The worst-case antenna pointing configuration (orbit (anti-)normal) is used for the DOP values, and unbiased Gaussian white noise ($N(0, \sigma)$) is added component-wise to the initial conditions for each propagation interval.

These results are the complete relative navigation error comprised of GPS measurement error and model error. One trend that is apparent in these results is the compounding position error effect as the interval size grows due to the displacements in the initial conditions created by the GPS error. The target position error grows consistently from ~5 m to ~340 m as the target interval increases despite the si-

multaneously improving force models, which taken alone had an error growth of only ~0.5 m to ~50 m (Sec. 3.3).

As previously discussed, the case that is representative of CLICK B/C operations is the 1 minute host and 10 minute target interval case (row 2 in both tables). These configurations define the CLICK baseline for relative navigation during crosslink and were used in Chapter 2's pointing budgets. For this configuration, GPS error accounts for 57% of the total error in the 25 km case and 52.6% of the total error in the 580 km case. Although the GPS and model errors are roughly even for this configuration, for the other configurations the GPS error is significantly greater than the model error. For the symmetric 1 minute interval case at 25 km, the GPS error accounts for 97.3% of the total error; and, for the 90 minute target interval case at 25 km, the GPS error accounts for 82.3% of the total error. This indicates that the relative navigation system performance can be improved even further by post-processing GPS measurements using a tool like a Kalman filter, which will be the subject of Chapter 4. Across all cases, the results show that using only an appropriate central body

Table 3.11: Error magnitudes (99^{th} percentile) for direct propagation of GPS measurements for CLICK short range (25 km) LEO crosslink for various propagation configurations.

Δt_H (min)	Δt_T (min)	Host Model	Target Model	Host Pos. Err. (m)	Target Pos. Err. (m)	Range Err. (m)	Angle Err. (μrad)
1	1	J_2	J_2	15.43	15.00	5.111	843.8
1	**10**	$\mathbf{J_2}$	$\mathbf{4 \times 4}$	**16.04**	**47.13**	**18.00**	**1367**
10	10	4×4	4×4	46.05	45.70	21.54	1524
10	30	4×4	14×14	45.67	108.4	79.69	1851
10	90	4×4	100×100	45.90	335.6	288.5	1832

gravity model to directly propagate GPS position & velocity fixes, the position error can be maintained less than ~340 m for intervals up to 90 minutes and less than ~50 m for intervals up to 10 minutes. This corresponds to 99^{th} percentile angular errors of less than ~2000 μrad at 25 km and less then ~200 μrad at 580 km. Using the Rayleigh approximation for the pointing error and including the other error budget terms in Table 2.2, the 99.7% pointing loss is therefore less than ~ -1.235

Table 3.12: Error magnitudes (99^{th} percentile) for direct propagation of GPS measurements for CLICK long range (580 km) LEO crosslink for various propagation configurations.

Δt_H (min)	Δt_T (min)	Host Model	Target Model	Host Pos. Err. (m)	Target Pos. Err. (m)	Range Err. (m)	Angle Err. (μrad)
1	1	J_2	J_2	16.42	15.71	4.756	36.20
1	**10**	**J_2**	**4×4**	**15.53**	**43.08**	**15.81**	**76.58**
10	10	4×4	4×4	43.42	48.17	20.45	98.96
10	30	4×4	14×14	46.69	110.9	77.09	150.4
10	90	4×4	100×100	47.46	337.7	279.3	136.7

dB at 25 km and ~ -0.427 dB at 580 km. The corresponding margins compared to the reference requirement of -1.5 dB are greater than 0.265 dB and 1.073 dB, respectively. Given these results, not only is direct propagation of GPS fixes without additonal processing sufficient for CLICK crosslink relative navigation, but any of alternative relative navigation configurations analyzed here are also sufficient. Therefore, given the CLICK beacon geometry and crosslink ranges along with a modern, high-precision GPS receiver similar to what is used in this analysis, the maximum acceptable target interval duration is only limited by fidelity of the on-board force model. However, given the practical challenges and risks associated with modifying the COTS navigation software is used for CLICK, the upper limit of 10 minutes for the target interval will be maintained for the CLICK mission.

Future missions with hardware and ranges similar to CLICK could potentially increase operational flexibility and further reduce GPS receiver & inter-satellite communications power requirements by further extending the target interval and implementing corresponding force models of equal or higher fidelity than those recommended here. Moreover, future missions may also have stricter pointing requirements if shorter ranges or a narrower beacon are necessary. For example, given a FWHM beacon divergence half that of CLICK (0.375°), the anticipated upper bound pointing losses increase to -4.941 dB at 25 km and -1.708 dB at 580 km, which do not meet the desired pointing loss of -1.5 dB. In this case, assuming additional beacon power is not available to compensate (+238 mW avg. power), further accuracy would

be needed, and processing of GPS measurements would be a software-only solution. This will be explored in detail in Chapter 4.

In summary, the addition of GPS measurement error causes relative navigation error to increase and compound over longer intervals despite improved force models. Nevertheless, using only aspherical gravity force models, the navigation error can be maintained to less than ~340 m over intervals of 90 minutes and less than ~50 m for intervals less than 10 minutes. Across all configurations, the 99^{th} percentile angular errors were less than ~2000 μrad at 25 km and less then ~200 μrad at 580 km, corresponding to 99.7% pointing losses less than -1.235 dB at 25 km and -0.427 dB at 580 km and corresponding margins greater than 0.265 dB and 1.073 dB, respectively. Therefore, given sufficient force modeling for intervals up to 90 minutes, unprocessed GPS measurements can be used with the CLICK hardware, and sufficient pointing accuracy can be maintained, which is the plan for CLICK. However, for future missions with worse GPS hardware performance and/or stricter pointing requirements like reduced minimum range or beacon divergence, GPS measurement processing is recommended, which will be the subject of Chapter 4.

3.9 Propagation of GPS Measurements for Downlinks

For downlinks, there are GPS measurement error contributions for both the satellite position and the ground station position. The GPS measurement errors discussed in Section 3.10 are directly added to the satellite propagator initial conditions and to the stored ground station coordinates without any statistical processing to reduce noise. The results are summarized in Table 3.13. The baseline CLICK mission case is row 4 of Table 3.13, which was used for the error analysis in Chapter 2.

These results are the complete relative navigation error comprised of GPS measurement error and model error. One clear take-away is that the Earth rotation model error is insignificant compared to the ground station GPS error if the 3D RMS po-

sition error is on the order of 1 m or less, which is the case for all models of equal or higher fidelity to the 15-term model with select EOPs (1.18 m 3D RMS position error). For example, the baseline case for 1 minute intervals with the IAU-00/06 B model has a target model error of 0.015 m, which only accounts for 0.1% of the target error when GPS error is added. This causes the GPS noise to dominate the error in these cases, and the distinction between these models and a perfect transformation to disappear in the navigation statistics. This means that the 15-term model with select EOPs could be used instead of baseline the IAU-00/06 B model for computational cost savings without any impact on relative navigation performance. Furthermore, the

Table 3.13: Error magnitudes (99^{th} percentile) for for direct propagation of GPS measurements for LEO downlink to CONUS for various propagation & ECI-ECEF transform configurations. Reference geodetic coordinates (Latitude, Longitude): Boston (42.360636°, $-71.093418°$), Boulder (40.006891°, $-105.264983°$), Los Angeles (34.068851°, $-118.444692°$).

Δt_H (min)	Host Model	ECI-ECEF Transform	Host Pos. Err. (m)	Target Pos. Err. (m)	Range Err. (m)	Angle Err. (μrad)
1	J_2	4-term X,Y Only	14.61	23.41	22.07	33.90
1	J_2	4-term X,Y & ΔUT1	14.61	16.84	14.69	22.22
1	J_2	15-term X,Y & x_p, y_p, ΔUT1	14.61	14.47	10.98	16.36
1	**J_2**	**IAU-00/06 B & All EOP**	**14.61**	**14.58**	**11.13**	**17.29**
1	J_2	None	14.61	15.34	10.90	17.31
10	4×4	4-term X,Y Only	46.34	23.53	32.03	43.43
10	4×4	4-term X,Y & ΔUT1	46.34	16.36	29.56	35.35
10	4×4	15-term X,Y & x_p, y_p, ΔUT1	46.34	14.33	28.37	29.86
10	4×4	IAU-00/06 B & All EOP	46.34	14.35	26.55	32.44
10	4×4	None	46.34	14.24	27.64	31.14

overall 99^{th} percentile error across all cases is less than $\sim$45 μrad, which corresponds to 99.7% pointing losses of less than -0.434 dB with margins greater than 1.066 dB across all cases. This means that any of the relative navigation configurations analyzed here could be used, and the pointing requirement would still be met. Moreover, computational cost savings could be realized by using the simple 4-term Earth rotation model without EOPs. This also would reduce operational overhead, as EOPs are data that is uploaded from the ground. Again, due to the COTS nature of the CLICK

navigation software, the baseline case will be used for the CLICK mission; however, future missions could benefit from these software modifications. Finally, although GPS measurement processing could reduce the relative navigation error, the downlink pointing budget is currently dominated by the assembly & calibration error term, which means that to see benefits from measurement processing, the opto-mechanical design for assembly & calibration would need to be improved first. Assuming this would be the case for future missions with more stringent requirements, GPS measurement processing could again be useful for performance improvement.

In summary, the overall 99^{th} percentile error across all cases is less than $\sim$45 μrad, which corresponds to 99.7% pointing losses of less than -0.434 dB with margins greater than 1.066 dB across all cases, which means that the pointing requirement is met for any of the relative navigation configurations analyzed, and cost savings can be had by simplifying the Earth rotation model to a 4-term X, Y series without EOPs. Furthermore, assuming the assembly & calibration error can be reduced for future missions, GPS measurement processing would improve performance, which will be the subject of the next chapter.

3.10 Chapter 3 Summary

This chapter first analyzed the state propagation algorithm in depth, followed by a discussion on how GPS position & velocity fixes are generated and their noise properties, before finally combining these two ideas to estimate the relative navigation error by directly propagating GPS fixes, which is the baseline configuration for CLICK.

Section 3.1 defined Cowell's method for orbit propagation, which uses two-body gravitational acceleration plus a perturbation acceleration. The perturbation acceleration is computed via the sum of additional forces being considered beyond Keplerian two-body gravity. In Earth orbit, these generally can include aspherical Earth gravity terms, atmospheric drag, solar radiation pressure, third body perturbations, tides, earth radiation pressure, relativistic effects, and thrusting maneuvers.

Next, in Section 3.1.1, the magnitudes of perturbing accelerations were compared, and the sequence of force model simplifications for comparison was determined to be 1) eliminate tides, 2) eliminate third body perturbations, 3) eliminate SRP, 4 & 5) substitute simplified atmospheric models for NRLMSISE00, 6) eliminate drag, 7-9) truncate central body gravity to lower order square models, 10) use a J_2 model, and 11) use a two-body model.

These simplified force models were analyzed for position propagation accuracy in Section 3.2. To achieve a position propagation accuracy of $\sim$ 25 m for crosslinks, the simplified models chosen were J_2 for $\Delta t = 1$ minute, 4×4 for $\Delta t = 10$ minutes, 14×14 for $\Delta t = 30$ minutes, and 100×100 for $\Delta t = 90$ minutes. The same respective models are chosen for the 1 & 10 minute intervals used for downlink.

Next, the error induced by using these simplified models for crosslinks was assessed in Section 3.3. Using only the appropriate central body gravity model, model-induced propagation error was maintained less than 50 m for intervals up to 90 minutes and less than 25 m for intervals up to 30 minutes. This corresponded to 99^{th} percentile angular errors of less than 600 μrad at 25 km and less then 40 μrad at 580 km.

Prior to relative navigation analysis for downlinks, ECI-ECEF transformations were discussed, and the position errors incurred by using simplified models with re-

duced computational costs were compared in Section 3.4 for 3 CONUS ground station locations. Even with the simplest 4-term X, Y series without EOPs, position error remained less than 16 m, which corresponds to about 9-16 μrad of angular error for the median downlink ranges of about 1000-1700 km. Moreover, ECI-ECEF transformations are used in orbit propagation for the aspheric gravity perturbation accelerations, and for intervals on the order of 15 minutes or less, a truncated ECI-ECEF model is not considered to impact satellite orbit prediction significantly for relative navigation purposes and is therefore also a feasible option for reducing computational costs for the host position prediction.

Next, in Section 3.5 these models were compared for relative navigation in combination with the orbit propagation models. All cases had a 99^{th} percentile model-induced error of less than 32 μrad, which is on the order of the point-ahead error (50.36 μrad).

Proceeding to the incorporation of GPS error, section 3.6 derived the position and velocity uncertainty as a function of the DOP parameters and the URE & URRE. Section gave the GPE error metrics used for further analysis. For this analysis, the specified spacecraft GPS receiver was determined to have $\sigma_{\text{URE}} = 0.83$ m and $\sigma_{\text{URRE}} = 0.005$ m/s. For a LEO satellite, it was found that the cross-track DOP increased as the antenna is oriented away from the radial direction, with a 1.4$\times$ increase in PDOP for (anti-)normal pointing relative to radial pointing. For the purposes of further analysis, the worst case (anti-)normal pointing was assumed, with a PDOP of 8.11, corresponding 3D RMS position error of 6.75 m, and 3D RMS velocity error of 0.040 m/s. The optical ground station is also equipped with GPS receiver with different specifications: $\sigma_{\text{URE}} = 1.21$ m. The DOP analysis aggregated over the same 3 CONUS ground stations yielded PDOP = 5.36 and a 3D RMS position error of 6.48 m.

Section 3.8 analyzed the baseline relative navigation error for crosslinks by combining orbit propagation with raw GPS fixes. With the GPS specifications provided, the navigation error was maintained to less than $\sim$340 m over intervals of 90 minutes and less than $\sim$50 m for intervals less than 10 minutes by using only aspherical

gravity force models to directly propagate GPS fixes without processing. Across all configurations, the 99$^{\text{th}}$ percentile angular errors were less than $\sim$2000 μrad at 25 km and less then $\sim$200 μrad at 580 km, corresponding to 99.7% pointing losses less than -1.235 dB at 25 km and -0.427 dB at 580 km and corresponding margins greater than 0.265 dB and 1.073 dB, respectively. Therefore, given sufficient force modeling for intervals up to 90 minutes, unprocessed GPS measurements can be used with the CLICK hardware, and sufficient pointing accuracy can be maintained, which is the plan for CLICK. For future missions with worse GPS hardware performance and/or stricter pointing requirements like reduced minimum range or beacon divergence, GPS measurement processing is recommended.

Similar analysis was carried out for downlinks in Section 3.9. The overall 99$^{\text{th}}$ percentile error across all cases was less than $\sim$45 μrad, which corresponds to 99.7% pointing losses of less than -0.434 dB with margins greater than 1.066 dB across all cases. This means that the pointing requirement is met for any of the relative navigation configurations analyzed, and computational cost savings can be had by simplifying the Earth rotation model to a 4-term X, Y series without EOPs. Furthermore, assuming the assembly & calibration error can be reduced for future missions and/or assuming significantly poorer GPS performance, GPS measurement processing could also improve performance for downlink relative navigation. GPS measurement processing for improved relative navigation performance will be the subject of the next chapter.

Chapter 4

Kalman Filtering for GNSS-Based Relative Navigation

The Kalman Filter [59] is a widely used framework for the estimation of the state of a dynamical system when given noisy measurements [47, 60, 61]. The Extended Kalman Filter (EKF) uses linearization to extend the linear Kalman filter to the nonlinear case. The EKF can be separated into two main subroutines: correction and prediction. There are three EKF formulations that will be studied for this application: 1) the Conventional EKF (CEKF); 2) the Joseph Sequential EKF (JSEKF); 3) the UD Sequential EKF (UDSEKF). These three formulations are compared on three metrics: the time complexity of implementation, the filter consistency, and accuracy for orbit determination using GPS measurements. The best performer is analyzed further, and its orbit determination uncertainties are used for a full relative navigation analysis to compare against the unfiltered results from Chapter 3.

4.1 The Extended Kalman Filter

The Extended Kalman Filter (EKF) can be formulated in continuous time, discrete time, or as a hybrid continuous-discrete system. For orbit determination, the dynamics are formulated in continuous time, and the GNSS measurements are discrete. The

general continuous-discrete system of this type is defined as follows [60]:

$$\dot{\mathbf{x}}(t) = \mathbf{f}(\mathbf{x}(t), \mathbf{u}(t), t) + G(t)\mathbf{w}_{\mathbf{x}}(t) \tag{4.1a}$$

$$\mathbf{y}_k = \mathbf{h}(\mathbf{x}_k) + \mathbf{w}_{\mathbf{y}_k} \tag{4.1b}$$

where $\mathbf{y}_k = \mathbf{y}(t_k) \in R^m$ is the measurement, $\mathbf{w}_{\mathbf{y}_k} \sim N(\mathbf{0} \in R^m, R_k)$ is the measurement noise modeled as an unbiased Gaussian process, $\mathbf{x} \in R^n$ is the state of the plant, $\mathbf{w}_{\mathbf{x}}(t) \sim N(\mathbf{0} \in R^p, Q(t))$ is the process noise, and $\mathbf{u} \in R^r$ is the control input to the plant (if the estimator is part of a control loop). In general, the continuous-discrete EKF is analytically formulated as follows [60]:

$$\hat{\mathbf{x}}(t_0) = \hat{\mathbf{x}}_0, P_0 = E[\tilde{\mathbf{x}}(t_0)\tilde{\mathbf{x}}^T(t_0)] \tag{4.2a}$$

$$K_k = P_k^- H_k^T (H_k P_k^- H_k^T + R_k)^{-1} \tag{4.2b}$$

$$H_k = \frac{\partial \mathbf{h}}{\partial \mathbf{x}}(\mathbf{x}_k^-) \tag{4.2c}$$

$$\hat{\mathbf{x}}_k^+ = \hat{\mathbf{x}}_k^- + K_k(\mathbf{y}_k - h(\mathbf{x}_k^-)) \tag{4.2d}$$

$$P_k^+ = (I - K_k H_k) P_k^- \tag{4.2e}$$

$$\dot{\hat{\mathbf{x}}}(t) = \mathbf{f}(\hat{\mathbf{x}}(t), \mathbf{u}(t), t) \tag{4.2f}$$

$$\dot{P}(t) = F(t)P(t) + P(t)F^T(t) + G(t)Q(t)G^T(t) \tag{4.2g}$$

$$F(t) = \frac{\partial \mathbf{f}}{\partial \mathbf{x}}(\mathbf{x}(t), \mathbf{u}(t), t) \tag{4.2h}$$

where $\hat{\mathbf{x}}_k^- = E[\mathbf{x}|\mathbf{y}_1, ..., \mathbf{y_{k-1}}]$ is the a priori state estimate, $\hat{\mathbf{x}}_k^+ = E[\mathbf{x}|\mathbf{y}_1, ..., \mathbf{y_k}]$ is the a posteriori state estimate, $\tilde{\mathbf{x}} = \hat{\mathbf{x}} - \mathbf{x}$ is the state estimate error, $P_k^- = E[\tilde{\mathbf{x}}_k^- \tilde{\mathbf{x}}_k^{-T}]$ is the a priori error covariance, $P_k^+ = E[\tilde{\mathbf{x}}_k^+ \tilde{\mathbf{x}}_k^{+T}]$ is the a posteriori error covariance, and $K_k \in R^{n \times m}$ is the Kalman gain. Equation 4.2a is the filter initialization step. Equations 4.2b-4.2e are called the correction or measurement-update step, which generates the a posteriori estimates. Equations 4.2f-4.2h give the state and covariance dynamics, which are the basis for the prediction or time-update step that generates the a priori estimates. These steps can be organized at a high level into the structure given in Algorithm 1.

Algorithm 1 Extended Kalman Filter Algorithm Structure

$[\hat{\mathbf{x}}_0^-, P_0^-] = \text{initialize}()$
while online **do**
  return $[\hat{\mathbf{x}}_k^+, P_k^+] = \text{correction}(\hat{\mathbf{x}}_k^-, P_k^-, \mathbf{y}_k)$
  $[\hat{\mathbf{x}}_{k+1}^-, P_{k+1}^-] = \text{prediction}(\hat{\mathbf{x}}_k^+, P_k^+)$
end while

The initialization step can use measurements or previous filtered data, and different initialization strategies such as batch processing, one-point initialization, two-point differencing can be tried depending on the available information [47]. In this study, for orbit determination using GNSS measurements, we simply use the GPS fix at the epoch of the sampling interval and plug in estimated measurement uncertainties to a diagonal initial covariance matrix. There are also alternative formulations to the covariance filter formulation given here called information filters, which propagate the the inverse of the covariance matrix, called the information matrix. This formulation does not require an initialization step; however, it is typically more expensive than covariance filtering unless the measurement dimension is much larger than the state dimension [60]. The correction and prediction subroutine details for a covariance filter formulation will be the topics of the following sections.

In summary, the EKF is used for estimation problems with nonlinear dynamics and/or measurements and can be formulated in continuous time, discrete time, or as a hybrid of both. There are three main steps: filter initialization, correction, and prediction. There are various initialization strategies depending on the available data. For orbit determination, we will use single GPS fixes for state initialization and estimated measurement uncertainties for covariance initialization. The correction and prediction algorithms will be detailed in the following sections.

4.2 The Correction Step

4.2.1 Conventional Correction

Following the nomenclature in Verhaegen et al., we will call the standard implementation of Equations 4.2b-4.2e the Conventional Extended Kalman Filter (CEKF) correction, which is defined in Algorithm 2 [62, 63]. The expression for algorithmic

Algorithm 2 Conventional Extended Kalman Filter Correction [62, 63]

Given $\hat{\mathbf{x}}_k^-, P_k^-, \mathbf{y}_k, R_k$
$H_k = \frac{\partial \mathbf{h}}{\partial \mathbf{x}}(\mathbf{x}_k^-)$
$C_k = H_k P_k^-$
$S_k = C_k H_k^T + R_k$
$K_k = C_k^T S_k^{-1}$
$P_k^+ = P_k^- - K_k C_k$
$P_k^+ = 0.5(P_k^+ + P_k^{+T})$
$\hat{\mathbf{x}}_k^+ = \hat{\mathbf{x}}_k^- + K_k(\mathbf{y}_k - h(\mathbf{x}_k^-))$
return $\hat{\mathbf{x}}_k^+, P_k^+$
Complexity: $O(m^3 + (2m+2)n^2 + 2m^2n + mn + m + n + p_{J_h}(n) + p_h(n))$

complexity is given as a function of the state and measurement dimensions, where $p_h(n)$ and $p_{J_h}(n)$ are the polynomial complexities to evaluate $\mathbf{h}$ and its Jacobian matrix, respectively. We assume that the measurement covariance R_k is computed offline and treat it as constant. Importantly, the covariance update, $P_k^+ = P_k^- - K_k C_k$, is subject to numerical errors that can cause the covariance matrix to become indefinite, leading the filter to diverge [62]. This is addressed in Algorithm 2 by brute force symmetrization ($P = (P + P^T)/2$) of the conventional covariance update. An alternative approach is the so-called Joseph form of the covariance update, shown in Equations 4.3a and 4.3b following the mechanization given in [64]:

$$\bar{P} = P_k^- - K_k C_k \tag{4.3a}$$

$$P_k^+ = (\bar{P} - (\bar{P} H_k^T) K_k^T) + (K_k R_k) K_k^T \tag{4.3b}$$

However, this approach to stability causes the CEKF algorithm complexity to change from that given in Algorithm 2 to $O(m^3 + (4m+3)n^2 + 4m^2n + mn + m + n + p_{J_h}(n) +$

$p_h(n)$), which has larger coefficients for the n^2 and m^2n terms. A different approach to maintaining stability is to reformulate the covariance matrix via factorization, which will be the subject of Section 4.2.3. The computational cost of the correction step can be reduced by eliminating the matrix inversion that generates an $O(m^3)$ complexity term. This is accomplished by taking advantage of an alternative formulation known as sequential measurement processing.

In this section, the Conventional EKF (CEKF) correction algorithm was defined, with a time complexity that includes a $O(m^3)$ term due a matrix inverse step. Furthermore, the standard covariance update step is numerically unstable, and two stabilization approaches were given: brute force symmetrization of the covariance matrix and the Joseph form of the covariance update. The next section will discuss sequential measurement processing, which eliminates the $O(m^3)$ matrix inverse.

4.2.2 Joseph Sequential Measurement Processing

The concept of sequential processing comes from treating the measurement vector as a combination of independent scalar measurements. In general, the measurement covariance will not be diagonal; however, as it is symmetric positive definite, it can be diagonalized in general via an orthogonal similarity transformation: $R = TD_RT^T$, $\mathbf{y} = T\mathbf{z}$, $H = T\mathcal{H}$. In many cases, this diagonalization can be computed offline. We next parse the measurement data by the individual components of $\mathbf{z}$: $z_{k,\alpha} = (\mathbf{z}_k)_\alpha$, $\mathbf{a}_{k,\alpha}^T = \text{row}_\alpha(\mathcal{H}_k)$, and $r_{k,\alpha} = (D_{R,k})_{\alpha,\alpha}$, where $\alpha \in \{1, ..., m\}$. The idea of sequential processing is to loop over these scalar measurement components, applying the Kalman correction iteratively at each step; however, at each step the scalar form of the update equations can be used, replacing matrix inversion with simple division. A proof of equivalence of this formulation and the conventional formulation can be found in Kettner et al., which takes advantage of linearity and the equivalence of the covariance and information forms of the update equations [63]. The sequential processing algorithm for the Joseph form Kalman update is given in Algorithm 3 following Thornton [64]. For simplicity, it is assumed that the measurement covariance diagonalization is computed offline. For memory efficiency, the diagonal elements

of $D_{R,k}$ are stored in a vector $\mathbf{r}_k$. The measurement linearity is essential for the state update in this implementation, so H_k is used to approximate the measurement estimate $\hat{\mathbf{y}} = \mathbf{h}(\hat{\mathbf{x}}_\mathbf{k}^-) \approx H_k \hat{\mathbf{x}}_\mathbf{k}^-$. It should be noted that for some applications with highly nonlinear measurements, this may cause unacceptable errors. The $O(m^2 n)$ term in the complexity comes from the change of basis transformation applied to the measurement Jacobian. Hence, if the measurement is already linear, then this form of the update has complexity with no powers of m greater than 2.

Algorithm 3 Joseph Sequential Extended Kalman Filter Correction [64]

Given $\hat{\mathbf{x}}_k^-, P_k^-, \mathbf{z}_k, \mathbf{r}_k, T$
$\mathcal{H}_k = T^T \frac{\partial \mathbf{h}}{\partial \mathbf{x}}(\mathbf{x}_k^-)$
$P_k^+ = P_k^-$, $\hat{\mathbf{x}}_k^+ = \hat{\mathbf{x}}_k^-$
for $\alpha = 1, ..., m$ **do**
  $\mathbf{a} = (\mathcal{H}_{k,[\alpha,1:n]})^T$
  $\mathbf{c} = P_k^+ \mathbf{a}$
  $\mathbf{k} = \mathbf{c}/(\mathbf{a}^T \mathbf{c} + r_{k,\alpha})$
  $\bar{P} = P_k^+ - \mathbf{k}\mathbf{c}^T$
  $P_k^+ = (\bar{P} - (\bar{P}\mathbf{a})\mathbf{k}^T) + r_{k,\alpha}(\mathbf{k}\mathbf{k}^T)$
  $\hat{\mathbf{x}}_k^+ = \hat{\mathbf{x}}_k^+ + \mathbf{k}(z_{k,\alpha} - \mathbf{a}^T \hat{\mathbf{x}}_k^+)$
end for
return $\hat{\mathbf{x}}_k^+, P_k^+$
Complexity: $O(7mn^2 + m^2 n + 5mn + 3m + p_{J_h}(n))$

In summary, sequential measurement processing treats vector measurements as sequences of scalar measurements, enabling the use of a series of scalar division correction steps instead of using matrix inverse. This eliminates the $O(m^3)$ term due to matrix inversion, and the remaining complexity terms have powers of m less than 2.

4.2.3 UD Sequential Measurement Processing

Matrix factorizations offer memory & processing efficiency while retaining stability. The symmetric positive definite nature of the error covariance matrix P leads to Cholesky factorizations of the following two forms:

$$P = SS^T \tag{4.4a}$$

$$P = UDU^T \tag{4.4b}$$

where $S = UD^{1/2}$ is the so-called square root of P, U is a unit, upper triangular matrix (ones on the main diagonal), and D is diagonal. Two covariance filter formulations that use Equation 4.4a are the Potter Square Root Filter and the Carlson Square Root Filter, where the Carlson form is an improved version of the Potter form [64]. The covariance filter formulation that uses Equation 4.4b is the Thornton-Bierman UD filter [65]. The UD filter with sequential processing has been shown to be the most efficient filter of these three [65, 64, 66]. Hence, the Potter and Carlson filters are not considered further. Furthermore, algorithms that use Cholesky matrix factors of P only need to store its $n(n+1)/2$ degrees of freedom instead of its n^2 entries, which is a memory savings of $50(1-1/n)\%$. For orbit determination with $n = 6$, the memory savings is 41.6%.

The UD filter sequential processing update is shown in Algorithm 4, following the formulation in Gerald & Bierman [65]. The matrix factorization process for P is not part of the UD filter, as only the matrix factors are used throughout. The use of linearized scalar measurement updates is similar to Algorithm 3 and carries the same complexity benefit of eliminating matrix inverses. The diagonal elements of D_k are stored in a vector $\mathbf{d}_k$. The memory improvement over storing P can be gained by storing the off-diagonal elements of U in a vector of length $n(n-1)/2$. For clarity, the matrix form of U is given in Algorithm 4, and for simplicity the dense matrix form is also used in the simulation implementation.

In summary, Cholesky factorization of the covariance matrix leads to the Potter square root filter, Carlson square root filter, and Thornton-Bierman UD filter formulations of the correction algorithm. Of these three, the Thornton-Bierman UD formulation is the most efficient. Furthermore, not only do Cholesky factorization formulations guarantee stability, but they also save on memory usage by $50(1-1/n)\%$. The next section will explore the prediction algorithms for the EKF.

Algorithm 4 *UD* Sequential Extended Kalman Filter Correction [65]

Given $\hat{\mathbf{x}}_k^-, U_k^-, \mathbf{d}_\mathbf{k}^-, \mathbf{z}_k, \mathbf{r}_k, T$
$\mathcal{H}_k = T^T \frac{\partial \mathbf{h}}{\partial \mathbf{x}}(\mathbf{x}_k^-)$
$U_k^+ = U_k^-$, $d_k^+ = d_k^-$, $\hat{\mathbf{x}}_k^+ = \hat{\mathbf{x}}_k^-$
for $\alpha = 1, ..., m$ **do**
  $\mathbf{a} = (\mathcal{H}_{k,[\alpha,1:n]})^T$
  $\mathbf{f} = U_k^{+T}\mathbf{a}$
  $v_i = d_i f_i, \quad i = 1, ..., n$
  $\gamma_1 = r_{k,\alpha} + v_1 f_1$
  $d_{k,1}^+ = d_{k,1}^+ r_{k,\alpha}/\gamma_1$
  $b_1 = v_1$
  $\bar{U} = U_k^+$
  for j = 2,...,n **do**
    $\gamma_j = \gamma_{j-1} + f_j v_j$
    $d_{k,j}^+ = d_{k,j}^+ \gamma_{j-1}/\gamma_j$
    $b_j = v_j$
    $p_j = -f_j/\gamma_{j-1}$
    for i = 1,...,j-1 **do**
      $U_{k,ij}^+ = \bar{U}_{ij} + b_i p_j$
      $b_i = b_i + \bar{U}_{ij}$
    end for
  end for
  $\hat{\mathbf{x}}_k^+ = \hat{\mathbf{x}}_k^+ + \mathbf{b}((z_{k,\alpha} - \mathbf{a}^T\hat{\mathbf{x}}_k^+)/\gamma_n)$
end for
return $\hat{\mathbf{x}}_k^+, U_k^+, \mathbf{d}_k^+$
Complexity: $O(m^2n + 3mn^2 + (3/2)n^2 + 3mn - n/2 + p_{J_h}(n))$ [65]

4.3 The Prediction Step

The state prediction step $\hat{\mathbf{x}}_k^+ \rightarrow \hat{\mathbf{x}}_{k+1}^-$ can be formulated as an initial value problem (IVP) in the ordinary differential equation for the state dynamics (Equation 4.2f). The family of Runge-Kutta methods are popular for solving IVPs and will be discussed in Section 4.3.1. The covariance prediction step $P_k^+ \rightarrow P_{k+1}^-$ can also be formulated as an IVP in a matrix ordinary differential equation (Equation 4.2g); however, solving this matrix IVP is computationally expensive and the alternative approach that will be used here takes advantage of matrix exponential methods, which will be discussed in Section 4.3.2.

4.3.1 State Prediction by Runge-Kutta Methods

There is a vast literature on methods for solving initial value problems, and the selection of an optimal method is problem-dependent. These methods can either use a fixed integration step size or a variable step size. We will first look at a 4^{th} order fixed-step Runge-Kutta method (RK4) following the treatment in Burden & Faires [67]. We will also discuss variable step methods like the Runge-Kutta-Fehlberg (RKF) 4(5) and 7(8) methods and the Dormand-Prince (DP) 5(4) method, which is the algorithm used by MATLAB's ode45 [68]. The IVP is formulated as an explicit nonlinear system of first order ordinary differential equations:

$$t \in [t_k, t_{k+1}] \tag{4.5a}$$

$$\hat{\mathbf{x}}(t_k) = \hat{\mathbf{x}}_k^+, \mathbf{u}(t_k) = \mathbf{u}_k \tag{4.5b}$$

$$\dot{\hat{\mathbf{x}}}(t) = \mathbf{f}(\hat{\mathbf{x}}(t), \mathbf{u}(t), t) \tag{4.5c}$$

$$\hat{\mathbf{x}}_{k+1}^- = \hat{\mathbf{x}}(t_{k+1}) \tag{4.5d}$$

An accuracy metric by which ODE solvers can commonly be judged is local truncation error, which is the accuracy at a given time step relative to the exact solution at the previous time step. It is generally a function of the step-size, denoted by h, and a p^{th} order truncation error $\tau = O(h^p)$. Both Runge-Kutta methods and Taylor methods of order p are characterized by p^{th} order truncation error; however, Runge-Kutta methods do not require evaluation of derivatives of $\mathbf{f}$, rather using repeated evaluation of $\mathbf{f}$ [67]. RK4 is given in Algorithm 5. RK4 has 4 stages and thus has a leading complexity term of $O(N(4np_{\mathbf{g}}(n,r)))$, where $p_{\mathbf{g}}(n,r)$ is the polynomial complexity to evaluate $\mathbf{g}$, and N is the number of time steps in the interval $[t_k, t_{k+1}]$.

Variable step size Runge-Kutta methods have a local error control capability, where the local error is estimated online. The step size is reduced when the algorithm local error is high, which indicates strong nonlinearity, and the step size can be increased otherwise to improve performance. In order to estimate the local error, the algorithm computes a p^{th}-order solution, w, and a $(p+1)^{\text{st}}$-order solution, $\tilde{w}$. The

Algorithm 5 4th Order Runge-Kutta Method for State Prediction [67]

Given $[t_k, t_{k+1}], N, \hat{\mathbf{x}}(t_k) = \hat{\mathbf{x}}_k^+, \mathbf{u}(t)$ for all sample points
Let $\mathbf{g}(\hat{\mathbf{x}}(t), t) = \mathbf{f}(\hat{\mathbf{x}}(t), \mathbf{u}(t), t)$
$h = (t_{k+1} - t_k)/N,\ t = t_k$
for j = 1,...,N **do**
  $\mathbf{k}_1 = h\mathbf{g}(\hat{\mathbf{x}}, t)$
  $\mathbf{k}_2 = h\mathbf{g}(\hat{\mathbf{x}} + \mathbf{k}_1/2, t + h/2)$
  $\mathbf{k}_3 = h\mathbf{g}(\hat{\mathbf{x}} + \mathbf{k}_2/2, t + h/2)$
  $\mathbf{k}_4 = h\mathbf{g}(\hat{\mathbf{x}} + \mathbf{k}_3, t + h)$
  $\hat{\mathbf{x}} = \hat{\mathbf{x}} + (\mathbf{k}_1 + 2\mathbf{k}_2 + 2\mathbf{k}_3 + \mathbf{k}_4)/6$
  $t = t_k + ih$
end for
return $\hat{\mathbf{x}}(t_{k+1})$
Complexity: $O(N(4np_{\mathbf{g}}(n, r) + 5n^2 + 14n + 2))$

step size h is then adjusted by a factor q defined by an inequality of the following form [67]:

$$q \leq c\left(\frac{\epsilon h}{|\tilde{w} - w|}\right)^{1/n} \tag{4.6a}$$

where ϵ is a tolerance on the local truncation error, and c is a constant. For example, RKF 4(5) uses 4th and 5th order estimates to estimate the local error, with $n = 4, c = (1/2)^{1/4}$ [67]. A method which makes further improvements is the DP 5(4) method, which is the current algorithm used in ode45 (it previously used an RKF 4(5) method) [69, 68]. Both RKF 4(5) & DP 5(4) have 6 unique stages; therefore, ignoring the additional arithmetic beyond function evaluation steps, the complexity for RKF 4(5) and DP 5(4) is therefore about $O(N(6np_{\mathbf{g}}(n, r)))$ [68]. RKF 7(8) uses 7th and 8th order estimates with 13 stages for a leading complexity term of $O(N(13np_{\mathbf{g}}(n, r)))$ [40]. It should be noted that the leading complexity terms of higher order methods will only be smaller than lower order methods if the number of steps taken (N) is significantly smaller. Nevertheless, for a given accuracy, higher-order, variable step methods are typically more efficient than lower-order, fixed-step methods [67]. The analysis in Bradley indicates that this trend holds for orbit propagation [40]. The default integrator used for orbit propagation throughout this work is RKF 7(8) with

a tolerance of 10^{-13}, which is the default used by STK's HPOP.

In summary, state prediction consists in solving an IVP, which is commonly accomplished using the Runge-Kutta family of methods. Differences between methods include the order of the truncation error and the use of either fixed or variable step sizes. The leading complexity terms are characterized by the number of stages, which include function evaluation steps. For comparison these are $O(N(4np_{\mathbf{g}}(n,r)))$ for RK4, $O(N(6np_{\mathbf{g}}(n,r)))$ for RKF 4(5) & DP 5(4), and $O(N(13np_{\mathbf{g}}(n,r)))$ for RKF 7(8). For a given accuracy, higher-order, variable step methods typically need to take far fewer steps N than lower-order, fixed-step methods, meaning that they are more efficient. The default integrator used for orbit propagation throughout this work is RKF 7(8). In the next section, covariance prediction will be discussed.

4.3.2 Covariance Prediction

The covariance prediction step must estimate a solution to Equation 4.7, a differential Lyapunov equation that is the simplified form of the differential Riccati equation that describes the full prediction-correction dynamics of the covariance [61].

$$\dot{P}(t) = F(t)P(t) + P(t)F^T(t) + G(t)Q(t)G^T(t) \tag{4.7}$$

However, integrating Equation 4.7 can can be quite costly, with the equivalent state dimension being the number of degrees of freedom of P, which is $n(n+1)/2$. For Equation 4.2g, this leads to an RK4 complexity of $O((N/4)(5n^4 + 22n^3 - 7n^2 - 20n + 8))$, which is potentially the most expensive algorithm so far. However, the matrices involved can be approximated by constant matrices, which enables an alternative approach that converts the continuous equation to a discrete equation using the matrix exponential.

Following the treatment in [61], we define the transformation $\lambda = P\eta$. Plugging this into Equation 4.7 yields the following $2n \times 2n$ first order, Hamiltonian system

[61]:

$$\begin{bmatrix} \dot{\eta} \\ \dot{\lambda} \end{bmatrix} = \begin{bmatrix} -F^T & 0 \\ GQG^T & F \end{bmatrix} \begin{bmatrix} \eta \\ \lambda \end{bmatrix} \equiv \Gamma \begin{bmatrix} \eta \\ \lambda \end{bmatrix} \tag{4.8a}$$

The state transition matrix for this system between time steps is $\Psi(t_{k+1}, t_k) = e^{\Gamma(t_{k+1}-t_k)} = e^{\Gamma \Delta t}$, which leads to the discrete form of Equation 4.8a [61]:

$$\begin{bmatrix} \eta(t_{k+1}) \\ \lambda(t_{k+1}) \end{bmatrix} = \begin{bmatrix} \Psi_{\eta\eta} & \Psi_{\eta\lambda} \\ \Psi_{\lambda\eta} & \Psi_{\lambda\lambda} \end{bmatrix} \begin{bmatrix} \eta(t_k) \\ \lambda(t_k) \end{bmatrix} \tag{4.9a}$$

with solution: (4.9b)

$$P(t_{k+1}) = \left(\Psi_{\lambda\eta} + \Psi_{\lambda\lambda} P(t_k)\right) \left(\Psi_{\eta\eta} + \Psi_{\eta\lambda} P(t_k)\right)^{-1} \tag{4.9c}$$

where $\Psi_{\lambda\lambda} = \Phi$, $\Psi_{\eta\eta} = \Psi_{\lambda\lambda}^{-T}$, and $\Psi_{\eta\lambda} = 0$. Simplifying Equation 4.9c yields [61]:

$$P_{k+1}^- = \Phi_k P_k^+ \Phi_k^T + W_k \tag{4.10a}$$

$$\Phi = e^{F\Delta t} \tag{4.10b}$$

where Equation 4.10a is equivalent to the prediction equation for the fully discrete time EKF, Φ_k is the state transition matrix, and $W_k = \Psi_{\lambda\eta}\Psi_{\lambda\lambda}^T$ is the discretized form of the noise covariance. Equation 4.10b defines the relationship between the linearized dynamics and the discrete state transition matrix, which depends on the computation of a matrix exponential.

In summary, the solution to the continuous dynamics Lyapunov differential equation for the covariance can approximated by the standard discrete time covariance prediction by using the matrix exponential. Algorithms for computing the matrix exponential will be the subject of the following.

The Matrix Exponential

There are many ways to compute a matrix exponential, 19 of which are described in the classic paper by Moler & Van Loan [70]. The most obvious approach is a

truncated Taylor series approximation:

$$e^A \approx T_k(A) = \sum_{k=0}^{N} \frac{1}{k!} A^k \tag{4.11a}$$

Another common approximation is the Pade approximant, which is defined as follows [70]:

$$e^A \approx R_{pq}(A) = Q_{pq}^{-1}(A) P_{pq}(A) \tag{4.12a}$$

$$Q_{pq}(A) = \sum_{j=0}^{p} \frac{p!(p+q-j)!}{j!(p+q)!(p-q)!} A^j \tag{4.12b}$$

$$P_{pq}(A) = \sum_{j=0}^{q} \frac{q!(p+q-j)!}{j!(p+q)!(q-j)!} (-A)^j \tag{4.12c}$$

The problem with this either of these series approaches is that by themselves, they do not take into account how ill-conditioning of the problem can lead to large forward error [70]:

$$\phi(t) = \frac{\left\| e^{t(A+E)} - e^{tA} \right\|}{\left\| e^{tA} \right\|} \tag{4.13a}$$

$$\phi(t) \leq t \left\| E \right\| \exp\left[t(\mu(A) - \alpha(A) + \left\| E \right\|) \right] \tag{4.13b}$$

$$\phi(t) \approx \frac{\left\| E \right\|}{\left\| A \right\|} \kappa(t, A) \tag{4.13c}$$

where E is a matrix perturbation, $\mu(A)$ is the log norm of A (e.g. the maximum eigenvalue of $(A + A^H)/2$), $\alpha(A)$ is the maximum real eigenvalue component in the spectrum of A, and $\kappa(t, A)$ is the condition number of the problem. Importantly, $\kappa(A, t) \geq t \left\| A \right\|$, with equality if the matrix A is normal (e.g. $AA^H - A^H A = 0$), which includes Hermitian, skew-Hermitian, and unitary matrices. Hence, the matrix exponential is well conditioned if A is normal with a small L_2-norm [70]. Therefore, both Taylor and Pade series approaches may fail in the general case.

An approach that remedies this is the scaling and squaring method, which utilizes the identity $e^A = \left(e^{A/\sigma}\right)^\sigma$ with $\sigma = 2^j$ to reduce the norm of the matrix argument [70].

Either of the above approximations may be used, $T_k(A/2^j)^{2^j}$ or $R_{qq}(A/2^j)^{2^j}$, where the diagonal Pade approximant ($p = q$) is used to maximize efficiency. According to Moler & Van Loan, with $10^{-2} \leq \|A\| \leq 10^3$, the scaling and squaring method is generally more efficient when using the diagonal Pade approximant instead of the Taylor approximant [70]. For example, if $\|A\| = 1$, $\phi \leq 10^{-9}\kappa$ requires a 6th order Taylor series with 3 scaling and squaring steps versus a 4th order Pade series with only 1 scaling and squaring step.

Therefore, for the general problem, we will use the scaling and squaring Pade approximant method that is used by MATLAB's **expm**, which is further described by Higham et al. [71, 72]. It is possible to specialize this algorithm to reduce costs in special cases where the necessary scaling and series orders are known. Furthermore, the algorithm is optimized for IEEE double precision floats and therefore can be modified for reduced precision representations. These modifications are not explored in this work. Importantly, the maximum cost of the algorithm for a $M \times M$ matrix is $O([29/3 + \log_2(\|A\|_1 / \theta_{13})]M^3)$, where $\|A\|_1 > \theta_{13} \approx 5.37192$. For example, if $\|A\|_1 = 10$, the cost is $O(10.56M^3)$. If $\|A\|_1 \leq \theta_{13}$, the cost will be lower, and the various expressions for the complexity as a function of $\|A\|_1$ can be found in Higham et al. [72]. The best and worst case complexity expressions are given in Algorithm 6, along with the complexity of the other arithmetic operations involved in the covariance prediction step.

Algorithm 6 Matrix Exponential for Covariance Prediction [61, 71, 72]

Given $\Delta t = t_{k+1} - t_k$, P_k^+, F_k, $\mathcal{W} = G_k Q_k G_k^T$ (computed offline)
$\Gamma = \begin{bmatrix} -F_k^T & 0 \\ \mathcal{W} & F_k \end{bmatrix}$
$\Psi = \mathbf{expm}(\Gamma \Delta t)$
$\Phi = \Psi_{(n+1):2n,(n+1):2n}$
$W = \Psi_{(n+1):2n,1:n}\Phi^T$
$P_{k+1}^- = \Phi P_k^+ \Phi^T + W$
return P_{k+1}^-
Complexity (Best-Case **expm**): $O((8/3)(2n)^3)$
Complexity (Worst-Case **expm**): $O([(29/3 + \log_2(\|\Gamma \Delta t\|_1 / \theta_{13}))](2n)^3)$
Complexity (Other): $O(3n^3 + n^2)$

The baseline implementation of the covariance prediction step is shown in Algorithm 6 (note that $M = 2n$). As discussed above, the matrix exponential can be modified for improved performance in special cases. More generally, approaches that take advantage of the block lower triangular, Hamiltonian matrix structure of Γ may enable further efficiency improvements but are outside the scope of this work [73, 74, 75].

In summary, there are many methods for computing the matrix exponential; however, one of the top performing algorithms is the scaling and squaring Pade approximant method used by MATLAB's **expm**. The complexity of this algorithm is a function of the L_1-norm of the argument to the matrix exponential ($\|\Gamma\Delta t\|_1$), which in the best case reduces to $O(24.3n^3)$. It is possible to improve the performance of this algorithm by taking advantage of the block lower triangular, Hamiltonian matrix structure of Γ. The next section will modify Algorithm 6 for the UD covariance formulation case.

4.3.3 Prediction for the UD Factorization

In order to efficiently utilize the matrix factorizations in Section 4.2.3, the prediction step should not require recombination into P followed by re-factorization, which would be a direct implementation of Algorithm 6, with an additional $O(7n^3/3)$. Instead, an approach developed in parallel with Algorithm 4 can be utilized. The treatment here follows Thornton & Bierman [76]. The starting point is the discrete dynamics, treating the linearized dynamics matrices as constant over the interval: $\mathbf{x}_{k+1} = \Phi_k \mathbf{x}_k + \Upsilon_k \mathbf{w}_{\mathbf{x}k}$. The covariance prediction is $P_{k+1}^- = \Phi P_k^+ \Phi^T + \Upsilon_k Q_k \Upsilon_k^T$. The covariance factor prediction can then be formulated in terms of the UD factorization [76]:

$$\bar{W} = [\Phi_k U_k^+ \mid \Upsilon_k] \tag{4.14a}$$

$$\bar{D} = \begin{bmatrix} D_k^+ & 0 \\ 0 & Q_k \end{bmatrix} \tag{4.14b}$$

$$P_{k+1}^- = \bar{W}\bar{D}\bar{W}^T \tag{4.14c}$$

The matrices Φ_k and Υ_k can be computed with a continuous to discrete transformation via the matrix exponential [77]. The factors U_{k+1}^- & D_{k+1}^- can be computed via a modified weighted Gram-Schmidt orthogonalization of the rows of $\bar{W}$, where the weighting Gram matrix is $\bar{D}$ [78]. The UD covariance prediction step is thus given in Algorithm 7. In summary, the covariance prediction step must be modified for

Algorithm 7 UD Prediction via **expm** and Modified Weighted Gram-Schmidt [76, 77, 78]

Given $\Delta t = t_{k+1} - t_k$, U_k^+, $\mathbf{d}_k^+$, F_k, $G_k \in R^{n\times p}$, $\mathbf{q}_k = \text{diag}(Q_k)$ (or of the diagonalization of Q_k computed offline)

$$\Omega = \begin{bmatrix} F_k & G_k \\ 0_{p\times n} & 0_{p\times p} \end{bmatrix} \in R^{(n+p)\times(n+p)}$$

$\Theta = \mathbf{expm}(\Omega\Delta t)$

$\Phi = \Theta_{1:n,1:n}$

$\Upsilon = \Theta_{1:n,(n+1):(n+p)}$

$\bar{W} = [\Phi U_k^+ \ , \ \Upsilon]$ (row-cat)

$\bar{\mathbf{d}} = [\mathbf{d}_k^+ \ ; \ \mathbf{q}_k]$ (col-cat)

Modified Weighted Gram-Schmidt:

Let $< \mathbf{u}, \mathbf{v} >_{\bar{\mathbf{d}}} = \sum_{i=1}^{n+p} u_i \bar{d}_i v_i$

Let $W = \bar{W}^T$ (column vector data)

for j = n,(n-1),...,1 **do**

  $d_{k+1,j}^- =< W_{:,j}, W_{:,j} >_{\bar{\mathbf{d}}}$

  for i = 1,..,(j-1) **do**

    $U_{k+1,i,j}^- =< W_{:,i}, W_{:,j} >_{\bar{\mathbf{d}}} / d_{k+1,j}^-$

    $W_{:,i} = W_{:,i} - U_{k+1,i,j}^- W_{:,j}$

  end for

end for

return $U_{k+1}^-, \mathbf{d}_{k+1}^-$

Complexity (Best-Case **expm**): $O((8/3)(n+p)^3)$

Complexity (Worst-Case **expm**): $O([(29/3 + \log_2(\|\Omega\Delta t\|_1 / \theta_{13}))](n+p)^3)$

Complexity (MWGS): $O((3/2)(n+p)^3 + (5/2)(n+p)^2 - 2(n+p))$

the UD factorization to avoid incurring the costs of online factorization. This is accomplished by a similar discretization of the continous linearized dynamics via the matrix exponential followed by a modified weighted Gram-Schmidt process that is used to predict the a priori UD terms. The next section will formulate the EKF for the orbit determination problem with GNSS measurements.

4.4 Stochastic Dynamical System for Orbit Determination Using GNSS Measurements

In this study's implementation of the EKF for orbit determination, the state vector is $\mathbf{x} = [\mathbf{r}; \mathbf{v}] = [x, y, z, v_x, v_y, v_z]^T$. The coordinate system is Cartesian Earth-Centered Inertial (ECI). This is the minimal state needed; however, additional parameters may need to be appended to the state if force models are used that include parameters to be estimated like the drag coefficient [79], noise models are used that are not Gaussian white noise processes [47], or out-of-sequence measurements are encountered [80].

Following the analysis in Section 3.2, only central body gravity is included in the dynamics model, and the GNSS position and velocity fixes as per Section 3.6 are used. An alternative formulation that directly processes psuedorange measurements is explored by Bar-Shalom et al. [47].

$$\dot{\mathbf{r}} = \mathbf{v} \tag{4.15a}$$

$$\dot{\mathbf{v}} = \mathbf{a}_{\text{central body}} + \mathbf{w}_{\mathbf{x}} \tag{4.15b}$$

$$\mathbf{y}_k = \begin{bmatrix} \mathbf{r}_k \\ \mathbf{v}_k \end{bmatrix} + \mathbf{w}_{\mathbf{y}k} \tag{4.15c}$$

where $m = n = 6$, $p = 3$. The process noise model follows the same Cowell method discussed Section 3.1.1, which in this case treats all effects beyond a central-body gravity model as disturbance accelerations. The linearization and noise covariance matrices are as follows:

$$F = \begin{bmatrix} 0_{3\times3} & I_{3\times3} \\ \frac{\partial \mathbf{a}_{\text{central body}}}{\partial \mathbf{r}} & 0_{3\times3} \end{bmatrix}, \; G = \begin{bmatrix} 0_{3\times3} \\ I_{3\times3} \end{bmatrix}, \; Q = \sigma_w^2 I_{3\times3} \tag{4.16a}$$

$$H = I_{6\times6}, \quad R = \begin{bmatrix} \sigma_r^2 I_{3\times3} & 0_{3\times3} \\ 0_{3\times3} & \sigma_v^2 I_{3\times3} \end{bmatrix} \tag{4.16b}$$

where the noise covariances are treated as uncorrelated. As gravity is independent of velocity, the velocity gradient of the acceleration vanishes. The expression for the

position gradient is given in Appendix A.8. The position and velocity noise variances that will be used are the orbit (anti-)normal receiver oriented results from Section 3.10. The position and velocity noise are treated as Gaussian white noise processes. Some authors use a combination of Gaussian white noise and Gauss-Markov noise in the position/URE measurement model [47]. As noted before, this requires auxiliary state parameters to estimate the Gauss-Markov noise value in order to reduce the problem back to the Gaussian white noise case. See Bar Shalom et al. for further details on Kalman filtering with Gauss-Markov noise models [47]. The process noise (σ_w) magnitude is estimated by simply summing the unmodeled acceleration statistics from Section 3.1.1. For central body gravity models, these estimates are 1.4×10^{-5} km/s^2 for two-body, 1.4×10^{-6} km/s^2 for J_2, 6.8×10^{-7} km/s^2 for 4×4, 6.8×10^{-8} km/s^2 for 10×10, 1.1×10^{-8} km/s^2 for 21×21, and 3.2×10^{-9} km/s^2 for 70×70. These are order of magnitude estimates, and they are sufficient for this work. Vallado describes more sophisticated methods for process noise estimation to fine tune filters in practice [33].

Additionally, it is preferable to nondimensionalize rather than use SI or similar units because the problem is badly scaled in typical units. For instance, let the state be $\mathbf{x} = [6871, 0, 0, 0, 4, 5]^T$ in km & km/s. Given $\mu \approx 3.986 \times 10^5$ km^3/s^2 as using a two-body central body gravity model, $\kappa(F) = \|F\| \|F^{-1}\| \approx 8.1 \times 10^5$. Therefore, the problem is nondimensionalized according to the following rules: $t \rightarrow t/T$, $T = \sqrt{L^3/\mu_e}$, $L = R_e = 6378.137$ km, $\mu_e = 3.9860044418 \times 10^5$ km^3/s^2, $\mathbf{r} \rightarrow \mathbf{r}/L$, and similar rules for the other unit combinations. With this nondimensionalization, the dynamics model parameters $R_e \rightarrow 1$ and $\mu \rightarrow 1$, where R_e is the equatorial radius of the Earth, and μ_e is the gravitational parameter for the Earth [33]. With nondimensionalization, $\kappa(F) \approx 63$, which is an improvement of 3 orders of magnitude.

In summary, the EKF for orbit determination using GPS measurements is formulated here using the minimal state consisting of the ECI position and velocity, uses a central body gravity model including two-body and aspheric terms appropriate for the propagation interval, and uses GPS position and velocity fixes as discrete-time measurements. The process noise magnitude is estimated via the perturbing accel-

eration analysis of Section 3.1.1, and the GPS receiver orbit (anti-)normal receiver oriented measurement noise from Section 3.10 will be used. Lastly, the problem is ill-conditioned in typical units, so the state is nondimensionalized using the Earth's radius R_e and its gravitational parameter μ_e. The next section will compare the three EKF formulations described previously, CEKF, JSEKF, & UDSEKF, on the metrics of efficiency, consistency, and orbit determination accuracy.

4.5 Filter Comparison

This section will rank the CEKF, JSEKF, and UDSEKF filter formulations on three metrics: efficiency as per analytical time complexity results given previously for each of the subroutines, a statistical hypothesis test for consistency, and 3D-RMS position & velocity estimation errors for orbit determination.

4.5.1 Efficiency

For comparison, the operation counts per step are tabulated for each of the three algorithms along with their in Table 4.1. For simplicity, a two-body dynamics model with RK4 integration and $\Delta t = 1$ second is used for this comparison (Algorithm 5). Higher order gravity models will be more costly for a given integration method. Also, as previously discussed, higher-order, variable-step integrators can be more efficient than fixed-step integration, requiring fewer steps (N) for the same level of accuracy. For two-body dynamics, $p_{\mathbf{g}}(n, r) = p_{\mathbf{f}}(n) = (3/2)n + 2 = 11$. Furthermore, for Algorithm 6, $\|\Gamma\Delta t\|_1 \approx 1.43 \times 10^{-2}$, and for Algorithm 7, $\|\Omega\Delta t\|_1 \approx 1.24 \times 10^{-2}$. Although these matrices are not normal, they do have norms less than $\theta_3 \approx 1.49 \times 10^{-2}$, which means that **expm** is likely to function near minimal computational load in this case: a 3rd order Pade approximant with no scaling or squaring steps, so the best-case complexity for Algorithm 6 is used: $O((8/3)M^3)$. The table estimate uses this best-case for **expm** with $M = 2n = 12$ for 6 and $M = n + p = 9$ for 7. Note that slower GPS sampling results in larger Δt values, which increases computational cost for covariance prediction due to the larger matrix-norm values.

Table 4.1: Operation Counts for CEKF, JSEKF, & UDSEKF for a two-body dynamics model using RK4 integration with $\Delta t = 1$.

CEKF	FLOP Count	JSEKF	FLOP Count	UD-SEKF	FLOP Count
Algo. 5	$O(530N)$	Algo. 5	$O(530N)$	Algo. 5	$O(530N)$
Algo. 6	$O(5292)$	Algo. 6	$O(5292)$	Algo. 7	$O(1944)$
Algo. 2	$O(1200)$	Algo. 3	$O(1926)$	Algo. 4	$O(1023)$
Total	$O(530N + 6456)$	Total	$O(530N + 7218)$	Total	$O(530N + 2967)$

For the CEKF or the JSEKF with $N \leq 10$ and for the UDSEKF with $N \leq 3$, the most costly step is covariance prediction (Algorithms 6 and 7); otherwise, the most costly step is state prediction (Algorithm 5). One way to reduce the operation count for covariance prediction would be to pick a fixed truncation matrix exponential method such as 3rd order Pade approximant without scaling and squaring and expand the block triangular argument matrices, which would lead to a direct computation of the state transition matrix via $\Phi = e^{F\Delta t}$, $O(576)$, along with additional operations by analytic formulae to compute the remaining output [75]. This is not analyzed in this work, but is a good example of how the implementation details of the algorithm depend closely on the problem details for full optimization. Given the implementation described, the ranking of the algorithms from most efficient to least efficient is 1) UDSEKF, 2) CEKF, 3) JSEKF.

4.5.2 Filter Consistency

Filter consistency is defined as the state error obeying its design assumption: that it is zero-mean Gaussian distributed. This is formulated as a χ^2 hypothesis test following the approach in Bar-Shalom et al. [47]. The consistency check can be simplified to a check on a single scalar metric called the Normalized Estimation Error Squared (NEES), which is defined by the quadratic form in the a posteriori information matrix: $\epsilon_k = \tilde{\mathbf{x}}_k^{+T} P_k^{+-1} \tilde{\mathbf{x}}_k^+$. The hypothesis test supports consistency if the average NEES $\bar{\epsilon}_k \in [r_1, r_2]$, where $r_1 = (1/N_{mc}) F_\chi^{-1}((1-\alpha)/2, nN_{mc})$, $r_2 = (1/N_{mc}) F_\chi^{-1}((1+\alpha)/2, nN_{mc})$, F_χ^{-1} is the inverse CDF for the χ^2 distribution, N_{mc} is the number of Monte-Carlo runs, and α is the confidence parameter (set to 0.99 for 99% confidence) [47]. Note

that if the filter is perfect, then $E[\epsilon_k] = n$ (the state dimension). For the simulated implementation, $n = 6$ and the chi-squared 99% bounds are $[r_1, r_2] = [4.50, 7.75]$.

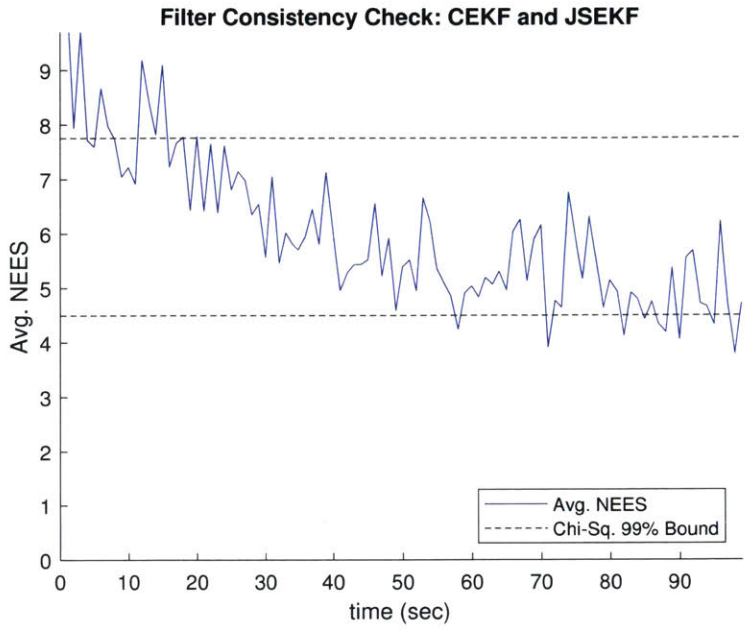

Figure 4-1: Average NEES timeseries for 30-run Monte-Carlo simulation of CEKF and JSEKF for 1 second measurement sampling with a two-body force model. Average for $t \in [50, 100]$ is 5.11.

The time behaviors of the average NEES are shown in Figures 4-1 and 4-2. The result for the CEKF and JSEKF was identical, and the UDSEKF performed with slightly higher average NEES values. To characterize the settled behavior, it is averaged over the interval $t \in [50, 100]$ seconds, and the resulting average NEES values are as follows: CEKF 5.11; JSEKF 5.11; UDSEKF 6.85. This result shows that upon settling, all three filter implementations pass the χ^2 hypothesis test on average, with a deviation of the time-average from the ideal value of 0.89 for CEKF & JSEKF and a slightly smaller deviation of 0.85 for the UDSEKF. Therefore, on the metric of consistency, the three filters score equally.

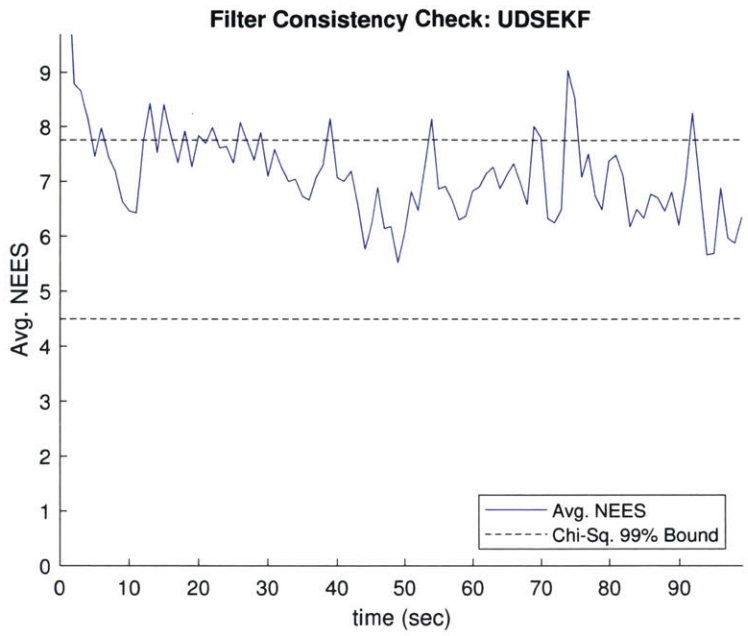

Figure 4-2: Average NEES timeseries for 30-run Monte-Carlo simulation of UDSEKF for 1 second measurement sampling with a two-body force model. NEES time-average of averages for $t \in [50, 100]$ is 6.85.

4.5.3 Orbit Determination Accuracy

The final metric for comparison is filter accuracy when applied to the orbit determination problem using GPS measurements. For simplicity, this comparison is limited to a single orbit case with a 1 second sampling time (T_s) and a two-body force model. More detailed analysis with other sampling intervals, force models, and orbits will be done in later sections with the best performing filter. The orbit used here is at a 500 km altitude and 51.6° inclination, with other initial elements the same as previous simulations (Sec. 3.10). For each filter, there are 30 simulation trials with each trial being $100T_s = 100$ seconds. For error analysis, a settling time must be selected to parse the results. Figure 4-3 shows the position and velocity error convergence for an example sampling interval using the UDSEKF. Figure 4-4 shows the filter's estimate of the error covariance for position and velocity where $\hat{\sigma}_r = \sqrt{P_{11}^2 + P_{22}^2 + P_{33}^2}$ and $\hat{\sigma}_v = \sqrt{P_{44}^2 + P_{55}^2 + P_{66}^2}$. It can be seen here that the filter convergence occurs within the first 50 samples, which in this case corresponds to 50 seconds. Hence, the latter-half of the trial intervals are used to aggregate data for statistical analysis of

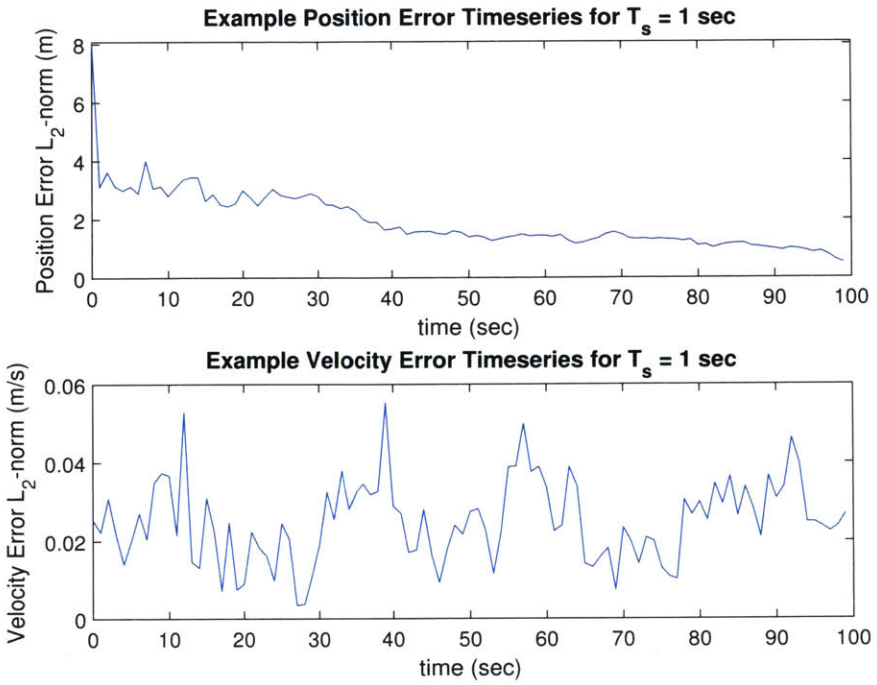

Figure 4-3: Measurement data interval processing example result for position and velocity error. Uses the UDSEKF for 1 second measurement sampling with a two-body force model.

Table 4.2: Estimated RMS position and velocity errors for the CEKF, JSEKF, & UDSEKF implementations for a 500 km altitude and 51.6° inclination near-circular low-Earth orbit will $T_s = 1$ second.

EKF Type	3D-RMS Position Error (m)	Noise Reduction	3D-RMS Velocity Error (m)	Noise Reduction
CEKF	0.425	15.9×	0.019	2.1×
JSEKF	0.425	15.9×	0.019	2.1×
UDSEKF	0.394	17.1×	0.011	3.6×

the settled filter behavior. Table 4.2 gives the 3D RMS position and velocity errors for each of the three filter formulations. The noise reduction is computed relative to the raw GPS 3D RMS position and velocity errors from Section 3.10: 6.75 m and 0.040 m/s, respectively. The CEKF and JSEKF perform equally, and the UDSEKF is the best performer. Therefore, on the basis of orbit determination accuracy, the ranking is 1) UDSEKF and 2) CEKF & JSEKF.

In summary, on the first metric of efficiency, the ranking of the algorithms is 1)

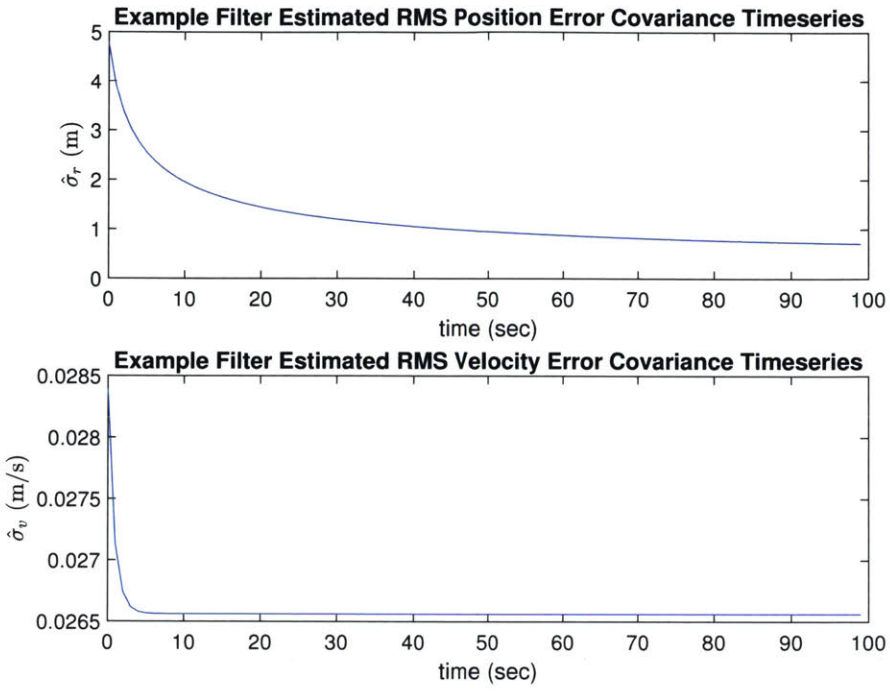

Figure 4-4: Measurement data interval processing example result for estimated position and velocity error covariance (RMS of respective diagonal elements of the a posteriori estimated error covariance matrix). Uses the UDSEKF for 1 second measurement sampling with a two-body force model.

UDSEKF, 2) CEKF, 3) JSEKF. On the metric of consistency, the three filters score equally. Lastly, on the metric of orbit determination accuracy, the ranking is 1) UDSEKF and 2) CEKF & JSEKF. Therefore, the overall ranking is 1) UDSEKF, 2) CEKF, 3) JSEKF. Hence, the UDSEKF is the best performing formulation overall, and it is therefore selected for further analysis.

4.6 Error Estimates for Kalman Filtered GPS Measurements

As per the discussion in Section 3.2, the maximum sampling interval is the maximum Host propagation interval, which is 10 minutes. Table 4.3 summarizes the position and velocity estimation error results for the UDSEKF applied to three different measurement sampling periods with appropriate force models.

Table 4.3: Estimated RMS position and velocity errors for filtered GPS measurements with different measurement sampling intervals (T_s) and corresponding force models.

T_s	EKF Model	3D-RMS Position Error (m)	Noise Reduction	3D-RMS Velocity Error (m)	Noise Reduction
1 sec	2-Body	0.425	15.9×	0.019	2.1×
1 min	J_2	1.615	4.2×	0.017	2.4×
10 min	14×14	2.982	2.3×	0.012	3.3×

Note that the 10 min interval uses a 14×14 model for filtering, which is higher order than the propagation model used previously. This is because it was found that the 4×4 model was introducing sufficient prediction error that the filtered state errors were still similar in magnitude to the unfiltered state errors. Again, even for measurement intervals up to 10 minutes, the position and velocity estimation errors are reduced by at least a factor of 2 and up to a factor of 16 for position error in the 1 second sampling case. As the interval increases, the propagation error causes the position error to increase, though interestingly the velocity error slightly decreases. It should also be noted that the matrix exponential approach to covariance prediction assumes a relatively short propagation interval, which could also be a contributor to the increase in position error. If the interval is extended further, a multi-step correction could be used to reduce the Δt value could be used, or the matrix IVP could be solved at the cost of efficiency.

In summary, applying the UDSEKF to sampling intervals (T_s) from 1 second up to 10 minutes yields improvements in the 3D-RMS position and velocity errors of at least 2× relative to unfiltered GPS fixes. These filtered uncertainties will be used for

relative navigation analysis in the next sections analogous to that of Sections 3.8 & 3.9 to compare using filtering for orbit determination against using raw GPS fixes.

4.7 Propagation of Kalman Filtered GPS Measurements for LEO Crosslinks

Tables 4.4 and 4.5 summarize the results of propagating GPS measurements that have been processed using an EKF as per Section 4.6. The simulations are identical to those in Section 3.8, except that the position and velocity noise variances have been replaced with the results from Table 4.3. Specifically, the EKF variances are selected to match the Host interval, which in this case matches the GPS measurement sample time. In practice, for even higher performance, the sampling time could be reduced to 1 second if necessary. However, even with a relatively slow sampling time of 1 minute, filtering reduces the Host position error by about 4.5× from 15.4 m down to 3.4 m. For the baseline 25 km scenario with a Host interval of 1 minute and a Target interval of 10 minutes (row 2 of Table 4.4), the angular error reduced by about 2× from 1367 μrad for unfiltered GPS measurements to 685.1 μrad. More generally, the angular error reduction of at least 2× was true across most scenarios. Note that although the EKF error estimates for the 10 minute sampling interval used a 14 × 14 force model, the propagation error estimates here use a 4 × 4 force model for consistency with the presentation of previous propagation error results.

Table 4.4: Error magnitudes (99^{th} percentile) for propagation of Kalman filtered GPS measurements for CLICK short range (25 km) LEO crosslink for various propagation configurations.

Δt_H (min)	Δt_T (min)	Host Model	Target Model	Host Pos. Err. (m)	Target Pos. Err. (m)	Range Err. (m)	Angle Err. (μrad)
1	1	J_2	J_2	3.357	3.461	3.032	166.2
1	**10**	**J_2**	**4 × 4**	**3.453**	**25.84**	**13.26**	**685.1**
10	10	4 × 4	4 × 4	26.53	25.08	12.40	615.5
10	30	4 × 4	14 × 14	23.20	48.48	34.55	792.5
10	90	4 × 4	100 × 100	23.33	274.6	234.5	856.2

Table 4.5: Error magnitudes (99^{th} percentile) for propagation of Kalman filtered GPS measurements for CLICK long range (580 km) LEO crosslink for various propagation configurations.

Δt_H (min)	Δt_T (min)	Host Model	Target Model	Host Pos. Err. (m)	Target Pos. Err. (m)	Range Err. (m)	Angle Err. (μrad)
1	1	J_2	J_2	3.237	3.439	3.070	7.771
1	**10**	**J_2**	**4×4**	**3.487**	**26.72**	**13.10**	**43.38**
10	10	4×4	4×4	26.67	25.77	12.23	38.67
10	30	4×4	14×14	23.93	53.83	38.26	71.84
10	90	4×4	100×100	22.90	251.6	217.2	90.55

The compounding position error effect as the interval size grows is still present; however, with a reduced magnitude: the target position error grows consistently from $\sim$3 m to $\sim$275 m as the target interval increases, which is a reduction of 40% and 20%, respectively. For the baseline configuration, GPS error contribution was reduced from 57% to only 14.1% of the total error in the 25 km case and from 52.6% to 16.2% of the total error in the 580 km case. For the symmetric 1 minute interval case at 25 km, the GPS error contribution was reduced from 97.3% to 86.6% of the total error; and, for the 90 minute target interval case at 25 km, the GPS error contribution was reduced from 82.3% to 62.1% of the total error.

Across all cases, the results show that using an appropriate central body gravity model to propagate filtered GPS measurements, the position error can be maintained less than $\sim$275 m for intervals up to 90 minutes and less than $\sim$26 m for intervals up to 10 minutes. This corresponds to 99^{th} percentile angular errors of less than $\sim$1000 μrad at 25 km and less then $\sim$100 μrad at 580 km, which is a 50% or greater improvement from the unfiltered case. Using the Rayleigh approximation for the pointing error and including the other error budget terms in Table 2.2, the 99.7% pointing loss is therefore less than ~ -0.623 dB at 25 km and ~ -0.421 dB at 580 km. The corresponding margins compared to the reference requirement of -1.5 dB are greater than 0.877 dB and 1.079 dB, respectively. This is an improvement of 0.607 dB for the 25 km case and only 0.006 dB for the 580 km case. The reason for the negligible pointing loss improvement in the 580 km case is that the other error budget

terms dominate the pointing error in that case, with the assembly & calibration error being several times larger than the relative navigation error even without filtering. Therefore, for the CLICK terminal, filtering at short ranges has a significant pointing loss improvement of about 49%; however, filtering at long ranges has a negligible impact of only about 1%. As discussed previously, the losses using unfiltered GPS measurements are sufficient for CLICK, so filtering will not be used onboard for the mission, although the results in this section could be verified by post-processing on the ground. Nevertheless, for future missions with potentially narrower beacons, better assembly & calibration error, or significantly worse GPS measurement errors filtering may be more beneficial. For example, if the beacon divergence is halved and the mechanical errors due to assembly, calibration, & launch-shifts are improved by a factor of 10, then the losses at 25 km are improved by filtering from -3.34 dB to -0.892 dB (73.2%), and those at 580 km are improved from -0.108 dB to -0.084 dB (22.2%). Despite this, at long ranges, the unfiltered GPS approach would still have positive margin, so filtering would only be needed for long ranges if the GPS error increased significantly due to significantly poorer receiver performance due to hardware faults.

In summary, with the addition of Kalman filtering, the navigation error can be maintained to less than $\sim$275 m over intervals of 90 minutes and less than $\sim$26 m for intervals less than 10 minutes, with improvements relative to unfiltered results of 19% and 48% respectively. Across all configurations, the 99^{th} percentile angular errors were less than $\sim$1000 μrad at 25 km and less then $\sim$100 μrad at 580 km, corresponding to 99.7% pointing losses less than -0.623 dB at 25 km and -0.421 dB at 580 km and corresponding margins greater than 0.877 dB and 1.079 dB, respectively. This corresponds to improvements of at least 50% for the angular error across all cases and improvements of 49% for the pointing loss at 25 km and about 1% at 580 km. Therefore, for the CLICK hardware configuration, filtering has a significantly greater effect on pointing loss at shorter ranges due to the dominance of error terms other than relative navigation in the 580 km crosslink pointing budget. Nevertheless, for future missions with potentially narrower beacons, improved mechanical errors,

and/or significantly worse GPS measurement errors, filtering may have greater impact at long ranges. Moreover, despite the performance improvement from filtering at short ranges, simply propagating the raw GPS fixes is sufficient to meet the requirements of the CLICK mission, so the application of filtering to relative navigation will not be tested on orbit during the CLICK mission, although post-processing telemetry on the ground could validate the results of this analysis. Nevertheless, the need to continue to reduce SWaP and improve performance could necessitate filtering for future missions.

4.8 Propagation of Kalman Filtered GPS Measurements for LEO Downlinks

Table 4.6 summarizes the results for propagation of Kalman filtered GPS measurements for LEO downlinks. Note that in this case, only the Host GPS measurements were filtered, although even higher performance could be acheived by statistical processing of the ground station GPS measurements as well. This could be done by simply averaging them for fixed ground stations rather than using a Kalman filter. For mobile platforms like vehicles, a filter employing a stochastic dynamic model like a white noise acceleration model could potentially be used, which are typically used in target-tracking scenarios where a physics-based target dynamics model is unavailable [47]. Nevertheless, the performance did improve in all scenarios by filtering even just the Host measurements. For example, with the 1 minute interval and the IAU-00/06 B model, the angular error was reduced by 1.5× from 17.29 μrad to 11.20 μrad. For the 10 minute interval with the IAU-00/06 B model, the angular error was reduced by 1.7× from 32.44 μrad to 18.88 μrad.

As the ground station GPS measurements were not filtered, the Target position errors were left unchanged in this simulation. The overall 99^{th} percentile error across all cases is less than ~35 μrad (improvement of 22.2%), which corresponds to 99.7% pointing losses of less than −0.434 dB with margins greater than 1.066 dB across

Table 4.6: Error magnitudes (99^{th} percentile) for propagation of Kalman filtered GPS measurements for LEO downlink to CONUS for various propagation & ECI-ECEF transform configurations. Reference geodetic coordinates (Latitude, Longitude): Boston (42.360636°, − 71.093418°), Boulder (40.006891°, − 105.264983°), Los Angeles (34.068851°, − 118.444692°).

Δt_H (min)	Host Model	ECI-ECEF Transform	Host Pos. Err. (m)	Target Pos. Err. (m)	Range Err. (m)	Angle Err. (μrad)
1	J_2	4-term X,Y Only	3.657	23.24	19.94	30.74
1	J_2	4-term X,Y & ΔUT1	3.657	16.18	11.22	16.46
1	J_2	15-term X,Y & x_p, y_p, ΔUT1	3.657	14.66	5.926	10.72
1	**J_2**	**IAU-00/06 B & All EOP**	**3.657**	**14.31**	**6.480**	**11.20**
1	J_2	None	3.657	14.93	6.679	11.68
10	4×4	4-term X,Y Only	27.04	24.12	21.16	33.45
10	4×4	4-term X,Y & ΔUT1	27.04	16.03	13.04	22.26
10	4×4	15-term X,Y & x_p, y_p, ΔUT1	27.04	13.69	12.07	19.37
10	4×4	IAU-00/06 B & All EOP	27.04	14.47	12.66	18.88
10	4×4	None	27.04	14.93	12.21	20.95

all cases. As predicted in Chapter 3, the impact on pointing loss from filtering the spacecraft GPS measurements is negligible because the downlink pointing budget is currently dominated by the mechanical error terms. Moreover, even the spacecraft body pointing error is greater than the relative navigation error, so for filtering to be useful for improving downlink pointing losses, not only would the terminal hardware performance need to increase with a narrower beam and better mechanical errors, but the beacon would likely need to be actively pointed with a mirror. This could be the case if the terminal eliminates the additional wide-angle beacon laser and uses a narrow laser for both communications and PAT, which would be beneficial from a terminal design standpoint, as it would reduce the power and volume requirements. Assuming this would be the case for future missions with more stringent requirements, GPS measurement processing could then be useful for performance improvement.

In summary, by filtering the spacecraft GPS measurements, the overall 99^{th} percentile error across all cases was improved by at least 22.2% to less than $\sim$35 μrad, which corresponds to 99.7% pointing losses of less than -0.434 dB with margins greater than 1.066 dB across all cases. This means that, as anticipated from previ-

ous analysis, filtering had a negligible impact on pointing loss for downlink due to the dominance of mechanical and spacecraft errors in the downlink pointing budget. Nevertheless, for future missions with more stringent requirements and higher performance terminal designs, GPS measurement processing could be useful for performance improvement for downlinks as well as crosslinks.

4.9 Chapter 4 Summary

The Extended Kalman Filter (EKF) is used for estimation problems with nonlinear dynamics and/or measurements and can be formulated in continuous time, discrete time, or as a hybrid of both. There are three main steps: filter initialization, correction, and prediction. There are various initialization strategies depending on the available data. For orbit determination analysis, single GPS fixes were used for state initialization, and estimated measurement uncertainties were used for covariance initialization. Three different formulations of the EKF subroutines were explored in depth: 1) the Conventional EKF (CEKF); 2) the Joseph Sequential EKF (JSEKF); 3) the UD Sequential EKF (UDSEKF).

In Section 4.2.1, the Conventional EKF (CEKF) correction algorithm was defined, with a time complexity that includes a $O(m^3)$ term due a matrix inverse step. Two numerical stabilization approaches were given: brute force symmetrization of the covariance matrix and the Joseph form update. Next, in Section 4.2.2, sequential measurement processing was introduced to eliminate the matrix inverse step in the conventional correction. This treats vector measurements as sequences of scalar measurements, enabling the use of a series of scalar division correction steps instead of using matrix inverse. An alternative approach to guarantee numerical stabilization is to take advantage of the Cholesky factorization of the covariance matrix, which was introduced in Section 4.2.3. This led to the Thornton-Bierman UD formulation of the EKF. Moreover, Cholesky factorization formulations save on memory usage by $50(1 - 1/n)\%$.

Section 4.3.1 described some Runge-Kutta methods for solving the state prediction initial value problem (IVP). Differences between methods include the order of the truncation error and the use of either fixed or variable step sizes. The leading complexity terms are $O(N(4np_{\mathbf{g}}(n,r)))$ for RK4, $O(N(6np_{\mathbf{g}}(n,r)))$ for RKF 4(5) & DP 5(4), and $O(N(13np_{\mathbf{g}}(n,r)))$ for RKF 7(8). For a given accuracy, higher-order, variable step methods typically need to take far fewer steps N than lower-order, fixed-step methods, meaning that they are more efficient.

For covariance prediction, Section 4.3.2 showed that the solution to the continuous dynamics Lyapunov matrix differential equation can approximated by the standard discrete time covariance prediction by using the matrix exponential. Section 4.3.2 showed how one of the top performing matrix exponential algorithms is the scaling and squaring Pade approximant method used by MATLAB's **expm**, which has a complexity that is a function of the L_1-norm of the $M \times M$ matrix argument, which in the best case reduces to $O((8/3)M^3)$. Next, Section 4.3.3 showed how the covariance prediction step is modified for the UD factorization via a similar discretization step via the matrix exponential followed by a modified weighted Gram-Schmidt process for UD prediction.

The EKF for orbit determination using GNSS measurements was formulated in Section 4.4 using the minimal state consisting of the ECI position and velocity, a central body gravity model, and GPS position and velocity fixes. The process noise magnitude was estimated via the perturbing acceleration analysis of Section 3.1.1, and the GPS receiver orbit (anti-)normal receiver oriented measurement noise from Section 3.10 was used. The improvement of the problem conditioning via nondimensionalization was also discussed.

Following this, Section 4.5 evaluated the CEKF, JSEKF, and UDSEKF filter formulations on three metrics: efficiency as per analytical time complexity results given previously for each of the subroutines, a statistical hypothesis test for consistency, and 3D-RMS position & velocity estimation errors for orbit determination. The overall ranking was 1) UDSEKF, 2) CEKF, 3) JSEKF. Furthermore, Section 4.6 showed that applying the UDSEKF to sampling intervals (T_s) from 1 second up to 10 minutes yields improvements in the 3D-RMS position and velocity errors of at least $2\times$ relative to unfiltered GPS fixes.

Section 4.7 demonstrated that with the addition of Kalman filtering, the navigation error can be maintained to less than $\sim$275 m over intervals of 90 minutes and less than $\sim$26 m for intervals less than 10 minutes, with improvements relative to unfiltered results of 19% and 48% respectively. Across all configurations, the 99^{th} percentile angular errors were less than $\sim$1000 μrad at 25 km and less then $\sim$100

μrad at 580 km, corresponding to 99.7% pointing losses less than -0.623 dB at 25 km and -0.421 dB at 580 km and corresponding margins greater than 0.877 dB and 1.079 dB, respectively. This corresponded to improvements of at least 50% for the angular error across all cases and improvements of 49% for the pointing loss at 25 km and about 1% at 580 km. Therefore, for the CLICK hardware configuration, filtering has a significantly greater effect on pointing loss at shorter ranges due to the dominance of error terms other than relative navigation in the CLICK 580 km crosslink pointing budget. Nevertheless, for future missions with potentially narrower beacons, improved mechanical errors, and/or significantly worse GPS measurement errors, filtering may have greater impact at long ranges.

Finally, Section 4.8 applied filtering to the spacecraft GPS measurements for downlinks, which led to the improvement of the overall 99^{th} percentile error across all cases by at least 22.2% to less than $\sim$35 μrad. This corresponds to 99.7% pointing losses of less than -0.434 dB with margins greater than 1.066 dB across all cases. As anticipated from previous analysis, filtering had a negligible impact on pointing loss for downlink due to the dominance of mechanical and spacecraft errors in the CLICK downlink pointing budget. Nevertheless, for future missions with more stringent requirements and higher performance terminal designs, GPS measurement processing could be useful for performance improvement for downlinks as well as crosslinks.

Chapter 5

Conclusion

5.1 Thesis Summary

Chapter 1

The SWaP efficiency of laser communications make it a good fite for development in concert with rising interest in small satellite mission concepts. Nanosatellite LEO to ground downlinks have been demonstrated and improved performance is expected with furture downlink demonstrations. The CLICK B/C mission has the objective of demonstrating the first nanosatellite crosslink. This mission was the catalyst for this thesis research and will be referenced throughout as a motivating example and case study in nanosatellite laser communications.

The need for precise and accurate pointing with laser instruments motivates a formalized, systematic approach to fulfilling this need called Pointing, Acquisition, and Tracking (PAT). The PAT process for the CLICK crosslink begins with relative navigation information derived from the GPS measurements aboard both satellites provides the initial pointing information for beacon acquisition on the camera. The camera data is used for feedback to refine the body pointing followed by a fine pointing process using the terminal's fast steering mirror. Throughout the 10 minute communications link, the coarse spacecraft tracking and fine steering mirror tracking processes continue to maintain the link. The downlink PAT process begins with a

similar relative navigation process, although the ground station target position is estimated using an earth rotation model and stored coordinates. The navigation solution is used throughout for body pointing, and the ground station's beacon is used only for fine pointing. The focus of this thesis is the initial pointing process for these LEO crosslinks and downlinks using GPS-based relative navigation.

Chapter 2

First, the Gaussian beam intensity along with the $1/e^2$ & FWHM beam divergences were defined. Next, the laser communications range equation was presented, leading into derivations for the Rice/Rician model of the total pointing error and the non-central chi-squared model of the pointing loss. The pointing error models were applied to find model parameters for the baseline CLICK configuration relative navigation error and for the point ahead error for crosslinks and downlinks. The crosslink point ahead errors increased as a power law of the range, and the downlink point-ahead errors were similar across LEO orbits and CONUS ground stations.

Next, the baseline pointing budgets for crosslink relative navigation based body pointing were given for the CLICK minimum & maximum ranges of 25 & 580 km. The 99^{th} percentile angular relative navigation errors were 1367 μrad & 76.58 μrad for the 25 km and 580 km cases, respectively. The corresponding 99.7% pointing losses were -0.278 dB & -0.182 dB, with margins of 1.222 dB & 1.318 dB relative to the -1.5 dB required worst case pointing loss bound. The pointing budget for relative navigation based body pointing for the CLICK B/C downlink was then given, which had a 99^{th} percentile angular relative navigation error of 17.29 μrad and a corresponding 99.7% pointing loss of -0.189 dB with a margin of 1.311 dB compared to the -1.5 dB requirement.

The crosslink access duration was analyzed based on solar keep out constraints between 20° & 75° for near-circular LEO orbits. The CLICK keep out constraint of 45° to 50° corresponded to an access duration of at least 21 minutes for 99% of cases, which meets the mission requirement of 15 minutes. The median LEO downlink durations to CONUS ground stations were between 9.38 & 13.55 minutes for perigee

altitudes between 400 & 600 km and zero minimum ground station elevation angle. The median minimum downlink ranges were between 995.9 km and 1630 km, with the mid-range ISS inclination of 51.6° having the minimum ranges.

Chapter 3

This chapter first analyzed the state propagation algorithm in depth, followed by a discussion on how GPS position & velocity fixes are generated and their noise properties, before finally combining these two ideas to estimate the relative navigation error by directly propagating GPS fixes, which is the baseline configuration for CLICK. Cowell's method is used in this work for LEO propagation, which numerically integrates a two-body gravitational acceleration plus a perturbation acceleration computed via the sum of additional forces that can generally include aspherical Earth gravity terms, atmospheric drag, solar radiation pressure, third body perturbations, tides, earth radiation pressure, relativistic effects, and thrusting maneuvers. The magnitudes of these perturbing accelerations were compared, and a sequence of force model simplifications for comparison was determined prior to position propagation accuracy analysis. To achieve a position propagation accuracy of ~ 25 m for crosslinks, the simplified models chosen were J_2 for $\Delta t = 1$ minute, 4×4 for $\Delta t = 10$ minutes, 14×14 for $\Delta t = 30$ minutes, and 100×100 for $\Delta t = 90$ minutes. The same respective models are chosen for the 1 & 10 minute intervals used for downlink. Using only the appropriate central body gravity model, model-induced propagation error was maintained less than 50 m for intervals up to 90 minutes and less than 25 m for intervals up to 30 minutes. This corresponded to 99^{th} percentile angular errors of less than 600 μrad at 25 km and less then 40 μrad at 580 km.

Prior to relative navigation analysis for downlinks, ECI-ECEF transformations were discussed, and the position errors incurred by using simplified models with reduced computational costs were compared for CONUS ground station locations. Even with the simplest 4-term X, Y series without EOPs, position error remained less than 16 m. These models were compared for relative navigation in combination with the orbit propagation models. All cases had a 99^{th} percentile model-induced error of less

than 32 μrad, which is on the order of the point-ahead error (50.36 μrad).

Proceeding to the incorporation of GPS error, the position and velocity uncertainties were derived as a function of the DOP parameters and the URE & URRE. For this analysis, the specified spacecraft GPS receiver was determined to have σ_{URE} = 0.83 m and σ_{URRE} = 0.005 m/s. For a LEO satellite, it was found that the cross-track DOP increased as the antenna is oriented away from the radial direction, with a 1.4$\times$ increase in PDOP for (anti-)normal pointing relative to radial pointing. For the purposes of further analysis, the worst case (anti-)normal pointing was assumed, with a PDOP of 8.11, corresponding 3D RMS position error of 6.75 m, and 3D RMS velocity error of 0.040 m/s. The optical ground station is also equipped with GPS receiver with different parameters: σ_{URE} = 1.21 m, PDOP = 5.36, and a 3D-RMS position error of 6.48 m.

The relative navigation error for crosslinks was analyzed by combining orbit propagation with raw GPS fixes. The navigation error was maintained to less than $\sim$340 m over intervals of 90 minutes and less than $\sim$50 m for intervals less than 10 minutes. Across all configurations, the 99$^{\text{th}}$ percentile angular errors were less than $\sim$2000 μrad at 25 km and less then $\sim$200 μrad at 580 km, corresponding to 99.7% pointing losses less than -1.235 dB at 25 km and -0.427 dB at 580 km and corresponding margins greater than 0.265 dB and 1.073 dB, respectively. Therefore, given sufficient force modeling for intervals up to 90 minutes, unprocessed GPS measurements can be used with the CLICK hardware, and sufficient pointing accuracy can be maintained, which is the plan for CLICK.

Similar analysis was carried out for downlinks, and the 99$^{\text{th}}$ percentile error across all cases was less than $\sim$45 μrad, which corresponds to 99.7% pointing losses of less than -0.434 dB with margins greater than 1.066 dB across all cases. This means that the pointing requirement is met for any of the relative navigation configurations analyzed, and computational cost savings can be had by simplifying the Earth rotation model to a 4-term X, Y series without EOPs.

Chapter 4

The Extended Kalman Filter (EKF) is used for estimation problems with nonlinear dynamics and/or measurements. There are three main steps: filter initialization, correction, and prediction. There are various initialization strategies depending on the available data. For orbit determination analysis, single GPS fixes were used for state initialization, and estimated measurement uncertainties were used for covariance initialization. Three different formulations of the correction and prediction subroutines were explored in depth: 1) the Conventional EKF (CEKF); 2) the Joseph Sequential EKF (JSEKF); 3) the UD Sequential EKF (UDSEKF).

The CEKF correction algorithm was defined, which has a time complexity that includes a $O(m^3)$ term due a matrix inverse step. Two numerical stabilization approaches were given: brute force symmetrization of the covariance matrix and the Joseph form update. Next, sequential measurement processing was introduced to eliminate the matrix inverse step in the conventional correction, which led to the JSEKF formulation. An alternative approach to guarantee numerical stabilization is to take advantage of the UDU^T Cholesky factorization of the covariance matrix, which led to the UDSEKF formulation. Moreover, Cholesky factorization formulations save on memory usage by $50(1 - 1/n)\%$.

The state prediction initial value problem (IVP) can be solved by Runge-Kutta methods. Differences between these methods include the order of the truncation error and the use of either fixed or variable step sizes. For a given accuracy, higher-order, variable step methods typically need to take far fewer steps than lower-order, fixed-step methods, meaning that they are more efficient.

For covariance prediction, the solution to the continuous dynamics Lyapunov matrix differential equation can approximated by the standard discrete time covariance prediction by using the matrix exponential. One of the top performing matrix exponential algorithms is the scaling and squaring Pade approximant method used by MATLAB's expm, which has a complexity that is a function of the L_1-norm of the $M \times M$ matrix argument, which in the best case reduces to $O((8/3)M^3)$. For the

UDSEKF, the covariance prediction step is modified via a similar matrix exponential discretization step via followed by a modified weighted Gram-Schmidt process.

The EKF for orbit determination using GNSS measurements was formulated using the minimal state consisting of the ECI position and velocity, a central body gravity model, GPS position and velocity fixes, and nondimensionalization. The process noise magnitude was estimated via perturbing acceleration analysis, and the GPS receiver orbit (anti-)normal receiver oriented measurement noise was used.

The CEKF, JSEKF, and UDSEKF filter formulations were evaluated on three metrics: efficiency as per analytical time complexity results given previously for each of the subroutines, a statistical hypothesis test for consistency, and 3D-RMS position & velocity estimation errors for orbit determination. The overall ranking was 1) UDSEKF, 2) CEKF, 3) JSEKF. Applying the UDSEKF to sampling intervals (T_s) from 1 second up to 10 minutes yields improvements in the 3D-RMS position and velocity errors of at least $2\times$ relative to unfiltered GPS fixes.

Moreover, with the addition of Kalman filtering, the navigation error can be maintained to less than $\sim$275 m over intervals of 90 minutes and less than $\sim$26 m for intervals less than 10 minutes, with improvements relative to unfiltered results of 19% and 48% respectively. Across all configurations, the 99^{th} percentile angular errors were less than $\sim$1000 μrad at 25 km and less then $\sim$100 μrad at 580 km, corresponding to 99.7% pointing losses less than -0.623 dB at 25 km and -0.421 dB at 580 km and corresponding margins greater than 0.877 dB and 1.079 dB, respectively. This corresponded to improvements of at least 50% for the angular error across all cases and improvements of 49% for the pointing loss at 25 km and about 1% at 580 km. Therefore, for the CLICK hardware configuration, filtering has a significantly greater effect on pointing loss at shorter ranges due to the dominance of error terms other than relative navigation in the CLICK 580 km crosslink pointing budget. Nevertheless, for future missions with potentially narrower beacons, improved mechanical errors, and/or significantly worse GPS measurement errors, filtering may have greater impact at long ranges.

Applying filtering to the spacecraft GPS measurements for downlinks led to the

improvement of the overall 99^{th} percentile error across all cases by at least 22.2% to less than $\sim$35 μrad. This corresponds to 99.7% pointing losses of less than -0.434 dB with margins greater than 1.066 dB across all cases. As anticipated from previous analysis, filtering had a negligible impact on pointing loss for downlink due to the dominance of mechanical and spacecraft errors in the CLICK downlink pointing budget. Nevertheless, for future missions with more stringent requirements and higher performance terminal designs, GPS measurement processing could be useful for performance improvement for downlinks as well as crosslinks.

5.2 Thesis Contributions

- Detailed review of laser communications missions including the CubeSat Laser Infrared CrosslinK (CLICK) mission to demonstrate the first LEO nanosatellite laser communications crosslink as well as downlinks.
- Derivations of Rice statistical model lasercom pointing error and non-central chi-squared model for pointing loss. Simulated model parameters for relative navigation and point ahead errors.
- Pointing budgets for initial relative navigation PAT stages of CLICK crosslinks and downlinks.
- CLICK LEO crosslink access analysis based on solar keep-out constraints and LEO-to-CONUS downlink access analysis based on overpass duration and ranges.
- Recommendations for Cowell propagation force models for LEO satellites with propagation intervals from 1 to 90 minutes.
- Cowell propagation error analysis for relative navigation in LEO for crosslinks and downlinks in addition to recommendations for Earth rotation model simplifications for downlinks.
- GPS error analysis for LEO satellites and CONUS ground stations including review of contemporary hardware and DOP simulations.

- Relative navigation simulations for LEO crosslinks and downlinks using Cowell propagation of raw GPS position and velocity fixes, which is the CLICK baseline. Demonstrated that this CLICK baseline relative navigation configuration meets its pointing requirements. Recommendations for force models and Earth rotation models for alternative relative navigation configurations.

- Review of EKF algorithms for orbit determination using GNSS measurements. Detailed discussion and comparison of three different formulations: CEKF, JSEKF, UDSEKF. Detailed time complexity results for all three formulations in addition to consistency and orbit determination accuracy results. UDSEKF is recommended as the best performer of the three for application to orbit determination.

- Relative navigation simulations for LEO crosslinks and downlinks using Cowell propagation of Kalman filtered GPS fixes. Confirmation of CLICK baseline configuration and recommendations for future missions.

5.3 Future Work

- Verification of the results of chapters 3 & 4 with Ground and on-orbit test results for the CLICK mission.

- Further analysis of propagation approaches for intervals longer than 90 minutes that could be encountered when using ground stations to relay satellite ephemeris information for crosslinks.

- Hardware testing for verification of the URE, URRE, and DOP results for the GPS receiver hardware discussed in Chapter 3.

- Take advantage of the lower block triangular, Hamiltonian structure of matrix arguments to the matrix exponential to reduce the computational cost of the covariance update algorithms described in chapter 4.

- Extend results in chapters 3 & 4 to other link types between and among other orbits including LEO, MEO, & GEO. Note that it is still possible to use GNSS signals in MEO and GEO by directly filtering the psuedorange measurements.

- Extend results in chapter 4 with auxiliary state parameters for Gauss-Markov position noise in GPS measurements, estimating drag to incorporate drag into the dynamics model, and/or out-of-sequence measurements.

- Extend results in chapter 4 using other nonlinear estimation methods: Unscented Kalman Filtering (UKF), particle filtering (PF), or ensemble Kalman filtering (EnKF).

- Relative position measurements have been shown to be sufficient to estimate the absolute orbit of a spacecraft for most orbits due to asymmetries in the dynamic models [81]. Application of this method would enable autonomous navigation for groups of satellites equipped with lasercom terminals in GEO, deep space, and in GNSS-denied situations in LEO & MEO. It would be beneficial to leverage the types of analysis in this work to extend previous results [82] on GNSS-independent navigation using range and/or angles measurements from laser communications crosslinks.

Appendix A

Appendices

A.1 Background on Lasercom PAT Hardware

This section gives a brief introduction to the hardware used in lasercom terminals for PAT. The most common form of large field of regard (FOR) or coarse beam pointing used in ground systems and aboard large satellites are two-axis gimbals, which can provide greater than hemispherical (2π sr) coverage. To the author's knowledge as of this writing, gimballed optical terminal technology, which is essentially based around reflecting ground telescope designs, currently does not exist that can fullfill the SWaP requirements of a nanosatellite such as a 3U or 6U CubeSat. Therefore, the nanosatellite laser communications payloads cited in Table 1.1 (e.g. OCSD, TBIRD, CLICK) all use terminals that are fixed with respect to the spacecraft structure. One of the resulting beam actuation concepts for PAT is static beam body pointing. This is the concept used by TBIRD, OCSD A, B, & C, VSOTA, and OSIRIS. The spacecraft bus uses its onboard attitude determination and control system (ADCS) to achieve the beam pointing requirements of the terminal.

Although nanosatellite ADCS has improved dramatically in recent years [31], the addition of fine (or Vernier) beam steering stages can improve pointing performance well beyond the state of the art in ADCS and/or relax the requirements levied upon the ADCS. There are additional benefits to further steering stages that terminals deployed on large spacecraft take advantage of to help achieve microradian-level point-

ing. One, beam steering can be used to actively compensate for structural vibrations induced by ADCS that include reaction wheels. Two, for sufficiently high relative velocities, a pointing control system is subject to point-ahead error, as described in Section 2.4.2. This error can be on the order of tens of microradians for links between satellites in different orbital planes or between terminals at significantly different altitudes, including space-ground links (see results in Section 2.4.2). A beam steering stage called a Point-Ahead Mirror (PAM) is used to compensate for this error, typically in open-loop, via ephemeris tracking software [3]. There are several approaches to Vernier beam steering. Fine (or fast) steering mirror (FSM) devices include single-axis galvonometer devices, two-axis voice coil devices, piezo-electric devices, Micro-Electro-Mechanical system (MEMS) actuators [3]. There are also nonreflective approaches that include nematic liquid crystals, acousto-optic beam deflectors, tunable liquid lenses, and phased-array emitters [3, 83]. Fine steering mirror devices are the most mature technology as of this writing. The CLICK A & B/C payloads are the only nanosatellite lasercom terminals known to the author that use fine beam steering. They take advantage of a low-SWaP Mirrorcle MEMS fine steering mirror to accomplish this within the constraints of a 1.2U and 1.5U terminal, respectively.

Closed-loop optical feedback for fine pointing or body pointing requires accurate beam position detection sensors, which also come in several forms. The laser wavelength drives the sensor material selection, with design wavelengths below about 1000 nm using silicon devices and design wavelengths above this using InGaAs or InGaAsP devices [3]. The fundamental detector components include p-intrinsic (PIN) photodiodes, avalanche photodiodes (APDs), charge-coupled devices (CCDs), and charge injection devices (CIDs) (which include Complementary Metal-Oxide Semiconductor (CMOS) detectors) [3]. Single photodiode devices can be used for communications receivers. Arrays of photodiodes, the most common of which is the 2 x 2 quadrant photodiode, can be used for acquisition, tracking, and/or communication. CCDs and CIDs can be used for acquisition and/or tracking and are commonly found in cameras, which can have thousands to millions of sensors to form each picture element (pixel). Due to the higher sensor density of CCDs and CIDs compared to photodiodes, these

types of devices can have higher spatial resolution and reduced background noise per sensor element, which is useful for wide field of view (WFOV) acquisition sensors that naturally receive more background optical noise than narrow FOV tracking or communication sensors [3]. In deep space applications, lasercom terminal cameras can have a dual-use to gather attitude information by imaging celestial targets like stars or the Earth (e.g. function as a star tracker or Earth sensor).

Like optical sensors, different optical sources can fulfill the roles of acquisition, tracking, communications, or a combination of the three. Optical sources that only fulfill PAT roles are called beacons and are typically operated at a different wavelength than the communications source to enable spectral isolation of the communications and tracking paths to avoid self-jamming [3]. Other forms of isolation include timing and polarization [3]. To fulfill an acquisition role, the beacon source typically has a larger beam divergence angle to cover a larger initial uncertainty area. The beam may also be scanned over the initial uncertainty area via coarse and/or fine beam steering. Also like sensors, there are multiple types of lasers depending on the desired wavelength, power, and modulation characteristics. The most common laser sources used for communications in free-space is semiconductor InGaAsP 1550 nm [2]. Other semiconductor sources include GaAlAs 780-890 nm, InGaAs 890-980 nm, and InGaAsP 1300 nm can be used [3]. Solid state sources include neodymium yttrium aluminum garnet (Nd:YAG) 1064 nm, neodymium lithium flouride (Nd:YLF) 1047 or 1053 nm, and neodymium yttrium aluminum phosphate (Nd:YAP) 1080 nm.

A.2 Gain and Pointing Loss of a Gaussian Beam

The range equation models the on-axis intensity as an equivalent isotropic source with the equivalent isotropic on-axis intensity given by [84]:

$$F_{iso} = \frac{P_{\mathrm{Tx}} G_{\mathrm{Tx}}}{4\pi z^2} \tag{A.1}$$

Setting $F_{iso} = I(0,z)$, we can solve for G_{Tx}. To simplify equation 2.1a at inter-satellite link ranges, we assume $z >> z_0$. For example, the Rayleigh range (z_0) of a 70.8μrad FWHM, 1550nm laser communications beam is 13.7cm. A series approximation for the beam radius can be made [25]:

$$\left(\frac{w_0}{w(z)}\right)^2 = \frac{1}{1+(z/z_0)^2} = \left(\frac{z_0}{z}\right)^2 + O\left(\left(\frac{z_0}{z}\right)^4\right) \tag{A.2a}$$

$$I(r,z) \approx I_0 \left(\frac{z_0}{z}\right)^2 \exp\left(-2\left(\frac{z_0}{w_0}\frac{r}{z}\right)^2\right) \tag{A.2b}$$

Therefore, making substitutions for z_0 and I_0,

$$I(0,z) = \frac{P_{\text{Tx}}}{4\pi z^2}\frac{8\pi w_0^2}{\lambda^2} \tag{A.3a}$$

$$G_{\text{Tx}} = \frac{8\pi w_0^2}{\lambda^2} = \frac{32}{\theta_{1/e^2}^2} \tag{A.3b}$$

The pointing loss accounts for the off-axis intensity term:

$$L_{ptg}(r,z) \equiv \exp\left(-2\left(\frac{z_0}{w_0}\frac{r}{z}\right)^2\right) \tag{A.4}$$

The substitution of the spherical-polar angle θ via the paraxial (small-angle) relation $r = z\theta$, re-parameterizes this equation in terms of the off-axis pointing angle. Furthermore, substitutions can be made that substitute the divergence angle for the beam waist and Rayleigh range using equations 2.1c and 2.1d:

$$L_{ptg}(\theta) = \exp\left(-2\left(\frac{\pi w_0}{\lambda}\theta\right)^2\right) \tag{A.5a}$$

$$= \exp\left(-8\left(\theta/\theta_{1/e^2}\right)^2\right) \tag{A.5b}$$

A.3 The Gaussian Distribution on the Sphere

In Chapter 2, the random pointing vector is described by its azimuth and elevation angles, Θ_x & Θ_y, respectively. Where $\Theta_x \sim N(\mu_x, \sigma_x)$ & $\Theta_y \sim N(\mu_y, \sigma_y)$. It may

be observed that the domains of these angles are finite, with $\Theta_x \in (-\pi, \pi]$ & $\Theta_y \in [-\pi/2, \pi/2]$, in apparent contradiction of the infinite domain of the standard normal distribution. What will be seen here is that the infinite domain normal distribution closely approximates the bounded domain case, and is mathematically simpler to work with, hence its use. A truncated Gaussian distribution can be described in general for the bounded random variable $X \in (a, b)$ using the CDF and PDF shown in the equations below [29]:

$$\mathrm{F_X}(x) = 0, \ x \leq a \tag{A.6a}$$

$$\mathrm{F_X}(x) = \frac{\Phi(x) - \Phi(a)}{\Phi(b) - \Phi(a)}, \ x \in (a, b] \tag{A.6b}$$

$$\mathrm{F_X}(x) = 1, \ x > b \tag{A.6c}$$

$$\mathrm{f}(x) = \frac{1}{\sqrt{2\pi}\sigma(\Phi(b) - \Phi(a))} \exp\left(-\frac{(x-\mu)^2}{2\sigma^2}\right), \ x \in (a, b] \tag{A.6d}$$

$$\mathrm{f}(x) = 0, \ x \leq a, \ x > b \tag{A.6e}$$

$$\text{with } \Phi(x) = \frac{1}{2}\mathrm{erfc}\left(\frac{\mu - x}{\sqrt{2}\sigma}\right) \tag{A.6f}$$

In the case of azimuth, $\Theta_x \in (\mu - \pi, \mu + \pi]$, where the bound has been shifted to be centered around the mean to avoid main lobe truncation in the case of large μ. Similarly, for elevation $\Theta_y \in [\mu - \pi/2, \mu + \pi/2]$. In practice, $|\mu| + 3\sigma << \pi/2$ (typically a few degrees, $\mathrm{O}(10^{-1})$ mrad, in the worst cases), which means that the problem of main lobe truncation would not be likely encountered regardless. More importantly, for these practical so-called small-angle or paraxial cases, the truncated distribution is well approximated by an infinite domain normal distribution with significant deviation only arising when $|\mu| + 3\sigma$ is on the order of the bound, which in this case is either π in the case of azimuth or $\pi/2$ in the case of elevation.

A.4 The Rayleigh Pointing Error & Loss Model

A distribution that is closely related to the Rice distribution is called the Rayleigh distribution, which is equivalent to a zero-bias Rice distribution: $\mathrm{Rice}(0, \sigma) = \mathrm{Rayleigh}(\sigma)$.

It is also important to note the following approximate relationship for $\nu/\sigma << 1$ [29]:

$$1 - \mathrm{Q}_1\left(\frac{\nu}{\sigma}, \frac{\theta}{\sigma}\right) = 1 - \exp\left(-\frac{\theta^2}{2\sigma^2}\right) + O\left(\left(\frac{\nu}{\sigma}\right)^2\right) \tag{A.7}$$

which means that for small bias relative to variance, the distribution is well-approximated by a Rayleigh distribution, which has CDF and PDF as follows [29]:

$$\mathrm{P}[\Theta \leq \theta] = 1 - \exp\left(-\frac{\theta^2}{2\sigma^2}\right) \tag{A.8a}$$

$$p_\Theta(\theta) = \frac{\theta}{\sigma^2}\exp\left(-\frac{\theta^2}{2\sigma^2}\right) \tag{A.8b}$$

The negative of the pointing loss in decibels is

$$\tilde{L}_{\mathrm{ptg,dB}} = -L_{\mathrm{ptg,dB}} = 80\mathrm{Log}_{10}(e)\left(\frac{\Theta}{\theta_{1/e^2}}\right)^2 \tag{A.9}$$

Taking the error angle Θ to be Rayleigh distributed results in an exponentially distributed pointing loss.

$$\Theta \sim \text{Rayleigh}(\sigma) \implies \tilde{L}_{\mathrm{ptg,dB}} \sim \text{Exponential}\left(\frac{1}{160\mathrm{Log}_{10}(e)}\frac{\theta_{1/e^2}^2}{\sigma^2}\right) \tag{A.10}$$

with the CDF

$$\mathrm{P}[\tilde{L}_{\mathrm{ptg,dB}} \leq \tilde{l}] = p_l = 1 - 10^{\frac{-\tilde{l}\theta_{1/e^2}^2}{160\sigma^2}} \tag{A.11}$$

The pointing loss percentile can therefore be expressed as follows for a given reliability level, expressed either as a general probability p_l or as a number of nines e.g. 3 nines is $p_l = 0.999$.

$$l = -\tilde{l} = \frac{160\sigma^2}{\theta_{1/e^2}^2}\mathrm{Log}_{10}(1 - p_l) = -\frac{160\sigma^2}{\theta_{1/e^2}^2}n_9 \tag{A.12}$$

Re-arranging this expression gives the standard deviation of the pointing error needed for a given loss, reliability level, and beam divergence.

$$\sigma = \theta_{1/e^2}\sqrt{\frac{|l|}{160n_9}} = \theta_{\mathrm{HWHM}}\sqrt{\frac{|l|}{20n_9\ln(2)}} \tag{A.13}$$

A.5 Background on PAT Sequences

In a simplex link from a transmitting terminal to a receiving terminal, the acquisition is achieved when the receiver terminal detects the transmitter terminal's signal and is able to lock on to its location. There are two criteria to be met: one, the transmitted signal is within the field of view of the receiver sensor; two, the transmitter is pointing its beam with sufficiently small angular deviation from the line of sight between the two terminals for the link to close.

There are two basic approaches to achieving these criteria, classified by Casey et al. as staring or scanning [3]. Staring the terminals means estimating the pointing direction of the target and pointing the receiver field of view or the laser beam at it: the target is the centroid of the uncertainty region, which is the pair of estimated mean pointing angles. Given sufficiently accurate pointing knowledge, the uncertainty region will be sufficiently enclosed within the pointing requirements of the receiver FOV and the transmitter beam, and the two criteria will be met with sufficiently high reliability. For instance, if the 95th percentile uncertainty region is within both requirements, the link will have an acquisition reliability of $0.95^2 = 90.25\%$, assuming each pointing task is an independent random variable. This type of acquisition is classed by by Casey et al. as stare-stare [3].

For a duplex link, what changes is the pointing requirement on each terminal. Typically, the laser beam has a narrower pointing requirement than the receiver field of view. This means that while for a simplex link, the pair of requirements is receiver FOV and laser beam; for a duplex link, the pair of requirements is given by each laser beam, with the FOV requirement being met by the beam requirement (given a co-aligned terminal beam and receiver design).

Scanning can be thought of as supplementary to staring, with the scan beginning at the best target estimate location and proceeding in a spiral or raster pattern from there out to a radius sufficient to encompass the uncertainty region to the desired reliability. Either the receiver and/or the transmitter may scan depending on the requirements of each. An example scanning operational approach is classed by Casey

et al. as scan-stare: the receiver stares in the estimated target direction, and the transmitter scans its beam over the uncertainty region of the receiver. When the receiver detects the transmitter beam, it responds with its own laser transmitter (this scanning approach requires a duplex link) by pointing it in the direction of the received signal. The transmitter then detects the response signal and narrows its scan onto the newly updated target direction. When this process converges, the terminals continue into tracking operations. The time of acquisition in any scan is directly related to the size of the uncertainty region, with smaller uncertainty regions corresponding to faster acquisitions. Hence, even for the scanned approach, the prior pointing knowledge is an important element of system performance.

Stages 1 and 2 of PAT for the CLICK B/C crosslink design are referred to "coarse" and "fine", respectively. As this is a two stage system, there are generally four phases of PAT operations: coarse acquisition, coarse tracking, fine acquisition, and fine tracking. Further details on the optical design and fine pointing design can be found in [7, 20, 21, 24]. Coarse acquisition is a stare-stare approach, which uses the beacon laser and beacon camera elements. Both the beacon laser and receiver are fixed with respect to the spacecraft and are actuated via the spacecraft body pointing capability realized by its attitude determination and control system (ADCS). The prior pointing knowledge that each spacecraft uses to estimate the target direction is provided via orbit determination of the target and host spacecraft using position and velocity measurements taken by each spacecraft's onboard Global Navigation Satellite System (GNSS) receiver. The orbit epoch information (time and orbital elements) is then transferred to the other spacecraft over a radio crosslink. Upon receipt, the orbit epoch is propagated and used to generate an attitude command (or command sequence) for the ADCS, which re-orients the spacecraft in the direction of the target attitude (and attitude rate). The beacon FWHM beamwidth is 0.75 degrees, and the camera FOV is 10 degrees. They are co-aligned such that the factor determining acquisition is the beacon beamwidth.

The fine steering mirror (FSM) actuates the incoming and outgoing beam, at the same time actuating FOV cone of the quadcell to co-align the transmitted signal with

the received signal. The signal received by the quadcell is the beacon signal, which is already being received by the camera from the previous step. The static FOV of the quadcell is 0.36°. If the signal is not being immediately received by the quadcell, the FSM can adjust based on the camera signal and then spiral scan from there if necessary. The FOR of the quadcell is limited by the max steering angle of the FSM, which is +/- 2 degree optical in each axis, corresponding to +/- 0.19 degrees outside the telescope. This leads to a quadcell FOR of 0.74°. Once the beacon is acquired on the quadcell, fine tracking can commence.

A.6 Additional CLICK B/C Pointing Budgets

A.6.1 Body Pointing Feedback for Crosslinks

Once the beacon signal is acquired, tracking begins where the beacon camera is used to correct the spacecraft attitude as well as provide a priori information for acquisition of the fine stage. The contributions to beacon tracking error are similar to acquisition and include pointing direction measurement error from the camera composed of the noise equivalent angle (NEA) and the calibration of the imaging process for feedback, body pointing jitter and attitude control error, point ahead error, and a the residual error from measuring the misalignment of the optical axes of the beacon laser and the camera lens. Further details on assembly & calibration can be found in [24, 30]. The body pointing is the same as previously discussed. The NEA is computed from link budget analysis using a model of the beacon camera sensor. The camera feedback calibration residual is based on hardware test results using a checkerboard reference object to calibrate the beacon camera. These are combined in the pointing budget given in Table A.1. The beacon pointing requirement of -1.5 dB is met with margin of 1.48 dB.

Table A.1: Pointing error budget for body pointing of crosslink beacon laser with optical feedback from a monocular camera.

Budget Element	25 km range		580 km range	
	μ (μrad)	σ (μrad)	μ (μrad)	σ (μrad)
Point Ahead	0.126	0.001	2.911	0.031
Assembly & Calibration	0.000	80.80	0.000	80.80
Camera Feedback Calibration	0.000	3.26	0.000	3.26
Camera Feedback NEA	0.000	69.13	0.000	69.13
Spacecraft Body Pointing	0.000	87.42	0.000	87.42
Total	0.126	137.7	2.911	137.7
θ_{1/e^2} (μrad)	22235			
θ_{ptg} (μrad, $p_\theta = 0.997$)	469.3		469.5	
$L_{\text{ptg,dB}}$ (dB, $p_l = 0.997$)	-0.0155		-0.0155	

A.6.2 Fine Pointing

The contributors to fine acquisition error are pointing direction measurement error, point ahead error, FSM pointing error, FSM-to-camera calibration error, sensor jitter, and mechanical misalignments in the quadcell optical train. The pointing direction measurement error is the same as that in coarse tracking. The FSM pointing error is a result of open-loop control instabilility. The FSM-to-camera calibration error is a the residual error in the calibration between the FSM actuation command and the pointing direction measurement, which is done on the ground. The sensor jitter is the same as the beam jitter from before; however, now the structural vibrations affect the sensor. The mechanical misalignments are similarly generated as before: residual calibration error, launch shifts, and on-orbit thermoelastic deformation. Additional details on mechanical and thermoelastic errors can be found in [24, 30]. The Reaction Wheel (RW) jitter value is based on flight results for the ASTERIA Cubesat [85]. The FSM control residual is based on optical bench hardware test results [7]. The quadcell NEA value is based on Zemax analysis, and further details can be found in [30]. Combining these results, the pointing budgets for fine pointing for crosslinks and downlinks are given in Tables A.2 and A.3.

Table A.2: Fine pointing error budget for the transmit communications laser for LEO crosslinks.

Budget Element	25 km range		580 km range	
	μ (μrad)	σ (μrad)	μ (μrad)	σ (μrad)
Point Ahead	0.126	0.001	2.911	0.031
Optical Calibration	0.00	4.47	0.00	4.47
Thermoelastic	0.00	5.40	0.00	5.40
RW Jitter	0.00	1.62	0.00	1.62
FSM Control Residual	0.00	3.33	0.00	3.33
Quadcell NEA	0.00	1.83	0.00	1.83
Total	0.126	8.14	2.911	8.14
θ_{1/e^2} (μrad)	120.96			
θ_{ptg} (μrad, $p_\theta = 0.997$)	27.7		29.3	
$L_{\text{ptg,dB}}$ (dB, $p_l = 0.997$)	-1.83		-2.04	

The fine pointing crosslink requirement of -3 dB is met with margins of 1.17 dB and 0.96 dB for ranges of 25 km and 580 km, respectively. For downlink fine pointing,

Table A.3: Fine pointing error budget for the transmit communications laser for LEO downlink.

Budget Element	μ (μrad)	σ (μrad)
Point Ahead	24.48	9.86
Optical Calibration	0.00	4.47
Thermoelastic	0.00	5.40
RW Jitter	0.00	1.62
FSM Control Residual	0.00	3.33
Quadcell NEA	0.00	1.83
Total	24.48	12.78
θ_{1/e^2} (μrad)	120.96	
θ_{ptg} (μrad, $p_\theta = 0.997$)	71.4	
$L_{\text{ptg,dB}}$ (dB, $p_l = 0.997$)	-12.1	

a point-ahead mirror was not included in the design to meet volume requirements; therefore, the point-ahead error dominates the loss, leading to a 99.7% pointing loss of -12.1 dB. Although this is significantly more than all other pointing budgets, link budget analysis has shown that the receiver gain of the 30 cm aperture optical ground station is sufficiently high to enable to link to close with sufficient margin and for sufficient durations to complete the 10 Mbps science data collection needs (necessary link duration less than 1 minute). For future terminal designs, a point ahead mirror is recommended to improve downlink communications performance.

A.7 Time Systems

All rotations are dependent on the current time, which makes timing knowledge essential for accurate transformations. Accurate timing can be maintained via periodic corrections of a local clock, which is subject to bias errors, using GPS measurements. There are several relevant time systems: Universal Time (UT) in the UT1 variant (there are also UT0 and UT2 variants of UT), Coordinated Universal Time (UTC), International Atomic Time (TAI), and Terrestrial (Dynamical) Time (TT). These are

related as follows [33].

$$\text{UT1} = \text{UTC} + \Delta\text{UT1} \tag{A.14a}$$

$$\text{TAI} = \text{UTC} + \Delta\text{AT} = \text{GPS} + 19\text{s} \tag{A.14b}$$

$$\text{TT} = \text{TAI} + 32.184\text{s} \tag{A.14c}$$

where ΔUT1 & ΔAT are offset values that are updated and published daily (see [41] for aggregated data). Lastly, the Julian Date (JD) represents the current date and time measured in days relative to January 1, 4713 B.C.E. 12:00:00.000. This may be converted to centuries relative to a more recent epoch to reduce the number of significant digits needed e.g. $\text{T} = (\text{JD} - 2,451,545.0)/36,525$ centuries past J2000.0 [33].

A.8 Central Body Gravity Model Gradient

The central body gravity potential U and acceleration $\mathbf{a}_{\text{aspherical}}$ are defined in Section 3.1.1. The acceleration gradient (Hessian of the potential) is then:

$$\frac{\partial \mathbf{a}_{\text{aspherical}}}{\partial \mathbf{r}} = -\frac{\partial^2 U}{\partial \mathbf{r}^2} \tag{A.15a}$$

$$= -\left(\frac{\partial^2 U_0(\mathbf{r})}{\partial \mathbf{r}^2} + \frac{\partial}{\partial \mathbf{r}}\frac{\partial U_{1+2}(\mathbf{x}_s)}{\partial \mathbf{r}}\right) \tag{A.15b}$$

$$= -\left(\frac{\partial^2 U_0(\mathbf{r})}{\partial \mathbf{r}^2} + \frac{\partial}{\partial \mathbf{r}}\left(\frac{\partial U_{1+2}}{\partial \mathbf{x}_s}\frac{\partial \mathbf{x}_s}{\partial \mathbf{r}}\right)\right) \tag{A.15c}$$

$$= -\left(\frac{\partial^2 U_0(\mathbf{r})}{\partial \mathbf{r}^2} + \left(\frac{\partial \mathbf{x}_s}{\partial \mathbf{r}}\frac{\partial}{\partial \mathbf{r}}\left(\frac{\partial U_{1+2}}{\partial \mathbf{x}_s}\right) + \frac{\partial U_{1+2}}{\partial \mathbf{x}_s}\frac{\partial^2 \mathbf{x}_s}{\partial \mathbf{r}^2}\right)\right) \tag{A.15d}$$

$$= -\left(\frac{\partial^2 U_0(\mathbf{r})}{\partial \mathbf{r}^2} + \frac{\partial \mathbf{x}_s}{\partial \mathbf{r}}\frac{\partial^2 U_{1+2}}{\partial \mathbf{x}_s^2}\frac{\partial \mathbf{x}_s}{\partial \mathbf{r}} + \frac{\partial U_{1+2}}{\partial \mathbf{x}_s}\frac{\partial^2 \mathbf{x}_s}{\partial \mathbf{r}^2}\right) \tag{A.15e}$$

where (A.15f)

$$\frac{\partial U_{1+2}}{\partial \mathbf{x}_s}\frac{\partial^2 \mathbf{x}_s}{\partial \mathbf{r}^2} = \frac{\partial U_{1+2}}{\partial r}\frac{\partial^2 r}{\partial \mathbf{r}^2} + \frac{\partial U_{1+2}}{\partial \lambda}\frac{\partial^2 \lambda}{\partial \mathbf{r}^2} + \frac{\partial U_{1+2}}{\partial \phi}\frac{\partial^2 \phi}{\partial \mathbf{r}^2} \tag{A.15g}$$

where $\mathbf{x}_s = (r, \lambda, \phi)$ are the spherical coordinates in which $U_{1+2} = U_1 + U_2$ is defined. The two-body Hessian term is:

$$-\frac{\partial^2 U_0(\mathbf{r})}{\partial \mathbf{r}^2} = -\frac{\mu}{\|\mathbf{r}\|^3} I_{3\times 3} + \frac{3}{\|\mathbf{r}\|^5} \mathbf{r}\mathbf{r}^T \tag{A.16}$$

Expressions for the higher order Jacobian and Hessians in terms 2 & 3 of Equation A.15e are documented in Vallado [33].

Bibliography

[1] Radar Systems, Electronic Systems Society, and Radar Systems Electronic Systems Society. "IEEE Standard Letter Designations for Radar-Frequency Bands". In: *IEEE Std 521-2002 (Revision of IEEE Std 521-1984)* 1984 (2003), pp. 5–14. DOI: 10.1109/IEEESTD.2003.94224.

[2] Hamid Hemmati, ed. *Near-Earth Laser Communications.* Boca Raton: CRC Press, 2009. ISBN: 9780824753818.

[3] William L. Casey and Stephen G. Lambert. *Laser Communications in Space.* Norwood: Artech House Inc, 1995. ISBN: 0890067228.

[4] Morris Katzman, ed. *Laser Satellite Communications.* Prentice-Hall, Inc., 1987. ISBN: 0135238048.

[5] Hank Heidt et al. "CubeSat: A new Generation of Picosatellite for Education and Industry Low-Cost Space Experimentation". In: *14th Annual/USU Conference on Small Satellites.* 2000. ISBN: 6507238651.

[6] Siegfried Janson et al. "The NASA Optical Communications and Sensor Demonstration Program : Initial Flight Results". In: *29th Annual AIAA/USU Conference on Small Satellities* (2015), SSC16–III–03.

[7] Kerri Cahoy et al. "The CubeSat Laser Infrared CrosslinK Mission (CLICK)". In: *International Conference on Space Optics.* Vol. 11180. 2018. DOI: 10.1117/12.2535953.

[8] C Schmidt, M Brechtelsbauer, and F Rein. "OSIRIS Payload for DLR's BiROS Satellite". In: *Conference on Space Optical Systems* (2014). URL: http://elib.dlr.de/89346/.

[9] E. Perez, M. Bailly, and J. M. Pairot. "Pointing Acquisition And Tracking System For Silex Inter Satellite Optical Link". In: *SPIE 1989 Technical Symposium on Aerospace Sensing.* Vol. 1111. 1989. DOI: 10.1117/12.977988.

[10] Zoran Sodnik, Bernhard Furch, and Hanspeter Lutz. "Optical Intersatellite Communication". In: *IEEE Journal of Selected Topics in Quantum Electronics* 16.5 (2010). ISSN: 03540596. DOI: 10.1109/MILCOM.2010.5680175.

[11] F. Heine et al. "Optical Intersatellite Communication". In: *Proceedings - IEEE Military Communications Conference MILCOM* 16.5 (2010), pp. 1583–1587. ISSN: 03540596. DOI: 10.1109/MILCOM.2010.5680175.

[12] Bryan S. Robinson et al. "The lunar laser communications demonstration". In: *2011 International Conference on Space Optical Systems and Applications, ICSOS'11* Llcd (2011), pp. 54–57. ISSN: 0277786X. DOI: 10.1109/ICSOS.2011.5783709.

[13] Alberto Carrasco-Casado et al. "LEO-to-ground optical communications using SOTA (Small Optical TrAnsponder): Payload verification results and experiments on space quantum communications". In: *Acta Astronautica* 139 (2017), pp. 377–384. ISSN: 00945765. DOI: 10.1016/j.actaastro.2017.07.030. URL: http://dx.doi.org/10.1016/j.actaastro.2017.07.030.

[14] *Web Page. RISESat (Rapid International Scientific Experiment Satellite) / Hodoyoshi-2.* Accessed 2019. URL: https://directory.eoportal.org/web/eoportal/satellite-missions/r/risesat.

[15] David J. Israel, Bernard L. Edwards, and John W. Staren. "Laser communications relay demonstration (LCRD) update and the path towards optical relay operations". In: *IEEE Aerospace Conference Proceedings* (2017), pp. 1–6. ISSN: 1095323X. DOI: 10.1109/AERO.2017.7943819.

[16] *Web Page. Focus tunable lenses.* Accessed 2019. URL: https://www.optotune.com/technology/focus-tunable-lenses.

[17] Antonios Seas, Zachary Gonnsen, and Timothy Yarnall. *ILLUMA-T : Integrated LCRD LEO User Modem and Amplifier Terminal Payload.* Tech. rep. NASA, 2018. URL: https://ntrs.nasa.gov/search.jsp?R=20180002846.

[18] Bryan S. Robinson et al. "TeraByte InfraRed Delivery (TBIRD): a demonstration of large-volume direct-to-Earth data transfer from low-Earth orbit". In: *SPIE LASE.* San Francisco, 2018. DOI: 10.1117/12.2295023.

[19] Jessica Chang et al. "Body pointing, acquisition and tracking for small satellite laser communication". In: *Free-Space Laser Communications XXXI* March (2019). DOI: 10.1117/12.2511159.

[20] Peter Grenfell et al. *Pointing, Acquisition, and Tracking for Small Satellite Laser Communications.* Tech. rep. URL: https://digitalcommons.usu.edu/cgi/viewcontent.cgi?article=4230%7B%5C&%7Dcontext=smallsat.

[21] Cadence Payne et al. "Integration and Testing of the Nanosatellite Optical Downlink Experiment". In: *Annual AIAA/USU Conference on Small Satellites, SSC18-XII-05.* URL: https://digitalcommons.usu.edu/cgi/viewcontent.cgi?article=4141%7B%5C&%7Dcontext=smallsat.

[22] Kathleen Michelle Riesing. "Portable Optical Ground Stations for Satellite Communication". PhD thesis. Massachusetts Institute of Technology, 2018.

[23] Kathleen Riesing, Hyosang Yoon, and Kerri Cahoy. "A portable optical ground station for low-earth orbit satellite communications". In: *2017 IEEE International Conference on Space Optical Systems and Applications, ICSOS 2017* Llcd (2018), pp. 108–114. DOI: 10.1109/ICSOS.2017.8357219.

[24] Laura Yenchesky et al. "Optomechanical Design and Analysis for Nanosatellite Laser Communications". In: *Proceedings of the AIAA/USU Conference on Small Satellites.* 2019.

[25] B.E.A. Saleh and M.C. Teich. *Fundamentals of Photonics.* Hoboken, N.J.: Wiley-Interscience, 1991. ISBN: 0-471-2-1374-8. URL: http://opt.zju.edu.cn/zjuopt2/upload/resources/chapter3%7B%5C%%7D2520Beam%7B%5C%%7D2520Optics.pdf.

[26] John J. Degnan and Bernard J. Klein. "Optical Antenna Gain 1: Transmitting Antennas". In: *Applied Optics* 13.12 (1974), p. 2762. ISSN: 0003-6935. DOI: 10.1364/ao.13.002762.

[27] Tam Nyugen. "Laser Beacon Tracking for Free-space Optical Communication on Small-Satellite Platforms in Low-Earth Orbit". Masters Thesis. Massachusetts Institute of Technology, 2015.

[28] Emily B Clements. "Probabilistic Methods for Systems Engineering with Application to Nanosatellite Laser Communications". PhD thesis. Massachusetts Institute of Technology, 2018.

[29] Wolfram Research. *Web Page. Wolfram MathWorld.* URL: http://mathworld.wolfram.com/.

[30] Michael J Long. "Pointing Acquisition and Tracking Design and Analysis for CubeSat Laser Communication Crosslinks". Masters Thesis. Massachusetts Institute of Technology, 2018.

[31] James Paul Mason et al. "MinXSS-1 CubeSat On-Orbit Pointing and Power Performance: The First Flight of the Blue Canyon Technologies XACT 3-axis Attitude Determination and Control System". In: (2017). arXiv: 1706.06967. URL: http://arxiv.org/abs/1706.06967.

[32] Hank D. Voss et al. "Globalstar Communication Link for CubeSats: TSAT, GEARRS1, and GEARRS2". In: *29th Annual AIAA/USU Conference on Small Satellites.* 2015.

[33] David A. Vallado. *Fundamentals of Astrodynamics and Applications.* 1st. Hawthorne: Microcosm Press, 2013.

[34] Kathleen Riesing. "Orbit Determination from Two Line Element Sets of ISS-Deployed CubeSats". In: *29th Annual AIAA/USU Conference on Small Satellites, 8-13 August* (2015), pp. VIII–5.

[35] D. P. Rubincam. "General relativity and satellite orbits - The motion of a test particle in the Schwarzschild metric". In: *Celestial Mechanics* 15 (1977), pp. 21–33.

[36] *Web Page. Index of /pub/warehouse/2019/WeeklyPDF/.* 2019. URL: `ftp://ftp.swpc.noaa.gov/pub/warehouse/2019/WeeklyPDF/`.

[37] Erin Kahr et al. "GPS tracking on a nanosatellite the CanX-2 flight experience". In: *8th International ESA Conference on Guidance, Navigation & Control Systems.* 2011.

[38] Hannu Leppinen. "Integration of a GPS subsystem into the Aalto-1 nanosatellite". PhD thesis. Aalto University, 2018.

[39] Srig-are Thrana and Jan Schulte. "Innovative NewSpace Ground Segment fffdfffdfffd Global Coverage Available Through the Cloud". In: *Annual AIAA/USU Conference on Small Satellites.* 2016.

[40] Ben K Bradley. "Numerical Algorithms for Precise and Efficient Orbit Propagation and Positioning". PhD thesis. University of Colorado, 2009.

[41] T.S. Kelso. *Web Page. EOP and Space Weather Data.* 2019. URL: `http://celestrak.com/SpaceData/`.

[42] *Web Page. Maia.* 2011. URL: `ftp://tai.bipm.org/iers/conv2010/chapter5/`.

[43] David Vallado. *Web Page. Astrodynamics Software.* 2019. URL: `http://www.celestrak.com/software/vallado-sw.php`.

[44] Mohinder S. Grewal, Lawrence R. Weill, and Angus P. Andrews. *Global Positioning Systems, Inertial Navigation, and Integration.* John Wiley & Sons,Inc., 2001. ISBN: 0471200719.

[45] United States Coast Guard Navigation Center. *Web Page. GPS CONSTELLATION STATUS.* URL: `https://www.navcen.uscg.gov/?Do=constellationStatus`.

[46] *Global Positioning System Standard Positioning Service Performance Standard.* Tech. rep. September. Department Of Defense, United States of America, 2008, pp. 1–160. URL: http://www.gps.gov/technical/ps/2008-SPS-performance-standard.pdf.

[47] Yaakov Bar-Shalom, X. Rong-Li, and Thiagalingam Kirubarajan. *Estimation with Applications to Tracking and Navigation.* John Wiley & Sons,Inc., 2001. ISBN: 047141655X.

[48] Peter W Sarunic. *Development of GPS Receiver Kalman Filter Algorithms for Stationary, Low-Dynamics, and High-Dynamics Applications.* Tech. rep. Cyber, Electronic Warfare Division Defence Science, and Technology Group, Australian Government Department of Defence, 2016.

[49] Novatel. *Web Page. OEM7 Commands and Logs Reference Manual.* URL: https://docs.novatel.com/OEM7/Content/PDFs/OEM7_Commands_Logs_Manual.pdf.

[50] Elliot D. Kaplan and Christopher J. Hegarty. *Understanding GPS: Principles and Applications.* 2nd. Artech House Inc, 2006.

[51] Bradford W. Parkinson et al. *Global Positioning System: Theory and Applications, Volume 1.* Washington DC: American Institute of Aeronautics and Astronautics, 1996. ISBN: 156347106X.

[52] Novatel. *Web Page. Receivers OEM4-G2.* URL: https://www.novatel.com/assets/Documents/Papers/oem4g2.pdf.

[53] Novatel. *Web Page. Receivers OEM615.* URL: https://www.novatel.com/assets/Documents/Papers/OEM615.pdf.

[54] Novatel. *Web Page. Receivers OEM719.* URL: https://www.novatel.com/assets/Documents/Papers/OEM719-Product-Sheet.pdf.

[55] Novatel. *Web Page. Receivers OEM729.* URL: https://www.novatel.com/assets/Documents/Papers/OEM729-Product-Sheet.pdf.

[56] Novatel. *Web Page. Receivers OEM7600.* URL: https://www.novatel.com/assets/Documents/Papers/OEM7600-Product-Sheet.pdf.

[57] Novatel. *Web Page. GPS Position Accuracy Measures.* URL: https://www.novatel.com/assets/Documents/Bulletins/apn029.pdf.

[58] Globalsat. *Web Page. GPS Mouse Users Guide V1.0 (WIN).* URL: https://www.globalsat.com.tw/ftp/download/GMouse_Win_UsersGuide-V1.0.pdf.

[59] Rudolph Kalman. "A New Approach to Linear Filtering and Prediction Problems". In: *Transactions of the ASME-Journal of Basic Engineering* 82 (1960), pp. 35–45. ISSN: 00223611. DOI: 10.1007/BF00248635. arXiv: NIHMS150003.

[60] John L. Crassidis and John L. Junkins. *Optimal Estimation of Dynamic Systems.* 2nd. CRC Press, 2004. ISBN: 158488391X.

[61] Arthur Gelb et al. *Applied optimal estimation.* 16th ed. Cambridge, Massachusetts: The MIT Press, 2001. ISBN: 0262200279. URL: http://ieeexplore.ieee.org/document/1454444/.

[62] M. Verhaegen and P. Van Dooren. "Numerical aspects of different Kalman filter implementations". In: *IEEE Transactions on Automatic Control* 31.10 (2004), pp. 907–917. ISSN: 0018-9286. DOI: 10.1109/tac.1986.1104128.

[63] Andreas Martin Kettner and Mario Paolone. "Sequential Discrete Kalman Filter for Real-Time State Estimation in Power Distribution Systems: Theory and Implementation". In: *IEEE Transactions on Instrumentation and Measurement* 66.9 (2017), pp. 2358–2370. ISSN: 00189456. DOI: 10.1109/TIM.2017.2708278. arXiv: arXiv:1702.08262v5.

[64] Catherine L. Thornton. "Triangular Covariance Factorizations for Kalman Filtering". PhD thesis. California Institute of Technology, 1976. ISBN: 1977000517.

[65] Bierman Gerald J. "Measurement updating using the U-D factorization". In: *Automatica* 12.4 (1976), pp. 375–382.

[66] Catherine L. Thornton and Gerald J. Bierman. *A Numerical Comparison of Discrete Kalman Filtering Algorithms: An Orbit Determination Case Study.* Tech. rep. 1976.

[67] Richard L. Burden and J. Douglas Faires. *Numerical Analysis.* 9th. Boston: Brooks/Cole CENGAGE Learning, 2011. ISBN: 0538733519.

[68] Lawrence F. Shampine and Mark W. Reichelt. "The MATLAB ODE Suite". In: *SIAM Journal on Scientific Computing* 18.1 (2003), pp. 1–22. ISSN: 1064-8275. DOI: 10.1137/s1064827594276424.

[69] J. R. Dormand and P. J. Prince. "A family of embedded Runge-Kutta formulae". In: *Journal of Computational and Applied Mathematics* 6.1 (1980), pp. 19–26. ISSN: 0771050X. DOI: 10.1016/0771-050X(80)90013-3.

[70] Cleve Moler and Charles Van Loan. "Nineteen Dubious Ways to Compute the Exponential of a Matrix, Twenty-Five Years Later". In: *SIAM Review* 45.1 (2005), pp. 3–49. ISSN: 0036-1445. DOI: 10.1137/s00361445024180.

[71] Nicholas J. Higham. "The Scaling and Squaring Method for the Matrix Exponential Revisited Nicholas J . Higham Manchester Institute for Mathematical Sciences School of Mathematics The University of Manchester". In: *SIAM Review* 51.4 (2009), pp. 747–764.

[72] Nicholas J. Higham and Awad H. Al-Mohy. "A New Scaling and Squaring Algorithm for the Matrix Exponential". In: *SIAM J. Matrix Analy. Appl.* 31.3 (2009), pp. 970–989.

[73] William F. Arnold and Alan J. Laub. "Generalized eigenproblem algorythms and software for algebraic Riccati equations". In: *Proceedings of the IEEE* 72.12 (1984), pp. 1746–1754.

[74] H Fassbender. "The Parameterized SR Algorithm for Hamiltonian Matrices". In: *Mathematics of Computation* 70.236 (2000), pp. 1515–1541.

[75] S Serbin and C Serbin. "A Time Stepping Procedure for X = AX + XA + D, X(0) = C". In: *IEEE Transactions on Automatic Control* AC-25.6 (1980), pp. 1138–1141.

[76] Catherine L. Thornton and Gerald J. Bierman. "Gram-Schmidt algorithms for covariance propagation". In: *International Journal of Control* 25.2 (1977), pp. 243–260. ISSN: 13665820. DOI: 10.1080/00207177708922225.

[77] Karl J. Astrom and Bjorn Wittenmark. *Computer-Controlled Systems.* 2nd. Mineola: Dover Publications Inc., 2011. ISBN: 0486486133.

[78] Ben Noble. *Applied Linear Algebra.* Prentice-Hall, Inc., 1969.

[79] John L Crassidis. "Survey of Nonlinear Attitude Estimation Methods". In: 30.1 (2007), pp. 12–28. DOI: 10.2514/1.22452.

[80] Subhash Challa, Robin J Evans, and Xuezhi Wang. "A Bayesian solution and its approximations to out-of-sequence measurement problems q". In: 4 (2003), pp. 185–199. DOI: 10.1016/S1566-2535(03)00037-X.

[81] Mark L Psiaki. "Autonomous Orbit Determination for Two Spacecraft from Relative Position Measurements". In: *Journal of Guidance Control and Dynamics* 22.2 (1999).

[82] P. Dave and K. Cahoy. "Laser Communication Crosslinks for Satellite Autonomous Navigation". In: *Proceedings of the AIAA/USU Conference on Small Satellites, Poster Session II, SSC18-PII-33.* 2018. URL: https://digitalcommons.usu.edu/smallsat/2018/all2018/394/.

[83] *Web Page. LCRD (Laser Communications Relay Demonstration) Mission.* Accessed 2019. URL: https://eoportal.org/web/eoportal/satellite-missions/content/-/article/lcrd.

[84] Daniel M. Dobkin. "Chapter 5 - Antennas". In: *RF Engineering for Wireless Networks.* 2005. Chap. 5, pp. 193–249. ISBN: 9780750678735. URL: http://www.sciencedirect.com/science/article/pii/B9780750678735500054.

[85] Christopher M Pong. "On-Orbit Performance & Operation of the Attitude & Pointing Control Subsystems on ASTERIA". In: *AIAA/USU Conference on Small Satellites, SSC18-PI-34*. 2018. URL: https://digitalcommons.usu.edu/cgi/viewcontent.cgi?article=4173%7B%5C&%7Dcontext=smallsat%7B%5C%%7D0Ahttps://digitalcommons.usu.edu/smallsat/2018/all2018/361.